

**AN ANALYSIS OF ATOMIC WAVE FUNCTIONS TO IMPROVE
DENSITY FUNCTIONAL KINETIC ENERGY MODELS**

A THESIS

**SUBMITTED TO THE GRADUATE SCHOOL
IN PARTIAL FULFILLMENT OF THE REQUIREMENTS**

FOR THE DEGREE

MASTERS OF SCIENCE, PHYSICS

BY

JEREMY REDD

DR. ANTONIO CANCIO - ADVISOR

BALL STATE UNIVERSITY

MUNCIE, INDIANA

DECEMBER 2015

Contents

Abstract	v
Acknowledgements	vi
List of Figures	vii
List of Tables	x
1 Introduction	1
1.1 Understanding Density Functional Theory	1
1.1.1 Why Density Functional Theory?	1
1.1.2 What is Density Functional Theory?	2
1.1.3 What Does Density Functional Theory Do?	3
1.1.4 31 Flavors of DFT	3
1.2 Applications of DFT	6
1.2.1 Traditional Applications–Orbital DFT	6
1.2.2 Large Scale DFT–OFDFT	7
1.3 Current Challenges in OFDFT	8
1.3.1 Research	9
1.3.2 Outline	11
2 Theory	12

2.1	The Many Body Hamiltonian	12
2.1.1	Hohenberg and Kohn	14
2.2	TF Theory	16
2.2.1	The Homogeneous Electron Gas	16
2.2.2	The Slowly Varying Electron Gas	18
2.2.3	The TF Energy	21
2.3	Kohn and Sham Method	23
2.3.1	Orbitals	23
2.3.2	The von Weizsacker Approximation	25
2.4	Kohn and Sham Method, Orbital Free	27
2.4.1	Models of the KS Kinetic Energy	27
2.4.2	The Gradient Expansion	27
2.4.3	Constraints on the KS Kinetic Energy	29
2.5	Perdew and Constantin	31
2.5.1	The Enhanced Gradient Expansion	31
2.5.2	The mGGA Stitching Function	32
2.5.3	Critique of the mGGA Stitching Function	32
2.6	The KS Model for Atoms	36
3	Methods	39
3.1	Atomic DFT	39
3.1.1	Spherical Wave Orbitals	40
3.1.2	Logarithmic Grids	40
3.2	What Algorithms Were Used?	42
3.2.1	Input	42
3.2.2	Density	43
3.2.3	The Kohn-Sham Model	43
3.2.4	Energy Densities	44

3.2.5	Total Energy	44
3.3	Code Tests and Verification	44
3.3.1	Comparing Densities to FHI98PP	44
3.3.2	Normalization and Electron Counting	46
3.3.3	Hydrogen Orbital Test Case	46
3.3.4	Green's Theorem	47
3.3.5	Comparing Total Energies to FHI98PP	49
4	Analysis and Results	50
4.1	Visualizing Parametrizations	51
4.1.1	The Second Row of the Periodic Table	53
4.1.2	Noble Gases	55
4.1.3	Three Regimes	56
4.1.4	Views in 3D space	56
4.2	Gradient Expansion Fits	58
4.3	Stitching Between the GEA2 and VW	67
4.3.1	Perdew and Constantin	68
4.3.2	The mGGAreV Model: Canonical GEA2	68
4.3.3	The mGGAreV Model: Empirically Fit GEA2	71
4.4	Analysis of the near-nuclear Regime	73
4.4.1	The Link Between p shells and the Constant	73
4.4.2	A Toy Model	75
4.5	Kinetic Energies and Kinetic Energy Densities	77
4.5.1	Local Energy Densities	77
4.5.2	Total Energies	83
5	Conclusions and Future Work	91
5.1	Triumphs	91

5.1.1	Two Turning Points Vs. One	91
5.1.2	Empirically Fit Gradient Expansions	92
5.1.3	Goldilocks Stitching Behavior	92
5.1.4	Atoms with $Z > 2$ Don't Approach the von Weizsacker Limit	93
5.2	Failings	93
5.2.1	Underestimation of the Total Energy for Large Z Atoms	93
5.2.2	Overestimation of the Total Energy for Small Z Atoms	94
5.3	Future Work	94
A List of Acronyms		96
B Lagrangian Interpolation Polynomials and Derivatives		97
C Hartree Fock		99
D Thomas Fermi Scaling		100
E The Thomas-Fermi Potential		102
E.0.1	The Binding Problem	103
Bibliography		106

ABSTRACT

THESIS: An Analysis of Atomic Wave Functions to Improve Density Functional Kinetic Energy Models

STUDENT: Jeremy Joseph Redd

DEGREE: Master of Science, Physics

COLLEGE: Sciences and Humanities

DATE: December 2015

PAGES: 108

Density Functional Theory (DFT) is a semi-classical computational theory developed to accurately predict electron charge density, ground-state energy, band gap energies, and other electronic properties. It has applications in chemistry, semiconductor physics, material science, and other fields. A major bottleneck is the increase of resources required to calculate atomic orbitals individually when scaling to systems of many electrons. An orbital free model that accurately predicts atomic kinetic energy densities is necessary for the largest scale problems. One approach to orbital free functionals is the work of Perdew and Constantin, who developed a model that stitches together the second order gradient expansion, a model that predicts kinetic energy density for a very large number of electrons well, with the von Weizsacker model, an analytical model that accurately predicts kinetic energy densities for bosons, and does well for small atoms. Our group finds the PC model to break down when predicting bonding energies, and has proposed a new class of stitching function. We are analyzing this stitching function for single atoms, studying scaling properties across the periodic table and beyond to test the validity of our model against known properties and scaling laws of atoms. We are using well known atomic electron number densities generated by a program, FHI98PP, and running them through several models including our own. We then compare kinetic energy densities, total kinetic energy densities vs nuclear charge.

Acknowledgments and Quotes

This thesis is dedicated to my wife for inspiring me to achieve my dreams.

"The worthwhile problems are the ones you can really solve or help solve, the ones you can really contribute something to. No problem is too small or too trivial if we can really do something about it."

Richard Feynman

"Oh the flavors of DFT, there's a DFT for you and me! My, DFT is lots of fun. There's a DFT for everyone."

Me, after a fair amount of sleep deprivation.

First, I would like to thank Dr. Antonio Cancio, Dr. Chris Nelson, Jesse Wattson, and the BSU physics department at large. I mostly had fun, and didn't tear all of my hair out (although I lost more than I'd like). Second, I would like to thank Thomas Baker at U.C. Irvine for generously sharing the Gnuplot style files that were used to generate the graphs throughout this thesis. Finally, I would like to thank my wife Megan. She has the intestinal fortitude to put up with me.

Thank you all!

List of Figures

2.1	(a) This is a plot of $\tau_{ks}(\mathbf{r})$ for C_3H_4 using an LDA pseudo-potential. This is a cross section of the C-C-C bond axis and two hydrogens. In-plane atoms and bonds are shown as black disks and line segments; out of plane ones as dashed lines and open disks. This Figure is taken from the Cancio group [1].	
	(b) This is a plot of $\tau_{mGGA}(\mathbf{r})$ for C_3H_4 . This is the same cross section as in Figure 2.1(a). The contour color scale is also the same.	34
2.2	This plots $\nabla^2 n(\mathbf{r})$ for C_3H_4 as generated by the KS model with a LDA. This is the same cross section as in Figure 2.1(a).	35
2.3	This plots $F_{mGGA}(0, q)$, $F_{mGGA_{rev}}(0, q)$ and $F_{GEA2}(0, q)$ vs $q(\mathbf{r})$	35
3.1	(a) This plot is of the absolute difference between FHI98PP's density and the calculated density for He. (b) This plot is of the absolute difference between FHI98PP's density and the calculated density for Ne.	45
4.1	(a) Number density $n(\mathbf{r})$ given by Equation 2.43 for argon. (b) $p(r)$ given by Equation 2.58 and $q(r)$ given by Equation 2.59	54
4.2	Parametric plot of $p(\mathbf{r})$ vs $q(\mathbf{r})$ for row two of the periodic table.	55
4.3	(a) Parametric plot of $p(\mathbf{r})$ vs $q(\mathbf{r})$ for helium, neon, argon, and radon. (b) Parametric plot of $p(\mathbf{r})$ vs $q(\mathbf{r})$ for krypton and xenon.	57
4.4	Parametric plot of $p(\mathbf{r})$ vs $q(\mathbf{r})$ for all atoms in column eight of the periodic table.	58

4.5	(a) $F_{ks}^p(p, q)$ vs $p(\mathbf{r})$ vs $q(\mathbf{r})$ for noble gases rotated 30 degrees about the F axis. (b) $F_{ks}^p(p, q)$ vs $p(\mathbf{r})$ vs $q(\mathbf{r})$ for noble gases rotated 60 degrees about the F axis.	59
4.6	(a) $F_{ks}^p(p, q)$ vs $p(\mathbf{r})$ vs $q(\mathbf{r})$ for noble gases rotated 90 degrees about the F axis. (b) $F_{ks}^p(p, q)$ vs $p(\mathbf{r})$ vs $q(\mathbf{r})$ for noble gases rotated 120 degrees about the F axis.	60
4.7	(a) $F_{ks}^p(p, q)$ and $F_{GEA2}^p(p, q)$ vs $p(\mathbf{r})$ vs $q(\mathbf{r})$ rotated such that the plane described by $F_{GEA2}^p(p, q)$ viewed in the $q = 0$ direction is seen edge on. (b) $F_{ks}^p(p, q)$ and $F_{GEA2}^p(p, q)$ vs $p(\mathbf{r})$ vs $q(\mathbf{r})$ rotated such that the plane described by $F_{GEA2}^p(p, q)$ viewed in the $p = 0$ direction is seen edge on.	62
4.8	(a) Fit parameter $a(Z)$ vs Z as determined by fitting Equation 4.2 to $F_{ks}^p(p, q)$ of individual atoms. (v) Fit parameter $\theta(Z)$ vs Z as determined by fitting Equation 4.2 to $F_{ks}^p(p, q)$ of individual atoms.	64
4.9	(a) $F_{ks}^p(p, q)$ and an $F_{GEA2}^p(p, q)$ empirically fit to large Z atoms vs $p(\mathbf{r})$ vs $q(\mathbf{r})$, rotated such that the plane described by the empirically fit $F_{GEA2}^p(p, q)$ viewed from the $q = 0$ direction is seen edge on. (b) $F_{ks}^p(p, q)$ and an $F_{GEA2}^p(p, q)$ empirically fit to large Z atoms vs $p(\mathbf{r})$ vs $q(\mathbf{r})$, rotated such that the plane described by the empirically fit $F_{GEA2}^p(p, q)$ viewed in the $p = 0$ direction is seen edge on.	66
4.10	Square of the standard deviation away from $F_{ks}^p(p, q)$ of the canonical $F_{GEA2}^p(p, q)$ and the $F_{GEA2}^p(p, q)$ empirically fit to large Z atoms in the core region of $F_{ks}^p(p, q)$	67
4.11	(a) $F_{mGGA_{rev}}^p(z)$, $F_{mGGA}^p(p, q)$, $F_{ks}^p(\mathbf{r})$, and $F_{GEA2}^p(z)$ vs z . (b) Re-plot of Figure 4.11(a) zoomed in on the near-nuclear region.	70
4.12	(a) $F_{mGGA_{rev}}^p(z_{emp})$, $F_{mGGA}^p(p, q)$, $F_{ks}^p(p, q)$, and $F_{GEA2}^p(z_{emp})$ vs z_{emp} . (b) Re-plot of Figure 4.12(a) zoomed in on the near-nuclear region.	72

4.13	$F_{mGGA}(0, q)$, $F_{mGGA_{rev}}(0, q)$ stitched to the canonical GEA2 where $\alpha = 4$, $F_{mGGA_{rev}}(0, q)$ stitched to the canonical GEA2 where $\alpha = 1$, and $F_{mGGA_{rev}}(0, q)$ stitched to $F_{GEA2}^p(z_{emp})$ empirically fit to large Z atoms where $\alpha = 4$ vs $q(\mathbf{r})$.	74
4.14	(a) $4\pi\mathbf{r}^2\tau_{model}(\mathbf{r})$ of helium for several models. (b) $4\pi\mathbf{r}^2[\tau_{model}(\mathbf{r}) - \tau_{ks}(\mathbf{r})]$ of helium for several models.	79
4.15	(a) $4\pi\mathbf{r}^2\tau_{model}(\mathbf{r})$ of neon for several models. (b) $4\pi\mathbf{r}^2[\tau_{model}(\mathbf{r}) - \tau_{ks}(\mathbf{r})]$ of neon for several models.	81
4.16	(a) $4\pi\mathbf{r}^2\tau_{model}(\mathbf{r})$ of potassium for several models. (b) $4\pi\mathbf{r}^2[\tau_{model}(\mathbf{r}) - \tau_{ks}(\mathbf{r})]$ of potassium for several models.	82
4.17	(a) This plot shows $4\pi\mathbf{r}^2\tau_{model}(\mathbf{r})$ of ununoctium for several models similar to Figure 4.14(a). (b) This plot shows $4\pi\mathbf{r}^2[\tau_{model}(\mathbf{r}) - \tau_{ks}(\mathbf{r})]$ of ununoctium for several models.	84
4.18	(a) This plots $T/Z^{7/3}$ vs $Z^{-1/3}$ for various kinetic energy models. (b) $T/Z^{7/3}$ vs $Z^{-1/3}$ for fewer, more important, kinetic energy models for visual clarity. .	89
4.19	This plots $T/Z^{7/3}$ vs $Z^{-1/3}$ for various kinetic energy models.	90

List of Tables

3.1	Table actual Z vs calculated Z and their relative error for various atoms. . . .	46
3.2	Table of theoretical Hydrogen orbital total energies, calculated energies and relative error	47
3.3	Table of $\int_0^\infty \nabla^2 n(r)$, FHI98PP total energies, and their respective ratio. . . .	48
3.4	Table of the difference between green's function terms Equation 3.16, the total kinetic energy, and their respective ratios for several atoms.	48
3.5	Table of Fhi98pp Total energies and our calculated total energies using the Kohn-Sham model with relative error. The dashes indicate that the first uncertain digit was less than the last significant digit in the FHI98PP output.	49
4.1	Table of fit parameters for various models in $T/Z^{7/3}$ vs $Z^{-1/3}$ space.	90

Chapter 1

Introduction

1.1 Understanding Density Functional Theory

1.1.1 Why Density Functional Theory?

A common joke in the computational physics community is as follows. An experimentalist presents his research and everyone believes him, except himself. A theorist presents his research and no one believes him, except himself. A computationalist presents his research and no one believes him, including himself. This is, to some extent, true.

In a world where one had all the computational power one wanted, one would simply solve the exact governing equation for every problem one encountered, no matter how complex. In a world where computation is finite, solving the exact governing equation for a system is not always computationally cost effective. This means that the computation time using the exact governing equation is very long.

To reduce the computational resources required to solve a specific problem, physicists make simplifying assumptions. These assumptions also decrease the accuracy of the mathematical description of the system. The goal of the computational physicist is to limit the error of the assumptions made while trying to maintain a cost effective model.

To give an example, the governing equation for quantum mechanics is the Schrödinger

Equation. Unfortunately there are few analytical solutions for the Schrödinger Equation. The most notable analytical solution is the electronic structure of the hydrogen atom. This system is solvable because it is a single particle problem. Most real world systems are many-particle. These would include any atom other than hydrogen, molecules, and solids.

The Schrödinger Equation requires many-particle wave functions to describe many-particle systems. Consequently, the Schrödinger Equation is not a very computationally cost-effective equation. In practice, the Schrödinger Equation is not really used directly to solve many-particle problems in most applications. This means that understanding the electronic structure of matter at the quantum level requires simplifying assumptions. Density Functional Theory is a model that makes these kinds of assumptions.

1.1.2 What is Density Functional Theory?

Density Functional Theory (DFT) is a computational method that replaces many-particle electron wave functions with expected electron densities. These expected densities behave similarly to a single-particle wave function. It has been shown by Hohenberg and Kohn [2] that not only is this a reasonable assumption, but there is in fact a perfect one-to-one mapping between many-particle wave functions and expected electron densities for ground-state systems. They prove that a unique external potential maps to a unique ground-state density. Because the uniqueness of the wave function is determined by the external potential, one can replace wave functions with densities.

DFT methods are the most widely used methods for solving quantum mechanical systems in the fields of chemistry and material science [3][4][5]. In principle any DFT method minimizes total energy density functionals with respect to density to find the ground-state energy. These functionals could be, in theory, exactly mapped from Hamiltonians acting on wave functions. Though it is proven to exist, the mapping between Hamiltonians acting on wave functions and total energy density functionals is unknown. The most accurate mapping that has been found is the Kohn-Sham method [6]. DFT methods are desirable computa-

tional methods for solving many body systems like molecules or materials as will be shown throughout this thesis.

1.1.3 What Does Density Functional Theory Do?

The benefit of replacing wave functions with densities is the reduction in computational load for a given problem. This is because a many-particle wave function of N particles is a function of N position variables, each of which must be solved for. Conversely, a continuous density depends on only one position variable. This means that minimizing a density functional requires fewer computations than any method that requires many-particle wave functions.

DFT models are constructed from kinetic energy and potential energy density functionals. The electron-electron interactions must somehow be modeled in either the kinetic energy functional, the potential functional or both. It turns out that modeling these electron-electron interactions is not trivial.

1.1.4 31 Flavors of DFT

Because it is difficult to model electron-electron interactions semi-classically, there are many DFT functionals. There are so many different functionals in DFT that it can be quite daunting to determine what is effective for a given problem, and what each density functional does [7]. Among these, there are three general schemes that need to be discussed. These schemes differ mainly in their definitions of kinetic energy and assumptions about what corrections need to be made to classical electron-electron interactions to account for quantum mechanical effects. The first is the Thomas-Fermi (TF) method, the second is the Kohn-Sham (KS) method, and finally methods that rely on gradient expansions of the KS kinetic energy.

The TF method is the first true density functional theory [3][8][9]. The method assumes the kinetic energy per-particle to be the average kinetic energy of a particle in the Fermi sea of a homogeneous electron gas. The potential energy is the Hartree energy, which is the classical potential energy for a charge density. Consequently, this model accurately describes

a classical homogeneous electron gas. However, this method fails to accurately predict the behavior of most realistic electronic systems outside of the homogeneous electron gas. Most importantly it fails to predict chemical binding [8][10]. Any prediction of actual materials or molecules would require the prediction of chemical bonds. There are corrections to this method that make it more effective, however this scheme is not commonly used. In practice the most commonly used, and accurate, method to robustly predict electronic structure is the KS method [4][5].

The KS ansatz states that one can make accurate electronic structure predictions if one assumes fictitious non-interacting single-particle orbital wave functions and eigenvalues [11]. The electron density is constructed from said wave functions. It is given by

$$n(\mathbf{r}) = \sum_{i=0}^N |\psi_i(\mathbf{r})|^2. \quad (1.1)$$

In practice one constructs an auxiliary Hamiltonian,

$$\hat{H}_{ks} = \sum_{i=0}^N [|\nabla\psi_i(\mathbf{r})|^2] + V_{aux}, \quad (1.2)$$

assuming these fictitious orbitals. It should be noted that the kinetic energy term is

$$T_{ks} = \frac{1}{2} \sum_{i=0}^N \int [|\nabla\psi_i(\mathbf{r})|^2] d^3r. \quad (1.3)$$

Making a reasonable guess of the auxiliary potential, one diagonalizes the Hamiltonian to find the wave functions, and thereby the density. The auxiliary potential is typically the Hartree potential with a correction added. This correction is designed to consider electron-electron interactions that are neglected in both the kinetic energy and in the Hartree energy. The density is then used to construct a total energy. The total energy is then minimized with respect to density, which gives a value for the auxiliary potential. If the calculated auxiliary potential is drastically different from the guessed auxiliary potential, the process is

repeated using the new value of the auxiliary potential [6][11]. The KS ansatz is justifiable as an extension of the Hohenberg and Kohn theorem as a method of finding density, and this method has very accurate practical results.

The downside of the KS method is that the introduction of orbitals creates a computational bottleneck [5][12]. This is due to the fact that every particle needs its own orbital¹. The dimensions of a Hamiltonian for an N particle system is $N \times N$. The number of calculations to diagonalize this matrix then scale as N^3 [3][5]. For large N that becomes a very large number of calculations.

Because of the bottleneck of the KS method, orbital free density functional theories (OFDFT) were developed which were meant to approximate the KS method without orbitals [4][5][12]. This means that instead of the Hamiltonian having $3N$ degrees of freedom, it has simply 3. The gradient expansion approximation (GEA) is one of the earliest attempts to approximate the KS functional without orbitals, and will be explained in detail in the next section. In the context of this section it is sufficient to say that the GEA gives reasonable predictions for highly homogeneous systems, but does poorly for inhomogeneous systems. Many orbital free methods rely on some sort of gradient expansion as a starting point.

These general schemes each make different specific assumptions to correct classical electron-electron interaction energies to include quantum mechanical effects. This means that each general scheme uses different correction functionals. There are many correction functionals that are only used for a single class of problem. With this in mind how do one chose a general method? What methods are the most robust?

¹Of course if one includes spin the occupation of each orbital is 2 not 1

1.2 Applications of DFT

1.2.1 Traditional Applications—Orbital DFT

The classical applications of DFT are in quantum chemistry and in material science. This is because DFT is good at solving problems that can be simplified to several atoms. In the case of quantum chemistry, DFT is very good at predicting dissociation energies, bonding angles, and geometry for simple molecular systems [9][16]. DFT can also be used to model simple proteins [17].

In the materials world, DFT is great for predicting the properties of most solids [18][19]. Due to the highly periodic nature of solids, one can use periodic boundary conditions and calculate the bulk properties of solids by modeling a single repeating unit cell. Many properties like electron mobility and bulk modulus can be determined via these methods.

This makes DFT very good for predicting certain behaviors of solid state devices like transistors [19]. Because of Hund's rules, which govern the order electron states are occupied, and the Kohn-Sham dependence on orbitals, one can even model ferromagnetic transistors or other magnetic states. This is a fantastic feature of DFT in the application of micro/nanoelectronics.

There are, however, limitations to orbital DFT. DFT has a hard time modeling relatively weak interactions like the interaction of induced dipole moments [9][20]. This is bad for many biochemical applications. DFT also models fundamental and optical band gaps poorly [9][20]. Highest Occupied Molecular Orbital Lowest Unoccupied Molecular Orbital (HOMO LUMO) gaps are particularly poorly predicted [21]. These are interesting problems, and a great deal of work is being done to improve these kinds of calculations [9][21].

The most restricting feature of DFT is the fact that the computational cost scales as N^3 . Many interesting problems become simply intractable using DFT because of this bottleneck. That makes OFDFT a very exciting avenue of research.

1.2.2 Large Scale DFT–OFDFT

Because DFTs greatest limitation stems from the fact it scales as N^3 , there are many systems for which traditional DFT is too computationally expensive to use. However if one uses orbital free density functional theory, the bottleneck in traditional DFT is greatly reduced. In fact OFDFT simulations are routinely done with 10^4 atoms, and benchmark tests of 10^6 atoms can be done with relatively modest computational resources [5]. Furthermore modeling high temperature systems is a challenge in traditional DFT. The number of orbitals available to an electron thermally excited to near the top of a potential well is very large. One would need to calculate many thousands or perhaps millions of orbitals to describe a hydrogen atom in a very dense warm environment.

There are many fields and topics that benefit from the ability to calculate a large number of ground-state atoms. One is the study of dislocation mobility [22]. This sort of effect is prevalent in metal that undergoes repeated stresses and strains, for instance support beams in buildings. OFDFT can be used to determine all sorts of material properties that can't be determined simply by analyzing the bulk properties of the material, like elastic properties near surfaces [23]. It can also help to determine large scale material properties based on quantum calculations [24]. This is applicable to fields like quantum dots, carbon nanowires, and nanoelectronics.

A field that could clearly benefit from the high temperature features of OFDFT is the study of warm dense matter [9][25]. Warm dense matter is essentially matter that is too dense to be considered a plasma, but too hot to be considered a solid. This sort of matter is found in gas giants like Jupiter. As previously mentioned, warm matter probes many orbitals. It would require a large amount of computational time to model warm dense matter with orbitals.

Also, as previously mentioned, in biophysics one deals with incredibly complicated many-atom molecules like proteins and DNA. Accurate models of proteins, and protein folding could help cure diseases like sickle-cell anemia, and would have potential applications in

genetics. OFDFT could be used to generate some of these models.

1.3 Current Challenges in OFDFT

It is interesting to note that every example cited for the use of zero temperature OFDFT was used to model a metal. This is because the electrons in a metal act very much like a homogeneous electron gas. This is a feature of metallic bonds. OFDFT kinetic energy models work very well in this limit [3][9]. However OFDFT models don't predict inhomogeneous systems well because they don't perfectly map to the KS model. Because Hohenberg and Kohn [2] proved that there is an exact one-to-one mapping between many-body wave functions and densities, there must be an orbital free density functional that requires only one position variable to exactly replace the KS density functional for any system, even highly inhomogeneous systems. Unfortunately, Hohenberg and Kohn simply prove the mapping exists and give little insight as to what that mapping is [5], and no systematic approach to determine it.

The errors between orbital free functionals and the KS model can stem from only two sources. One is the kinetic energy, the other is the potential energy. Although the potential energy does generate some error, the main source of error is the kinetic energy [5]. The challenge is to model the KS kinetic energy with as much accuracy as possible using orbital free kinetic energy functionals [5][12]. This has been achieved reasonably for certain classes of systems outside of metals. One functional that stands out is the Huang-Carter functional. This functional has shown a great deal of success in predicting properties for semiconductor materials [4][5]. However modeling covalent materials is still a shortcoming of OFDFT at large, due to a covalent bonds inherent inhomogeneity [1][7][12][26]. There are systems where the trade-off in accuracy outweighs the speed of these OFDFT kinetic energy models, while the KS model is still too computationally expensive to use. This is the defining problem of OFDFT, and a major problem in DFT at large.

In the same vein, it would be desirable to accurately model highly orbital dependent phenomena like ferromagnetism [5] using OFDFT. Another highly orbital dependent property that would be beneficial to model would be the HOMO LUMO gap. Although possible, these phenomena would be very difficult for an orbital free functional due to the fact that these phenomena are literally defined by orbitals [1][5].

1.3.1 Research

One of the most orbital dependent and inhomogeneous systems are atoms in the limit of small nuclei. One may wonder why it is necessary to describe single ground-state atoms with OFDFT. Certainly zero temperature atoms with few electrons are systems better modeled by orbital DFT. However, atoms are the building blocks of any molecular or solid state system. More importantly, the core electrons of atoms with large nuclei behave much like homogeneous electron gases. In fact as the nuclear charge approaches infinity, the core of the atom is perfectly described as a homogeneous electron gas. Recall that the TF model perfectly describes a homogeneous electron gas. The KS functional exactly agrees with the TF model in the limit of a homogeneous electron gas. The KS functional also exactly agrees with the TF model when the all electrons are in the ground state. The solution to the TF model when all electrons are in the ground state is called the von-Weizsacker (VW) model. Hydrogen and helium have all electrons in the ground state. This means that if an orbital free functional can describe atoms as they range from small nuclei to very large nuclei, that functional would be a candidate to replace the KS kinetic energy functional.

In 2006, Perdew and Constantin designed an orbital free kinetic energy functional, the mGGA. It is a meta-Generalized Gradient Approximation (GGA) designed to replace the second and fourth-order GEA for describing the kinetic energy of slowly varying electron gases [12]. It was designed with constraints set by the Kohn-Sham kinetic energy, which any orbital free kinetic energy functional should map to. It improved upon the second order GEA by including higher orders, and improved upon the fourth order GEA by solving an

undesirable stability problem that that exists in certain limits.

The greatest feature of the mGGA is that it predicts the proper total energy of atoms as they scale between small and large nuclei. It does this by stitching together the VW functional, which describes very inhomogeneous systems, with their specifically constructed meta-GGA, which describes very homogeneous systems. Perdew and Constantin's meta-GGA was designed to exactly agree with the TF functional in the limit of a homogeneous electron gas, and exactly agree with the VW functional in the limit of Hydrogen and Helium. This suggests that the mGGA is a potential orbital free candidate to replace the KS functional. It is noteworthy to mention that the stitching function used was a non-analytic smooth function.

To a theoretical physicist, the fact that the mGGA uses first principles and physical constraints to match realistic scaling trends in atoms is desirable. This suggests that it may be applied in a variety of systems. It also suggests with careful mathematical manipulation one could potentially modify and improve this model in any areas where its predictive power is poor while preserving the general behavior of the model. This is ideal because there are some shortcomings in this model.

In analyzing the mGGA applied to molecules, the Cancio group found that the mGGA underestimated bonding energies. The Cancio group determined the culprit was the mGGAs stitching function, which had two inflection points. A model, mGGArev, was designed to employ a stitching function which was also smooth, but had only one inflection point [1].

It is the goal of this research to expound on the work of Perdew and Constantin and the Cancio group to stitch together the slowly varying electron gas behavior of the GEA with the highly inhomogeneous behavior of the VW model. The objective of this stitching function is to find a robust mapping from the Kohn-Sham kinetic energy to an orbital free kinetic energy functional. This functional would ultimately have to satisfy all the constraints of the mGGA. Furthermore the total energy of the functional for atoms would need to scale properly as the nuclear charge increased. This will be done by modifying and improving the

mGGArev model.

The improvements to mGGArev will be determined by comparing the Kohn-Sham kinetic energy for single atoms with the kinetic energies of the mGGA and mGGArev models for the same atoms. If the functional being developed accurately predicts the kinetic energy density and total kinetic energy of many various atoms, then it should scale properly with nuclear charge, and should also satisfy all KS constraints. This has the potential to make advancements in accurately modeling kinetic energies using OFDFT.

1.3.2 Outline

It is now prudent to outline the remainder of this thesis. In chapter two, the basic theory of DFT and OFDFT will be introduced. Specific topics required to understand the mGGA and required to develop and improve the mGGArev will be explored, as will their behavior in relation to atoms. In chapter three, the methodology of the research will be explained. The mathematical and programming algorithms required to use and test the improved mGGArev model will also be described. In chapter four the improved mGGArev kinetic energy density model will be compared with other models including the mGGA model. It will also be determined if the mGGArev model offers increased efficacy and accuracy over the mGGA model. The metric by which efficacy and accuracy will be determined is two fold. It will be determined if the mGGArev model has increased agreement with the KS kinetic energy density of single atoms over other orbital free models. It will also be determined if the mGGArev offers an improvement of the scaling behavior of the total kinetic energy for atoms over other orbital free models. Finally in chapter five, final conclusions of the aforementioned analysis will be given, and future work will be suggested.

Chapter 2

Theory

2.1 The Many Body Hamiltonian

In general, a many-electron Hamiltonian can be derived from classical electrodynamics [6] using the Born Oppenheimer approximation [27]. It would take the form

$$\hat{H} = -\frac{1}{2} \sum_i \nabla_i^2 + \sum_{i,I} \frac{Z_I}{|\mathbf{r}_i - \mathbf{R}_I|} + \frac{1}{2} \sum_{i \neq j} \frac{1}{|\mathbf{r}_i - \mathbf{r}_j|} - \frac{1}{2M} \sum_I \nabla_I^2 + \frac{1}{2} \sum_{I \neq J} \frac{Z_I Z_J}{|\mathbf{R}_I - \mathbf{R}_J|}. \quad (2.1)$$

Here Z_I is the charge of the I th nucleus at site \mathbf{R}_I , and \mathbf{r}_i is the position of the i th electron. \mathbf{R}_J and \mathbf{r}_j are the positions of the J th nucleus and the j th electron. M is the relative mass between the nucleus and an electron. ∇_i is the standard vector gradient operator acting on \mathbf{r}_i . It should be noted that in perpetuity

$$\hbar = e = m_e = 4\pi\epsilon_0 = 1. \quad (2.2)$$

The kinetic energy term associated with the nuclei can be neglected, due to the fact that it is dwarfed by the electron kinetic energy term, because of their relative masses. This means that the nuclei are stationary, consequently in this approximation the nuclear-nuclear interaction is a constant added to the total energy and does not affect the electron wave

functions. Therefore the energy expectation is

$$E = \langle \Psi(\mathbf{r}_1, \mathbf{r}_2, \dots, \mathbf{r}_n) | \hat{H} | \Psi(\mathbf{r}_1, \mathbf{r}_2, \dots, \mathbf{r}_n) \rangle + \frac{1}{2} \sum_{I \neq J} \frac{Z_I Z_J}{|\mathbf{R}_I - \mathbf{R}_J|}. \quad (2.3)$$

Note that

$$\Psi(\mathbf{r}_1, \mathbf{r}_2, \dots, \mathbf{r}_n) = \frac{1}{\sqrt{N!}} \begin{vmatrix} \psi_1(\mathbf{r}_1) & \psi_2(\mathbf{r}_1) & \cdots & \psi_N(\mathbf{r}_1) \\ \psi_1(\mathbf{r}_2) & \psi_2(\mathbf{r}_2) & \cdots & \psi_N(\mathbf{r}_2) \\ \vdots & \vdots & \ddots & \vdots \\ \psi_1(\mathbf{r}_N) & \psi_2(\mathbf{r}_N) & \cdots & \psi_N(\mathbf{r}_N) \end{vmatrix} \quad (2.4)$$

is the many-body wave function for the electrons. N is the number of electrons. This form gives the proper anti-symmetrization. It should be noted that Equation 2.4 only describes the behavior of a non-interacting system of identical particles. The behavior becomes even more complicated for interacting particles.

Equation 2.3 is non linear and uses many body wave functions which require N position variables, which makes it non-local. This form is not always ideal for many-electron computational methods due to the non-locality and scaling behavior as the number of electrons is increased [6]. To start simplifying the Hamiltonian at large it is ideal to consider the energy in the form

$$E = \langle \Psi(\mathbf{r}_1, \mathbf{r}_2, \dots, \mathbf{r}_n) | \left(\hat{T} + \hat{V}_{ext} + \hat{V}_{int} \right) | \Psi(\mathbf{r}_1, \mathbf{r}_2, \dots, \mathbf{r}_n) \rangle + E_{II} \quad (2.5)$$

where

$$\hat{T} = -\frac{1}{2} \sum_i \nabla_i^2 \quad (2.6)$$

is the kinetic energy,

$$\hat{V}_{ext} = \sum_{i,I} \frac{Z_I}{|\mathbf{r}_i - \mathbf{R}_I|} \quad (2.7)$$

is the interaction between electrons and the nucleus,

$$\hat{V}_{int} = \frac{1}{2} \sum_{i \neq j} \frac{1}{|\mathbf{r}_i - \mathbf{r}_j|} \quad (2.8)$$

is the electron-electron interaction, and

$$E_{II} = \frac{1}{2} \sum_{I \neq J} \frac{Z_I Z_J}{|\mathbf{R}_I - \mathbf{R}_J|} \quad (2.9)$$

is the nuclear-nuclear interaction.

The goal is to simplify each term of this many body expression using appropriate assumptions. What follows is the explanation and justification of those assumptions.

2.1.1 Hohenberg and Kohn

In the pioneering work of Hohenberg and Kohn [2], they prove by negation that for any unique density $n(\mathbf{r})$ where

$$n(\mathbf{r}) = \langle \Psi | \sum_{i=0}^N \delta(\mathbf{r} - \mathbf{r}_i) | \Psi \rangle, \quad (2.10)$$

there exists a unique external potential $V(\mathbf{r})$. To illustrate this, consider a potential $V'(\mathbf{r})$ different from $V(\mathbf{r})$ that results in same density, $n(\mathbf{r})$. Let $\Psi'(\mathbf{r})$ and $\Psi(\mathbf{r})$ be the respective ground state wave functions, E' and E be the respective ground state energies, and H' and H be the respective ground state Hamiltonians. Because energies are bounded from below by the ground state,

$$E' = \langle \Psi' | H' | \Psi' \rangle < \langle \Psi | H' | \Psi \rangle = \langle \Psi | H + V' - V | \Psi \rangle. \quad (2.11)$$

Equation 2.13 can then be rewritten as

$$E' < E + \int [V'(\mathbf{r}) - V(\mathbf{r})]n(\mathbf{r})dr. \quad (2.12)$$

Because symmetrically

$$E = \langle \Psi | H | \Psi \rangle < \langle \Psi' | H | \Psi' \rangle = \langle \Psi' | H' + V - V' | \Psi' \rangle, \quad (2.13)$$

then

$$E < E' + \int [V(\mathbf{r}) - V'(\mathbf{r})]n(\mathbf{r})dr. \quad (2.14)$$

Adding Equation 2.12 and Equation 2.14 one encounters the paradox

$$E + E' < E + E', \quad (2.15)$$

thus proving there exists a unique potential for each unique ground state density. Because the uniqueness of Hamiltonians depends on their potential, a unique ground state energy can be determined in the form

$$E[n] = T[n] + E_{int}[n] + \int V_{ext}(\mathbf{r})n(\mathbf{r})d^3r + E_{II}. \quad (2.16)$$

This means that there is a universal expression for all ground state systems for $T[n]$ and $E_{int}[n]$ in terms of density functionals, and all uniqueness comes from V_{ext} . Once the universal functionals are known and the unique potential energy is included, any unique ground state system can be determined by minimizing the total energy $E[n]$. Unfortunately Hohenberg and Kohns proof does not give any indication of how one would express the two universal terms or the unique potential energy in terms of density. It simply proves their existence. The next step is to find or approximate expressions of the kinetic energy and the internal potential functionals.

2.2 TF Theory

2.2.1 The Homogeneous Electron Gas

In the case of a homogeneous electron gas, Equation 2.3 can be simplified under the assumption of a uniform positively charged background in place of nuclei [6]. The Energy expectation of an electron gas with positively charged nuclear point charges is

$$E[n] = T[n] + \frac{1}{2} \left[\int \frac{n(\mathbf{r})^2}{|\mathbf{r} - \mathbf{r}'|} d^3r d^3r' + \int \frac{n_+(\mathbf{r})^2}{|\mathbf{r} - \mathbf{r}'|} d^3r d^3r' - 2 \int \frac{n_+(\mathbf{r})n(\mathbf{r})}{|\mathbf{r} - \mathbf{r}'|} d^3r d^3r' \right], \quad (2.17)$$

where $n_+(\mathbf{r}) = \sum_{I=1}^N \delta(r - R_I)$, which is the density of nuclear point charges. It should be noted that \mathbf{r} and \mathbf{r}' are the positions of negative and positive charge densities respectively. This is essentially Equation 2.5. In the case of a homogeneous electron gas with a uniformly charged background the density of both electrons and nuclei are constants. This allows one to simplify Equation 2.17 to

$$\begin{aligned} E[n] - T[n] &= [n^2 + n_+^2 - 2n_+n] \left[\int \frac{1}{|\mathbf{r} - \mathbf{r}'|} d^3r d^3r' \right] \\ &= [n - n_+]^2 \left[\int \frac{1}{|\mathbf{r} - \mathbf{r}'|} d^3r d^3r' \right]. \end{aligned} \quad (2.18)$$

For a homogeneous electron gas of zero net charge, $n_+ = n$. Therefore the only term that survives is the kinetic energy term. An important effect of this semi-classical treatment has yet to be considered however. One must include Pauli's exclusion principle to accurately describe quantum mechanical behavior.

Imagine a homogeneous gas of fermions confined to a volume, L^3 . The wave functions for such a system would have the form $e^{i\mathbf{k}\cdot\mathbf{r}}$. In this case $k = \frac{2m\pi}{L}$, where $m \in \mathbb{N}$. Integrating over a Fermi volume [28] with a normalization chosen such that the Fermi volume has a

wavelength of 1 results in

$$2 \frac{1}{(2\pi/L)^3} \int_0^{k_f} dk^3 = 2 \frac{4\pi}{(2\pi/L)^3} \int_0^{k_f} k_f^2 dk = \frac{L^3 k_f^3}{\pi^2 3} = N, \quad (2.19)$$

where k_f is the Fermi momentum and the factor of two is due to spin degeneracies. It should also be noted that the only allowed wave function is the $m = 1$ case, which confines the wave functions to a single Fermi volume element. One can therefore conclude that

$$k_f = \left(\frac{3\pi^2 N}{V} \right)^{1/3}, \quad (2.20)$$

where $V = L^3$. Integrating over kinetic energy with proper normalization, it can be shown that

$$T = 2 \frac{1}{(2\pi/L)^3} \int_0^{k_f} \frac{k^2}{2} d^3k = 2 \frac{4\pi}{(2\pi/L)^3} \int_0^{k_f} \frac{k^4}{2} dk = \frac{L^3 k_f^5}{\pi^2 10}. \quad (2.21)$$

Finally it can be shown that $\frac{T}{N} = \frac{3}{10} k_f^2 = \frac{3}{5} \epsilon_f$, where $\epsilon_f = \frac{k_f^2}{2}$. Therefore, the average non-interacting kinetic energy of a homogeneous electron gas is defined to be

$$T = \frac{3}{10} N k_f^2 = \frac{3}{10} N (3\pi^2 n)^{2/3}, \quad (2.22)$$

where $n = N/V$.

There are two other consequences of the quantum nature of electron gases that have yet to be explored, exchange and correlation. Imagine any slight perturbation in the homogeneous electron gas. Because of the positively charged background, any perturbation from the homogeneous electron gas would create a region of positive net charge, and a region of negative net charge. This would equate to an electron surrounded by a screening hole [29]. Because of Pauli's exclusion principle, one would expect this sort of effect around every electron in the gas. No two electrons with the same quantum numbers can be found in the same place. This results in regions of reduced probability of finding an electron, which equates to regions of reduced electron density, and therefore a screening hole. The density of

a screening hole in general would be of the form $n_{xc} = n_{xc}(\mathbf{r}, \mathbf{r}')$. Using classical electrostatics one could construct an exchange energy

$$E_{xc} = - \int \frac{n(\mathbf{r}) n_{xc}(\mathbf{r}, \mathbf{r}')}{|\mathbf{r} - \mathbf{r}'|} d^3r d^3r', \quad (2.23)$$

which is the energy of the electron interaction with the screening hole. Note that \mathbf{r} is the position of the electron and \mathbf{r}' is the position of the hole. In the limit of a homogeneous electron gas the density would be $n_{xc}(\mathbf{r} - \mathbf{r}')$, and one could then integrate Equation 2.23 over \mathbf{r}' . For a homogeneous gas the integrand would become $n n_{xc}(\mathbf{r} - \mathbf{r}')$. If the system were split into N equal spheres, one per electron, one could define the radius of a hole as

$$r_s = \left(\frac{3}{4\pi n} \right)^{1/3} = \frac{3\pi}{4} \frac{1}{k_f}. \quad (2.24)$$

The total energy of a homogeneous electron gas becomes

$$E = \frac{3}{10} N (3\pi^2 n)^{2/3} - A \frac{N}{r_s}. \quad (2.25)$$

This expression is in terms of entirely extrinsic and intrinsic properties, N and n respectively.

2.2.2 The Slowly Varying Electron Gas

Describing a homogeneous electron gas is not particularly beneficial, as few real world systems are well modeled as homogeneous electron gases. It would be useful to be able to describe more complicated systems. Typically small variations in a Hamiltonian would use perturbative approximations similar to the adiabatic approximation or Wentzel Kramers Brillouin (WKB) approximation [30]. In the case of a slowly varying electron density, one such approximation is the aptly named slowly varying electron gas approximation. It should be noted that this approximation is not perturbative, but like the adiabatic approximation or WKB, it depends on the system being slowly varied.

Imagine a mesh of finite volume elements, each defined as a homogeneous electron gas, such that the density of each volume element is homogeneous, but the density can vary slightly from volume element to volume element. This would essentially describe a slowly varying electron gas [28]. However this is only a reasonable approximation in the limit that follows.

A variation in a density could be called large about a point r_0 in the case where

$$\nabla n(\mathbf{r}_0) \cdot \delta \mathbf{r} = n(\mathbf{r}_0) \quad (2.26)$$

given that $|\delta \mathbf{r}| = L$. It should be mentioned that ∇ in this context is a gradient, however it cannot be considered an operator in the same manner as it is in Equation 2.1. The finite difference analogue is $n(\mathbf{r}_1) - n(\mathbf{r}_0) = n(\mathbf{r}_0)$ over a single step L . This is large because it equates to a relative error of one over a single step for a system that is supposed to be near homogeneous. In order to ensure that a slowly varying system behaves like a homogeneous electron gas on this length scale, one needs to ensure that $k_f \gg \frac{1}{L}$. In fact one would want $1/L$ to be orders of magnitude less than k_f [20].

In this approximation of a slowly varying electron gas, one can now map $\delta N \rightarrow n(\mathbf{r})dV$ in Equation 2.25, which maps the number of electrons in a finite box to differential density. One can now also map $V \rightarrow \int d^3r$, which maps the volume of a box to a differential volume. Both $n(\mathbf{r})dV$ and $\int d^3r$ are entirely intrinsic variables. The other intrinsic variables would no longer be constant. In this case the average kinetic energy density becomes

$$\tau_{tf} = \frac{3}{10}(3\pi^2)^{2/3}n(\mathbf{r})^{5/3}. \quad (2.27)$$

The average total kinetic energy becomes

$$T_{tf} = \int \tau_{tf}d^3r = C_1 \int n(\mathbf{r})^{5/3}d^3r, \quad (2.28)$$

where $C_1 = \frac{3}{10}(3\pi^2)^{2/3}$ [6].

To describe the interactions between classical electron densities, which are no longer constant in a slowly varying electron gas, one can use the Hartree energy

$$E_H = \frac{1}{2} \int \frac{n(\mathbf{r}')n(\mathbf{r})}{|\mathbf{r} - \mathbf{r}'|} d^3r d^3r'. \quad (2.29)$$

This is essentially the classical electrostatic energy.

Treating electrons as charge densities has no features of their particle nature. It is necessary to discuss the exchange and correlation energies. Replacing N with $n(\mathbf{r})$ into the exchange term in Equation 2.25, which is the local density approximation [6], gives

$$E_x = A \int \frac{n(\mathbf{r})}{r_s} d^3r. \quad (2.30)$$

The exchange energy can then be expressed as

$$E_x = A \int \left[\frac{9\pi n(\mathbf{r})^4}{4k_f^3} \right]^{1/3} d^3r = \int C_2 n(\mathbf{r})^{4/3} d^3r, \quad (2.31)$$

where $C_2 = -\frac{3}{4}\left(\frac{3}{\pi}\right)^{1/3}$. This approximation only describes exchange with no correlation, and is an approximation to exchange.

There exists a single body wave function approximation that describes exact exchange, the Hartree-Fock (HF) method. The HF method is discussed in appendix C. It should be noted that TF did approximate correlation. The approximation was based on the idea of the response of the screening hole to a charged particle with momentum k outside the system [6]. The Fourier transform of this response at wave vector k is a Yukawa type Equation. This is, however, not relevant to the current discussion, and more importantly it doesn't work very well so it will not be discussed further here. It is noteworthy that there are many functionals in modern DFT that simultaneously describe correlation and exchange that are highly accurate [7].

The final element of the Hamiltonian that needs to be discussed is the interactions between the electrons and the uniform background. Once again considering the classical electrostatic energy

$$E_{ext} = \int \frac{n_+(\mathbf{r})n(\mathbf{r})}{|\mathbf{r} - \mathbf{r}'|} d^3r d^3r' = \int V_{ext}(\mathbf{r})n(\mathbf{r})d^3r. \quad (2.32)$$

2.2.3 The TF Energy

Summing each of these terms (neglecting correlation) the TF-Dirac energy is then [6]

$$\begin{aligned} E_{tf}[n(\mathbf{r})] = & C_1 \int n(\mathbf{r})^{5/3} d^3r + \int V_{ext}(\mathbf{r})n(\mathbf{r})d^3r \\ & + C_2 \int n(\mathbf{r})^{4/3} d^3r + \frac{1}{2} \int \frac{n(\mathbf{r}')n(\mathbf{r})}{|\mathbf{r} - \mathbf{r}'|} d^3r d^3r'. \end{aligned} \quad (2.33)$$

Note that square brackets in this context indicate a functional instead of a function. Now that the total energy is in terms of density functionals, and there are expressions for the universal functionals, the next step is to minimize the energy to determine the ground state. In order to ensure proper normalization, a minimization constraint condition is chosen such that integrating over the charge density gives the total number of electrons,

$$\int n(\mathbf{r})d^3r = N. \quad (2.34)$$

Using the method of Lagrange multipliers [6], the functional

$$\Omega_{tf}[n] = E_{tf}[n] - \mu \left\{ \int n(\mathbf{r})d^3r - N \right\} \quad (2.35)$$

is minimized using a functional derivative [6]. Functional derivatives are different than a standard derivative. Functional derivatives are analogous to the derivation of the Euler-Lagrange Equation. If one considers a path in a function space $S = \int L[x, f(x), f'(x)]dx$ and minimizes it $\frac{\delta S}{\delta f(x)} = \frac{\partial L}{\partial f} - \frac{d}{dx} \frac{\partial L}{\partial f'(x)}$, the units of the result are not $\frac{S}{f(x)}$ but rather $\frac{L}{f(x)}$. Martin's book [6] gives a good description of this in appendix A. If one considers the

minimization of each term individually then

$$V_x(\mathbf{r}) = \frac{\delta E_x}{\delta n(\mathbf{r})} = C_2 \frac{4}{3} n(\mathbf{r})^{1/3}, \quad (2.36)$$

$$V_{ext}(\mathbf{r}) = \frac{\delta E_{ext}}{\delta n(\mathbf{r})} = - \int \frac{n_+(\mathbf{r}')}{|\mathbf{r} - \mathbf{r}'|} d^3 r', \quad (2.37)$$

and

$$V_H(\mathbf{r}) = \frac{\delta E_H}{\delta n(\mathbf{r})} = \int \frac{n(\mathbf{r}')}{|\mathbf{r} - \mathbf{r}'|} d^3 r'. \quad (2.38)$$

Equation 2.35 when minimized is then

$$\begin{aligned} \frac{\delta \Omega_{tf}}{\delta n(\mathbf{r})} &= \int \{ \Omega_{tf}[n(\mathbf{r}) + \delta n(\mathbf{r})] - \Omega_{tf}[n(\mathbf{r})] \} d^3 r \rightarrow \\ &\int \left\{ \frac{5}{3} C_1 n(\mathbf{r})^{2/3} + V(\mathbf{r}) - \mu \right\} \delta n(\mathbf{r}) d^3 r = 0. \end{aligned} \quad (2.39)$$

In this context $V(\mathbf{r}) = V_{ext}(\mathbf{r}) + V_H(\mathbf{r}) + V_x(\mathbf{r})$ and μ is the chemical potential. This Equation must hold true for any $\delta n(\mathbf{r})$, therefore

$$\frac{5}{3} C_1 n(\mathbf{r})^{2/3} + V(\mathbf{r}) - \mu = 0. \quad (2.40)$$

It is important to note that $\frac{5}{3} C_1 n(\mathbf{r})^{2/3} = \epsilon_f$, where ϵ_f is the Fermi-energy. Equation 2.40 can then be rewritten as

$$\epsilon_f + V(\mathbf{r}) = \mu. \quad (2.41)$$

This means that if $V(\mathbf{r})$ is zero, ϵ_f becomes the exact energy required to add a single electron to the system by the definition of chemical potential.

Unfortunately the TF model doesn't allow molecular binding. This is a major flaw in the TF model. There are similar models relating to the TF model, most notably the von Weizacker model. This model also doesn't quite fix the binding problem, in that it allows binding, but gives inaccurate energy densities for highly homogeneous systems. Although it

can be derived from the TF model it is more elegantly derived from the KS model, so it will be discussed later in the corresponding section.

Nota Bene : At this point it is sufficient to say "It can be shown that the TF model doesn't allow molecular binding", and move on to the next topic. It is, however, interesting to show why this potential doesn't bind. Appendix E discusses the binding problem at length for the edification of the dedicated reader, and for the pedagogy and history of modeling OFDFT kinetic energy. This topic has no direct bearing on this research but it is didactic and can illuminate certain subtleties of chemical binding in DFT that will be important later in the chapter.

2.3 Kohn and Sham Method

2.3.1 Orbitals

It should be unclear at this point if it is the internal interaction energy or kinetic energy that causes the failure to bond in the TF model. The KS ansatz [6][11] states that if the TF model is replaced with a single body kinetic energy that depends on fictitious non-interacting orbitals and some auxiliary potential, the exact ground state density can be found. The Hamiltonian is then

$$\hat{H}_{aux} = -\frac{1}{2}\nabla^2 + V_{aux}(\mathbf{r}), \quad (2.42)$$

where the density of the system is

$$n(\mathbf{r}) = \sum_{i=0}^N |\psi_i(\mathbf{r})|^2. \quad (2.43)$$

This means that if one can describe the auxiliary potential, one can exactly find the ground state density. In order to find the auxiliary potential, one guesses a potential, and solves the

KS Equation [11]

$$\hat{H}_{aux} |\psi_i(\mathbf{r})\rangle = E_{ks} |\psi_i(\mathbf{r})\rangle. \quad (2.44)$$

The expectation value of the kinetic energy is

$$T_{ks} = \frac{1}{2} \sum_{i=0}^N \int [|\nabla\psi_i(\mathbf{r})|^2] d^3r, \quad (2.45)$$

and the total energy in the KS model takes the form

$$E_{ks} = \frac{1}{2} \sum_{i=1}^N \int [|\nabla\psi_i(\mathbf{r})|^2] d^3r + E_{aux}[n(\mathbf{r})], \quad (2.46)$$

where $E_{aux} = E_H + E_{ext} + E_{xc}$. E_{xc} is a functional meant to describe the exchange and correlation energies neglected in the functions of potential and kinetic energy. One then minimizes the energy to find the auxiliary potential

$$V_{aux}(\mathbf{r}) = \frac{\delta E_{aux}}{\delta n(\mathbf{r})}. \quad (2.47)$$

Then one compares the computed potential to the guessed potential in a self-consistent loop until one converges on the correct auxiliary potential. The KS ansatz is an extension of the Hohenberg and Kohn proof, empirically it holds quite well, and most importantly it binds correctly.

It should be noted that one might expect the kinetic energy expectation to take the form

$$\frac{1}{2} \sum_{i=0}^N \int \psi_i^*(\mathbf{r}) \nabla^2 \psi_i(\mathbf{r}) d^3r. \quad (2.48)$$

Equation 2.45 and Equation 2.48 are equivalent. To prove this consider Green's first identity,

$$\frac{1}{2} \sum_{i=0}^N \int \psi_i^*(\mathbf{r}) \nabla^2 \psi_i(\mathbf{r}) d^3r = \frac{1}{4} \int \nabla^2 n(\mathbf{r}) d^3r - \frac{1}{2} \sum_{i=0}^N \int |\nabla\psi_i(\mathbf{r})|^2 d^3r, \quad (2.49)$$

bearing in mind that

$$\sum_{i=0}^N \psi^*(\mathbf{r}) \nabla \psi(\mathbf{r}) = \frac{1}{2} \nabla n(\mathbf{r}). \quad (2.50)$$

The Laplacian of the density integrates to zero. Using the divergence theorem results in

$$\frac{1}{4} \int \nabla^2 n(\mathbf{r}) d^3r = \frac{1}{4} \oint \nabla n(\mathbf{r}) \cdot d\mathbf{A}, \quad (2.51)$$

which integrates to zero due to the fact that the system is a slowly varying electron gas of finite size and the closed surface is at infinity.

Because the Hartree potential was used, this illustrates that it is in fact the TF kinetic energy functional that fails to bind, not the Hartree functional. It is the non-interacting orbital feature of the kinetic energy that is key to the success of the KS model. One can introduce corrections into the TF model ad infinitum, but it will all be for naught if the non-interacting kinetic energy isn't corrected in some way that addresses orbitals. TF will incorrectly estimate the non-interacting kinetic energy no matter what exchange and correlation corrections one uses.

There is now an expression for a single body model that uses fictitious orbitals, replaces the TF kinetic energy, solves the binding problem, and gives the internal interaction universal functional in the limit of accurate exchange and correlation corrections. The problem is that orbitals were introduced, and these orbitals are required to construct the density, which increases computational cost. The goal then, is to consider orbital free kinetic energy density functionals that map to the KS kinetic energy.

2.3.2 The von Weizsacker Approximation

Before orbital free KS approximations are discussed, it is necessary to discuss the case of the KS model where the system is bosonic instead of fermionic. In a zero temperature Bose

system, all particles will be in the lowest energy eigen state. In this case

$$n(\mathbf{r}) = N|\psi_0(\mathbf{r})|^2. \quad (2.52)$$

Plugging Equation 2.52 into Equation 2.50 it can be shown that

$$\nabla\psi_0(\mathbf{r}) = \frac{\nabla n(\mathbf{r})}{2N\psi_0(\mathbf{r})}. \quad (2.53)$$

From Equation 2.45 it can be shown that

$$\tau_{ks} = \frac{1}{2} \sum_{i=0}^N |\nabla\psi_i(\mathbf{r})|^2 \rightarrow \frac{N}{2} |\nabla\psi_0(\mathbf{r})|^2, \quad (2.54)$$

if all the wave functions in Equation 2.54 are in the ground state. It follows that

$$\tau_{vw} = \frac{|\nabla n(\mathbf{r})|^2}{8N|\psi_0(\mathbf{r})|^2} = \frac{|\nabla n(\mathbf{r})|^2}{8n(\mathbf{r})}, \quad (2.55)$$

which is the VW kinetic energy density [6]. It should be noted that one can minimize the total energy in the same way as was done for the TF model. Minimizing a gradient is not exactly trivial, but there is an analytical minimization of the VW total energy. This is achieved using Green's theorem and integration by parts. This yields a result which describes bosonic systems in exact agreement with the KS model.

Also because zero temperature H and He only have at most 2 electrons in the lowest energy eigenstate, the VW functional models those atoms with perfect agreement to the KS model. In fact it models any system with only electron singlets, electron pairs that have zero net spin, perfectly. For instance systems like H₂. Because it works perfectly for electron singlets, it also works reasonably well for covalent bond energies, and any system that has very high inhomogeneity.

This method can also be extended to fermions at large if one uses a kinetic energy

correction τ_{tfvw} that uses some sort of variational method $\lambda\tau_{vw} + \tau_{tf} = \tau_{tfvw}$ [20]. The idea is to turn on the TF energy for highly homogeneous regimes, then turn on the VW energy for inhomogeneous regimes. This sort of approach has been used widely in the field [20]. It is now prudent to begin the discussion of orbital free KS models, and the current state of density functionals for kinetic energy.

2.4 Kohn and Sham Method, Orbital Free

2.4.1 Models of the KS Kinetic Energy

Because of the success of the KS model in fields like quantum chemistry and material science, it is known that the KS kinetic energy is a realistic model. The problem is the orbitals. The canonical KS model is too computationally expensive for large molecules and other complex systems [12]. If there are 1000 electrons one must calculate 500 orbitals. Although this is a great improvement over many body calculations it is still too complex for some applications. Luckily, it is also known because of Hohenburg and Kohn [2] that the KS kinetic energy has a mapping to an orbital free density functional, thereby eliminating orbitals all together. The challenge is to find said mapping [7].

2.4.2 The Gradient Expansion

In the interest of brevity, the formal derivation of the GEA [14][15] will not be discussed. To gain some intuition, however, consider a homogeneous electron gas that is perturbed by a small potential that is periodic with a wave vector $e^{i\mathbf{G}\cdot\mathbf{r}}$. Then consider the wave function $e^{i\mathbf{k}\cdot\mathbf{r}}$. The response of this wave function to the perturbing potential will be to diffract under the Bragg condition $(\mathbf{k} + \mathbf{G})^2 = k^2$ [28]. This is essentially the same as creating a band gap

in the kinetic energy. In this case [2]

$$\sum_G \Delta E = \sum_G G^2 f[n] + \mathcal{O}(G^4) + \dots \quad (2.56)$$

and

$$n(\mathbf{r}) = \sum_G n_0 + \delta n_G e^{i\mathbf{G}\cdot\mathbf{r}}. \quad (2.57)$$

Equation 2.56 when Fourier transformed generates a gradient expansion of all even orders because $\frac{d}{dr} e^{i\mathbf{G}\cdot\mathbf{r}} = iG e^{i\mathbf{G}\cdot\mathbf{r}}$. Therefore via a Fourier transform of Equation 2.56 and Equation 2.57 one can construct an expansion of even orders of gradients of $n(\mathbf{r})$ [20].

The GEA can be parametrized using

$$p = \frac{|\nabla n(\mathbf{r})|^2}{4k_f^2 n(\mathbf{r})^2}, \quad (2.58)$$

and

$$q = \frac{\nabla^2 n(\mathbf{r})}{4k_f^2 n(\mathbf{r})}. \quad (2.59)$$

These are scale invariant unitless parameters. When discussing GEAs it is most common to use the second order gradient expansion

$$\tau_{GEA2} = [1 + \frac{5}{27}p + \frac{20}{9}q]\tau_{tf}. \quad (2.60)$$

However the fourth order expansion

$$\tau_{GEA4} = \tau_{GEA2} + \Delta_4 \tau_{tf}, \quad (2.61)$$

where Δ_4 is

$$\Delta_4 = \frac{8}{81}q^2 - \frac{1}{9}pq + \frac{8}{243}p^2, \quad (2.62)$$

is used as well. Models can be written using an enhancement factor [7],

$$\tau_{model} = F_{model}\tau_{tf}. \quad (2.63)$$

It is important to note that not only can gradient expansions be written this way, but τ_{vw} can be as well, where $F_{vw} = \frac{5}{3}p$.

It is beneficial to compare enhancement factors in a manner that allows one to determine whether the behavior is fermionic or bosonic for various values of p and q , or equivalently more homogeneous or inhomogeneous. This behavior can be determined by constructing a Pauli enhancement factor

$$F_{model}^p = F_{model} - F_{vw}. \quad (2.64)$$

For the research discussed in chapter four, it is convenient to further parametrize the GEA2 using

$$z = \frac{20}{9}q - \frac{40}{27}p. \quad (2.65)$$

The second order Pauli enhancement factor can be written as

$$F_{GEA2}^p(z) = F_{GEA2} - F_{vw} = 1 + z. \quad (2.66)$$

This allows one to construct a parameterization where, when $z = 0$, $F_{model}^p(z)$ is at the TF limit, and when $F_{model}^p = 0$ the model may be exhibiting bosonic behavior. This will be seen a great deal in chapter four.

2.4.3 Constraints on the KS Kinetic Energy

Constraints are useful analytical tools to develop theoretical models. It is not always clear how to exactly model the behavior of a system, however it is possible to consider the behavior of a system at mathematical asymptotes or extrema and build a model that exhibits the same behaviors in the same limits. The assumption then, is that the resulting model will

exhibit similar behavior to the system in question in a wide range of circumstances. The KS kinetic energy, as well as any mapping or approximation to the KS kinetic energy, has a number of constraints [3][12].

1) $T_{ks} \geq T_{vw}$,

2) $\tau_{ks}(\mathbf{r}) \geq \tau_{vw}(\mathbf{r})$,

3) $T_{ks} = T_{vw}$ for $N < 2$,

4) $\tau_{ks}(\mathbf{r}) = \tau_{vw}(\mathbf{r})$ for $N < 2$,

5) $\tau_{ks}(\mathbf{r}) \rightarrow \tau_{tf}(\mathbf{r})$ for a homogeneous electron gas, where τ_{tf} is given by Equation 2.27,

and

6) $\tau_{ks}(\mathbf{r}) \rightarrow \tau_{GEA2}(\mathbf{r})$ for a near homogeneous electron gas.

Constraints 1-4 come from the fact that the energy of a gas of N fermions must be greater than the energy of N bosons if both are confined in the same space, due to Pauli's exclusion principle. Constraint 5 is self evident from the definition of the TF model. Constraint 6 comes from the fact that the first term of the gradient expansion is the TF kinetic energy.

The KS model fits those constraints automatically. Many approximations, including the GEA, fail constraints 3 and 4. This is because many models rely on some kind of gradient expansion. Gradient expansions do not approach the von Weizacker limit, which is to say gradient expansion models do not asymptotically approach a lower bound energy derived from a system where all particles are in the ground state. However, for very homogeneous systems gradient expansions do quite well.

2.5 Perdew and Constantin

2.5.1 The Enhanced Gradient Expansion

Perdew and Constantin set out to accurately calculate the total kinetic energy of all atoms using density functional theory, in the hopes of using their kinetic energy density in DFT models. They took a number of steps to build a constraint based model. The first step that Perdew and Constantin took was to modify the fourth order gradient expansion such that

$$\tau_{G_{EA}enhanced} = \frac{\tau_{G_{EA4}}}{\sqrt{1 + K^2}}, \quad (2.67)$$

where

$$K = \frac{\Delta_4}{1 + \frac{5}{3}p(\mathbf{r})}. \quad (2.68)$$

This modified gradient expansion has several pleasing features [12]. First, in the limit of a slowly varying density with small p and q , $F_{G_{EA}enhanced} \rightarrow F_{G_{EA4}}$ which more accurately describes a near homogeneous electron gas than $F_{G_{EA2}}$. This satisfies constraints 5 and 6. $F_{G_{EA}enhanced}$ satisfies constraint 5 by construction at $p = q = 0$. Second, in the case of very large p and q $|F_{G_{EA}enhanced}| < |F_{G_{EA4}}|$ which is necessary because for very large p and q $F_{G_{EA4}}$ can grow to infinity, which is not physical. Finally, $F_{G_{EA}enhanced} \rightarrow 1 + F_{vw}$ as $q \rightarrow \infty$ and goes to $F_{vw} + \mathcal{O}(p^0)$ as $p \rightarrow \infty$ both of which are greater than F_{vw} . All these limits put together show that constraint 3 is satisfied, because p is positive definite, and $q(n)\tau_{tf}^{5/3} = A\nabla^2 n(\mathbf{r})$ where A is some constant. Recall that the Laplacian of the density integrates to zero. This enhanced gradient expansion does not satisfy constraint 4, because the limit as $q \rightarrow -\infty$ is not F_{vw} . This means that although $\int \tau_{mGGA} d^3r > \int \tau_{vw} d^3r$, locally the kinetic energy density can go below the VW limit. $F_{G_{EA}enhanced}$, however, still offers an improvement over the canonical $F_{G_{EA2}}$, and also over $F_{G_{EA4}}$.

2.5.2 The mGGA Stitching Function

The second improvement Perdew and Constantin made was to use a smooth stitching function to stitch between the enhanced gradient expansion and the VW limit,

$$F_{mGGA} = F_{vw} + (F_{GGA_{enhanced}} - F_{vw})f_{ab}(z'). \quad (2.69)$$

The smooth stitching function is given by

$$f_{ab}(z') = \begin{cases} 0, & z' \leq 0 \\ \left[\frac{1+e^{a/(a-z')}}{e^{a/z'}+e^{a/(a-z')}} \right]^b, & 0 < z' < a \\ 1, & z' \geq a \end{cases}, \quad (2.70)$$

where $0 < a \leq 1$ and $b > 0$. The turning point is defined as

$$z' = F_{GGA_{enhanced}} - F_{vw}. \quad (2.71)$$

This means that Perdew and Constantin stitched together a function that accurately describes homogeneous systems to a function that describes very inhomogeneous systems. This effectively gives the proper asymptotic behavior as $q \rightarrow -\infty$, meaning that the function approaches the VW limit. This satisfies constraint 4, which gradient expansions alone do not. One of the interesting aspects of the F_{mGGA} is that it is smooth. One can take as many derivatives as one would like, and there are no left hand or right hand limit problems because the contribution from the stitching function is zero¹.

2.5.3 Critique of the mGGA Stitching Function

There are however valid criticisms of the mGGA stitching function. These criticisms will be expounded upon in Chapter 4. They are simply stated as follows. The Cancio group visually

¹The reason it is always zero is because $\frac{d^n}{dz^n} e^{-1/z} = \left[\frac{A}{z^{n+1}} + \frac{B}{z^{n+2}} + \dots + \frac{Y}{z^{2n}} \right] e^{-1/z}$. This is clearly always zero when evaluated at the origin. This is called a smooth non-analytic function.

investigated p and q for various molecules [1], as well as τ_{ks} and τ_{mGGA} . They discovered the mGGA gives poor binding energies for single covalent bonds [1]. This can be seen by comparing Figures 2.1(a) and 2.1(b). Each Figure is taken from the Cancio Group [1]. Note how the mGGA underestimates the kinetic energy in bonding regions.

In this analysis, it became clear that negative Laplacians strongly correlate to single covalent bonds as seen in Figure 2.2. This Figure is also taken from the Cancio Group [1]. The link between negative Laplacians and binding will be expounded upon in chapter four, however there is a paper by Bader that gives insight into this phenomenon [31].

It was also realized that the reason the kinetic energy was low was because F_{mGGA} approaches the VW limit quite rapidly, so negative Laplacians give less contribution to the kinetic energy density than they should in binding regions. This can be seen in Figure 2.3. Note how quickly the mGGA goes to zero for negative q . This is likely why the mGGA underestimates kinetic energies in bond regions.

Finally the Cancio group noted that although the mGGA stitching function is smooth, it has two turning points. As far as the author is aware there is no physical justification for this. The two turning points create features in kinetic energy densities that seem unphysical, as will be seen in chapter four. Motivated by some of these shortcomings, the conclusion was reached that a more physical stitching function was required to predict accurate bond energies.

The Cancio groups conjecture was that a functional that had only one turning point,

$$F_{mGGA_{rev}} = 1 + F_{vw} + z[1 - \Theta(-z)e^{-1/|z|}], \quad (2.72)$$

would improve bonding energies. This gives a hockey stick shape which can be seen in Figure 2.3. It is the goal of the research presented in this thesis to improve on the F_{mGGA} stitching function and generate a better mapping of an orbital free density functional to τ_{ks} , using this hockey stick shaped stitching curve.

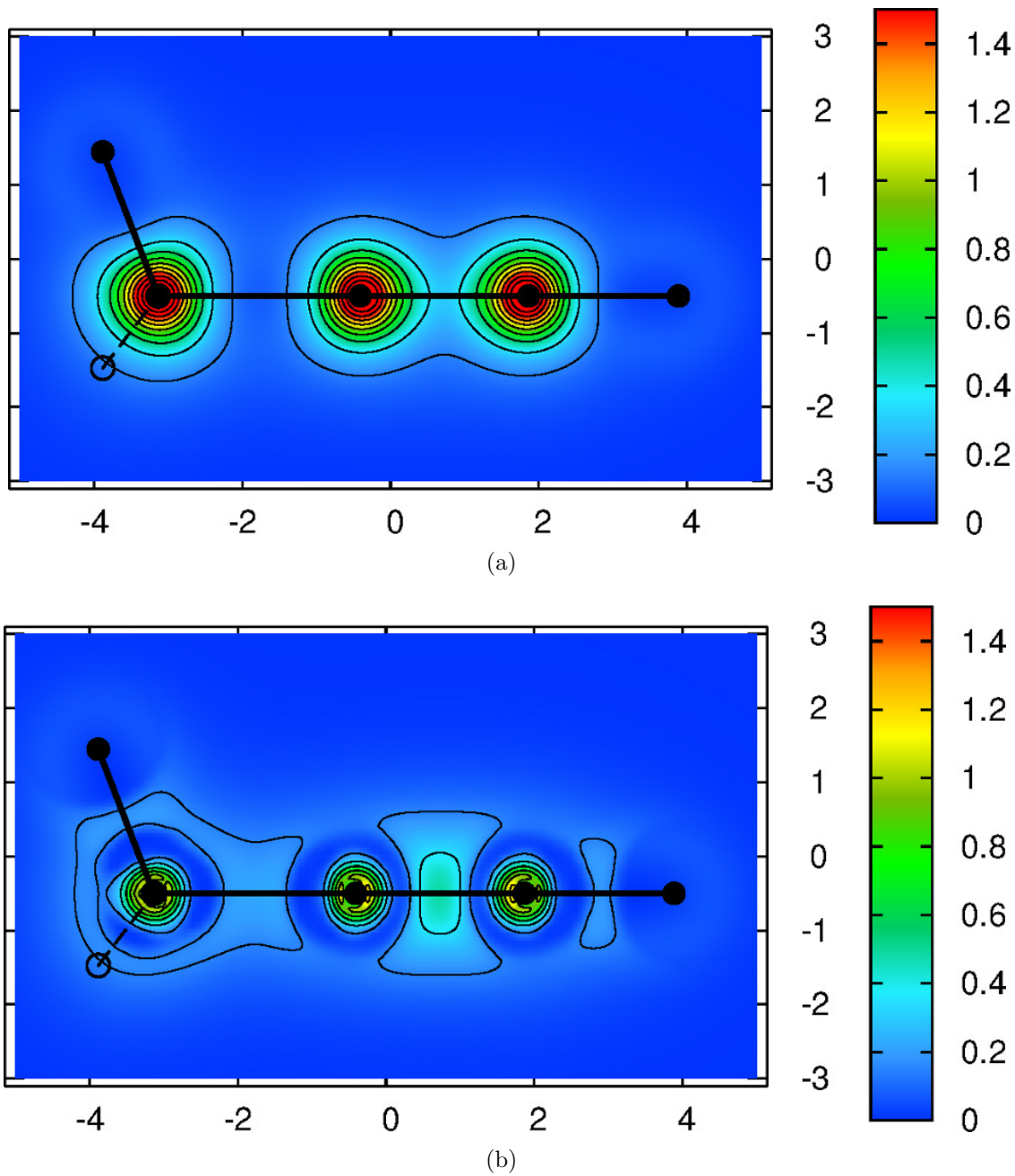


Figure 2.1: **(a)** This is a plot of $\tau_{ks}(\mathbf{r})$ for C_3H_4 using an LDA pseudo-potential. This is a cross section of the C-C-C bond axis and two hydrogens. In-plane atoms and bonds are shown as black disks and line segments; out of plane ones as dashed lines and open disks. This Figure is taken from the Cancio group [1]. **(b)** This is a plot of $\tau_{mGGA}(\mathbf{r})$ for C_3H_4 . This is the same cross section as in Figure 2.1(a). The contour color scale is also the same.

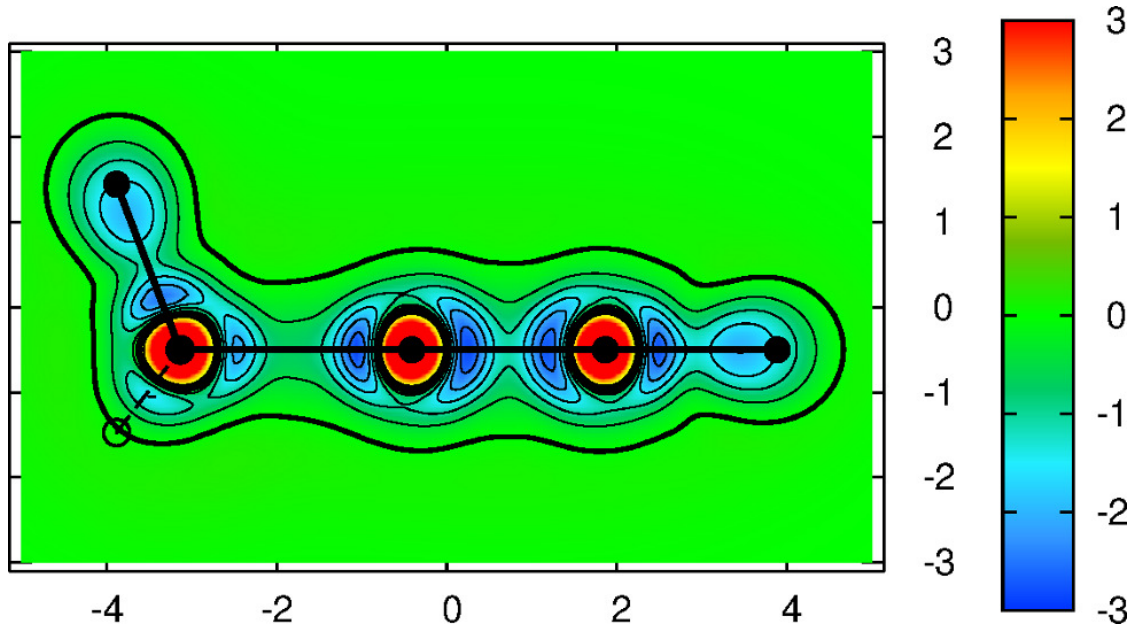


Figure 2.2: This plots $\nabla^2 n(\mathbf{r})$ for C_3H_4 as generated by the KS model with a LDA. This is the same cross section as in Figure 2.1(a).

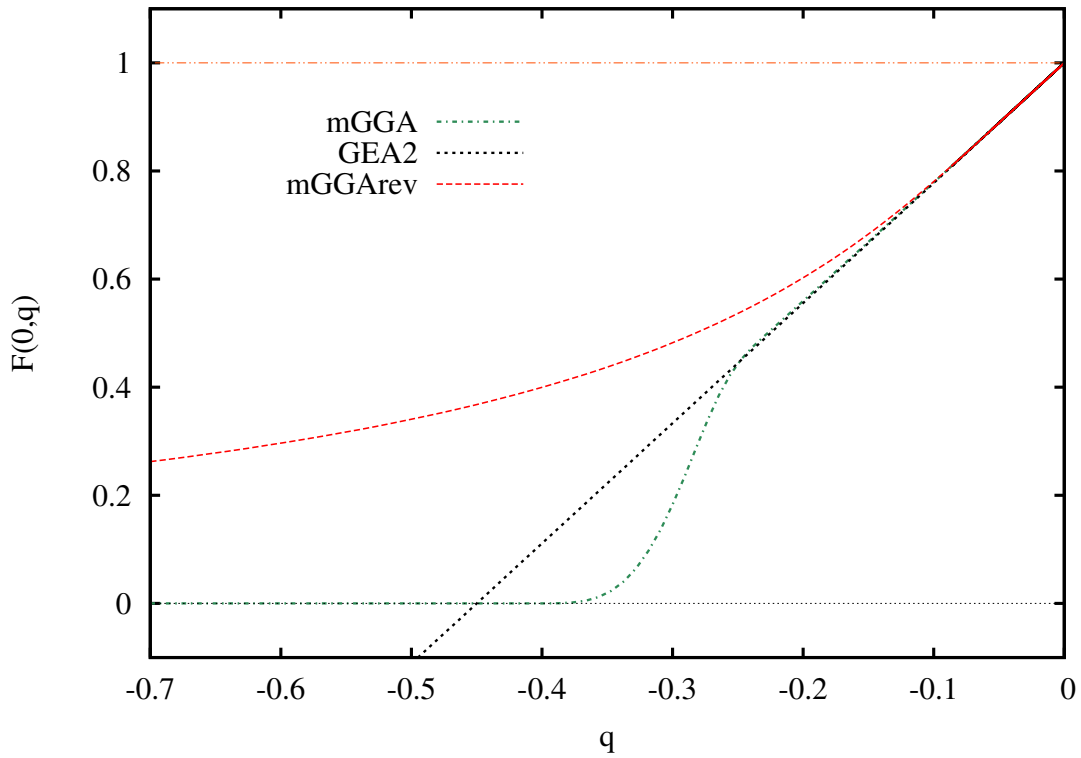


Figure 2.3: This plots $F_{mGGA}(0,q)$, $F_{mGGArev}(0,q)$, and $F_{GEA2}(0,q)$ vs $q(\mathbf{r})$. The black line is the VW limit and the red line is the TF limit.

Very briefly it necessary to analyze Equation 2.72 as z approaches various limits. For $z > 0$ it can be shown that

$$F_{mGGA_{rev}} = 1 + F_{vw} + z, \quad (2.73)$$

which is exactly F_{GEA2} . In the case where $0 > z \gg -1$

$$F_{mGGA_{rev}} = 1 + F_{vw} + z[1 - e^{-\infty}] = 1 + F_{vw} + z, \quad (2.74)$$

which is again exactly F_{GEA2} . This proves there is no discontinuity. For $z \rightarrow -\infty$, let $u = \frac{1}{|z|}$. Then

$$\begin{aligned} F_{mGGA_{rev}} &= 1 + F_{vw} + z [1 - e^{-u}] \approx \\ &1 + F_{vw} + z[1 - (1 - u)] = 1 + F_{vw} + \frac{z}{|z|} = F_{vw} \end{aligned} \quad (2.75)$$

which is the exact limit required by the KS constraints.

2.6 The KS Model for Atoms

Studying the behavior of atoms as the nuclear charge increases is a very elegant way of testing the efficacy and robustness of any specific OFDFT model. First, any density functional should be bounded from below by the VW functional. Recall that the VW functional and the KS functional exactly agree in the case of hydrogen and helium. Second, as the nuclear charge of atoms increases, the core electrons of the atom behave more and more like a homogeneous electron gas. Baer's online textbook gives an elegant proof of this [8]. This is also discussed indirectly in appendix D and in chapter four. For the current purposes, it is sufficient to state that as $Z \rightarrow \infty$ the core electrons of an atom behave exactly like a homogeneous electron gas. This means that if a density functional model were to reasonably predict the kinetic energies of all atoms on the periodic table, it may be able to accurately predict both inhomogeneous and homogeneous systems. This would make it a good candidate

to replace the KS model. At this juncture then, the application of the KS model to atoms must be discussed.

As a review of atomic physics, it is necessary to examine the Schrödinger Equation. The Schrödinger Equation,

$$E\psi(\mathbf{x}, \mathbf{y}, \mathbf{z}) = -\frac{1}{2}\nabla^2\psi(\mathbf{x}, \mathbf{y}, \mathbf{z}) + V\psi(\mathbf{x}, \mathbf{y}, \mathbf{z}), \quad (2.76)$$

can be used to find the wave functions for any quantum mechanical system. For atoms, one needs to separate the equation into radial and angular parts via separation of variables. The solutions to the angular parts for a single-electron atom are well known and won't be discussed here. The radial part, which is the part necessary for this discussion, is

$$Eu_{n,l}(r) = \left\{ \frac{1}{2} \left[-\frac{d^2}{dr^2} + \frac{l(l+1)}{r^2} \right] - \frac{Z}{r} \right\} u_{n,l}(r), \quad (2.77)$$

where $u_{n,l}(r) = rR_{n,l}(r)$, n is the principle quantum number, l is the angular momentum quantum number, and $R_{n,l}(r)$ is the radial wave function. In this context r is still essentially the position of an electron, but because of the separation of variables it can be considered a scalar.

The solutions to this single-electron equation are spherical wave functions. Individual eigenvalues correspond to individual orbitals. The first eigenvalue solution for $n = 1, l = 0$ is the 1s orbital. The second eigenvalue solution for $n = 2, l = 0$ is the 2s orbital. The third eigenvalue solution for $n = 2, l = 1$ is the 2p orbital, and so on. Unfortunately the Schrödinger Equation is only analytically solvable for the hydrogen atom. The solutions using the KS method, luckily, are very similar. The KS kinetic energy for an atom is,

$$\tau_{ks} = \sum_{l=0}^L \sum_{n=0}^N f_{n,l} \left[|\nabla u_{n,l}(r)|^2 + \frac{l(l+1)u_{n,l}(r)^2}{r^2} \right], \quad (2.78)$$

where $f_{n,l}$ is the occupation number. By solving the KS Equation, given by Equation 2.42,

for $u_{n,l}(r)$ one can find the KS energy for any atom. This is given by

$$E_{ks} = \int \tau_{ks}(r) d^3r + E_{aux}. \quad (2.79)$$

One then minimizes the energy in a self-consistent manner as usual. The KS density in this case is

$$n(r) = \sum_{l=0}^L \sum_{n=1}^N f_{n,l} |R_{n,l}(r)|^2, \quad (2.80)$$

and the total kinetic energy is

$$T_{ks} = \int_0^\infty \tau_{ks}(r) d^3r. \quad (2.81)$$

The basic theory required to analyze the mGGArev model in the context of atoms has now been discussed. The next chapter will discuss methodology and the basic mathematical and computational expressions required to generate the mGGArev model for atoms and compare it with other kinetic energy density models in the context of atoms, especially the mGGA model.

Chapter 3

Methods

The following chapter will describe the methods used to generate atomic wave functions, how these wave functions were used to generate various kinetic energy density models, and how these methods were tested to verify the accuracy of the algorithms used. Throughout the chapter it will be illustrated why this methodology is potentially useful to compare and contrast OFDFT models.

3.1 Atomic DFT

OFDFT is designed to be used for systems with many electrons. It may seem counterintuitive that one would study atomic OFDFT. The reasons for studying these relatively simple systems are three-fold. First, because the Kohn-Sham model accurately describes the scaling behavior of atoms as nuclear charge increases, it behooves one to compare any orbital free model to the Kohn-Sham model for atoms. Second, atoms are the building blocks for molecules, chemistry, and solids. Third, elements have a periodic nature, which means that if one analyzes a row or column of the periodic table, one should expect similar behavior from the entire row or column, thus giving one the ability to fit trends in energy versus density across multiple systems. A program called FHI98PP was used to generate accurate atomic orbitals and number densities for testing various kinetic energy models [32]. What

FHI98PP generates exactly, and how the output from FHI98PP was used to generate and test kinetic energy density models is the next topic of discussion.

3.1.1 Spherical Wave Orbitals

FHI98PP was written to solve the KS Equation. In the case of atoms this is Equation 2.42. FHI98PP does this with a combination of finite difference methods and self consistent fields as discussed in section 2.3.1. Also as mentioned in section 2.6, these solutions are spherical wave functions $u_{n,l}(r)$. Once these spherical wave functions are found, FHI98PP calculates the density for each orbital using Equation 2.80, the kinetic energy density using Equation 2.78, and total ground state kinetic energy using Equation 2.81. It is at this point that it becomes necessary to describe the mesh on which the finite difference methods are done, and the associated challenges.

3.1.2 Logarithmic Grids

Because the electrostatic potential is a hyperbola and asymptotically approaches infinity as $r \rightarrow 0$, it is not trivial to model the behavior of electronic structure near the nucleus. If one were to measure the slope and the change in slope, i.e. the first and second derivatives of this potential, at various places, one would find these values to be very small far away from the nucleus. Near the nucleus however, the slope and change in slope would be quite large, and would grow exponentially as one approached the nucleus. This means that if one were to discretize the potential linearly, the error would increase exponentially moving toward the nucleus. Because of this, FHI98PP uses a logarithmic grid, which gives roughly constant error per step. This introduces some technical challenges when computing derivatives and integrals on this mesh.

The first topic discussed will be integration. The most simple expression for a finite

difference on a logarithmic grid is

$$\Delta r_i = \ln(r_{i+1}) - \ln(r_i) = \ln\left(\frac{r_{i+1}}{r_i}\right). \quad (3.1)$$

To prove this, consider the following. A logarithmic or geometric progression means that each step increases the current value by a percentage.

$$r_{i+1} = \gamma r_i + r_i \quad (3.2)$$

where γ is the percent increase. If this is the case then,

$$\ln\left(\frac{r_{i+1}}{r_i}\right) = \ln\left(\frac{\gamma r_i + r_i}{r_i}\right) = \ln(1 + \gamma) \approx \gamma, \quad (3.3)$$

in the limit of small γ , which is the correct result. It should be noted that by default FHI98PP sets $\gamma = .0247$ for all atoms, however r_0 decreases for higher Z atoms due to increased charge density near the nucleus as Z increases.

The most simple Riemann sum on this grid would be

$$\int_a^b f(r)dr \approx \sum_{i=0}^n f(r_i)\gamma \quad (3.4)$$

This sum, however, is woefully inaccurate. However if one uses the Composite Simpson's rule,

$$\int_a^b f(r)dr \approx \frac{\gamma}{3} \left[f(r_0) + 2 \sum_{i=1}^{n/2-1} f(r_{2i}) + 4 \sum_{i=1}^{n/2} f(r_{2i-1}) + f(r_n) \right], \quad (3.5)$$

the numerical results are much better. This is the numerical integration scheme that is used for all integrals throughout the remainder of this thesis.

The next topic of discussion is differentiation. The most naive approach of differentiation on a logarithmic grid is

$$\frac{df(r)}{dr} \approx \frac{f(r_{i+1}) - f(r_i)}{\Delta r}. \quad (3.6)$$

This is again quite inaccurate. However if one uses a method similar to Gauss quadrature, whereby an n -th order interpolating polynomial is fit to $n + 1$ data points about r_i , and the desired order derivative of said polynomial is taken and evaluated at r_i , the accuracy is greatly increased over the simple finite difference method. The specifics of the interpolator [33], which is dependent on the logarithmic grid, will be discussed in appendix B. For the purposes of this discussion, it should be noted that a local batch size of 6 points to each side of the reference point was used in all cases. This means that the fit polynomial was 12th order in all cases. A problem arises at the end points, because there are insufficient points on one side of the reference point to generate a centered polynomial. This requires a truncation of the data at the end points. These are the basic algorithms that are used throughout this text. The next sections will expound upon the implementation and testing of said algorithms.

3.2 What Algorithms Were Used?

3.2.1 Input

The input to the algorithms used were radial wave functions, $u_{n,l}(r_i)$, and the associated radial grid r_i . These wave functions were the output of FHI98PP. The wave functions were output orbital by orbital; first the 1s array was output, then 2s, then 2p and so on. Because the quantity that is most useful in the context of generating densities is $R_{n,l}(r)$ not $u_{n,l}(r)$, an algorithm was made to calculate $R_{n,l}(r)$ as follows

$$R_{n,l}(r_i) = \frac{u_{n,l}(r_i)}{r_i}. \quad (3.7)$$

3.2.2 Density

Next, from $R_{n,l}(r_i)$ one can calculate the number density. This is calculated using

$$n(r_i) = \frac{1}{4\pi} \sum_{n=1}^N \sum_{l=0}^L R_{n,l}(r_i)^2 f_{n,l}, \quad (3.8)$$

which is the discretized form of Equation 2.80. Recall that $f_{n,l}$ is the occupation number. For proper normalization with respect to angular momentum, a factor of $\frac{1}{4\pi}$ must be included. Because $R_{n,l}(r_i)$ and $n(r_i)$ are the required values for calculating the kinetic energy and kinetic energy densities using DFT models, the algorithms for calculating these values can now be discussed.

3.2.3 The Kohn-Sham Model

Remember τ_{ks} for atoms is given by Equation 2.78. The discretized version is essentially the same, simply replacing r with r_i . Therefore if one sums said equation over l , the resulting algorithm will be

$$\tau_{ks}(r_i) = \sum_{n=1}^N \sum_{l=0}^L \frac{f_l}{8\pi} \left[\frac{l(l+1)R_{n,l}(r_i)^2}{|r_i|^2} + |\nabla R_{n,l}(r_i)|^2 \right]. \quad (3.9)$$

It should be noted that

$$\nabla R_{n,l}(r) = \frac{dR_{n,l}(r)}{dr} \hat{\mathbf{r}} \quad (3.10)$$

was a simplifying assumption made for the calculations of kinetic energy. This is a reasonable assumption for noble gases and other atoms with high spherical symmetry. Note that $\hat{\mathbf{r}}$ is a unit vector in the \mathbf{r} direction.

3.2.4 Energy Densities

Because $n(r_i)$ has now been calculated, the kinetic energy of any OFDFT model can now be computed. The only notes of importance are that

$$\nabla n(r) = \frac{dn(r)}{dr} \hat{r}, \quad (3.11)$$

and

$$\nabla^2 n(r) = \frac{1}{r^2} \frac{d}{dr} \left[r^2 \frac{dn(r)}{dr} \right], \quad (3.12)$$

because the assumption that $n(r_i)$ is spherically symmetric was made.

3.2.5 Total Energy

The last thing that needs to be calculated is the total energy. This is an integral over a spherical volume of the kinetic energy density of a given model,

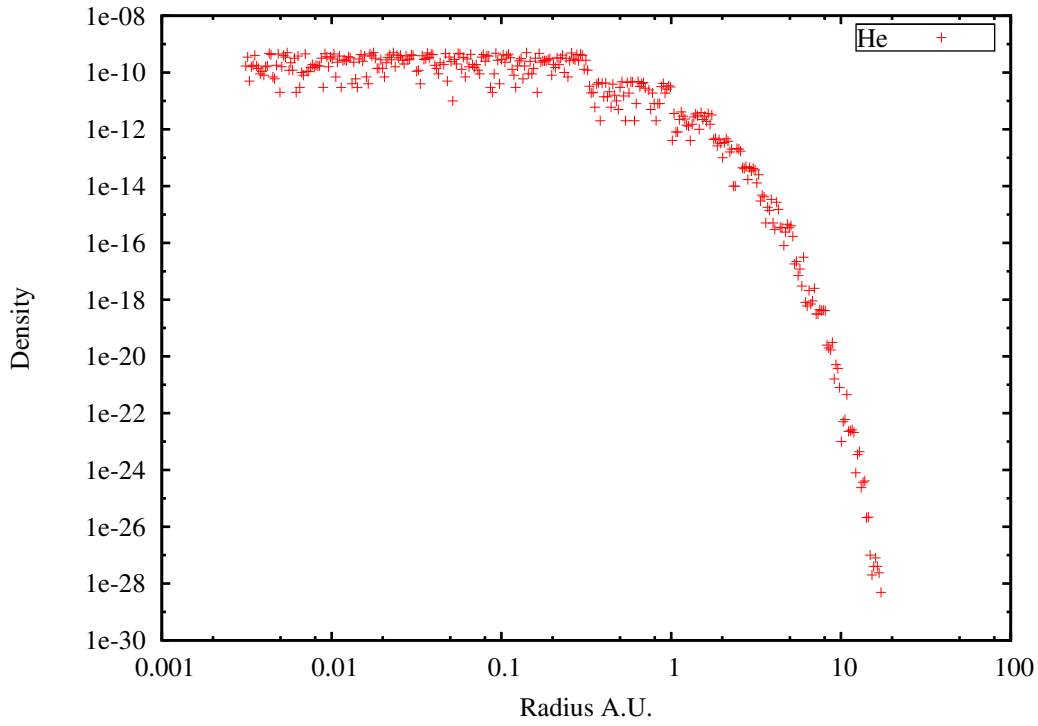
$$T = 4\pi \int_0^\infty \tau_{model}(r) |r|^2 dr, \quad (3.13)$$

using a Simpsons integral given by Equation 3.5.

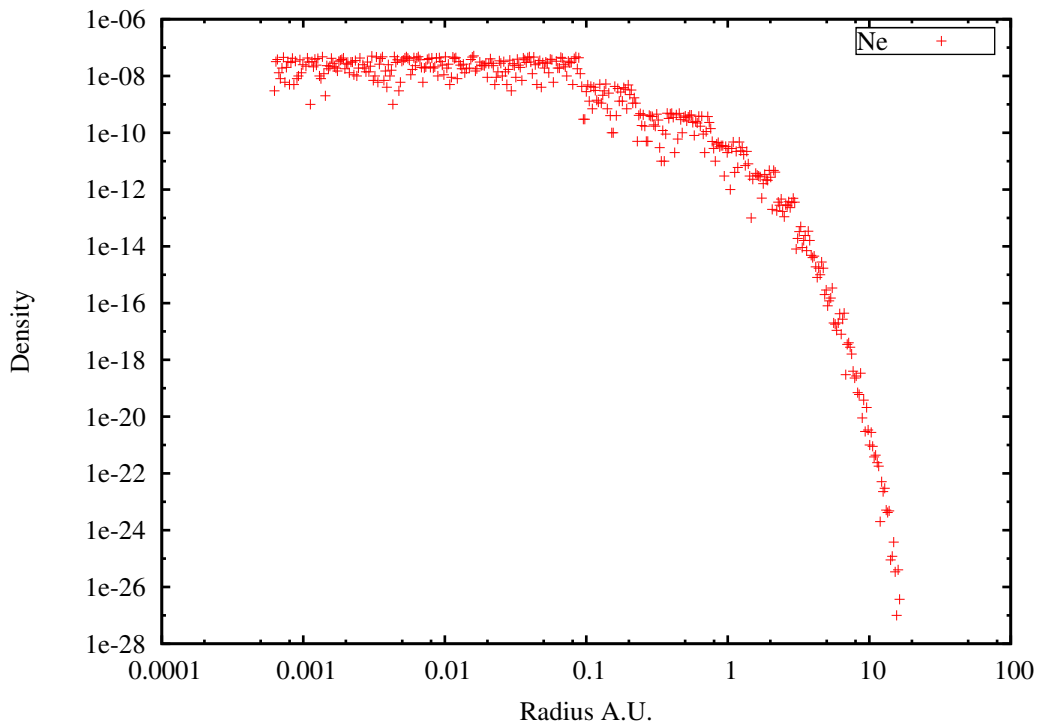
3.3 Code Tests and Verification

3.3.1 Comparing Densities to FHI98PP

All OFDFT models depend on densities. It is imperative that the computed densities be accurate, otherwise all other calculations will be for naught. FHI98PP calculates total densities once it calculates orbital wave functions. Because FHI98PP's wave functions are being used, the density algorithm described in Equation 3.8 should calculate the same density for any atom as FHI98PP. Figures 3.1(a) and 3.1(b) show the difference between densities generated by Equation 3.9 and FHI98PP's densities.



(a)



(b)

Figure 3.1: **(a)**This plot is of the absolute difference between FHI98PP's density and the calculated density for He. **(b)**This plot is of the absolute difference between FHI98PP's density and the calculated density for Ne.

3.3.2 Normalization and Electron Counting

The most simple and straightforward test for the density algorithm is a normalization test.

Essentially,

$$4\pi \int_0^\infty |R_{n,l}(r)|^2 |r|^2 dr = 1. \quad (3.14)$$

This has been tested for every atom with a result of 1. A similar, but more illuminating test is

$$4\pi \int_0^\infty n(r) |r|^2 dr = Z. \quad (3.15)$$

This is due to the fact that if one integrates the electron density of an atom over all space, one is essentially counting the number of electrons in the atom. Table 3.1 illustrates the results of this test.

atom	Z	Zcomp	Error
H	1	1.00000013441	-1.3441e-07
He	2	2.00000021709	-1.08545e-07
Li	3	3.00000024767	-8.25567e-08
Be	4	4.00000026824	-6.706e-08
B	5	5.00000027964	-5.5928e-08
C	6	6.00000028573	-4.76217e-08
N	7	7.00000029289	-4.18414e-08
O	8	8.00000029687	-3.71088e-08
F	9	9.00000030021	-3.33567e-08
Ne	10	10.0000003027	-3.027e-08
Ar	18	18.0000003227	-1.79278e-08
Kr	36	36.000000344	-9.55556e-09
Xe	54	54.0000003422	-6.33704e-09
Rn	86	86.0000003528	-4.10233e-09

Table 3.1: Table actual Z vs calculated Z and their relative error for various atoms.

3.3.3 Hydrogen Orbital Test Case

The following is a test of the differentiation and integration algorithms. The KS kinetic energy algorithm as given by equation 3.9 and Equation 3.13 requires both differentiation

and integration. Wave functions with analytically calculable energies are then selected. For example the hydrogenic wave functions. If the KS kinetic energy algorithm is correct, one should be able to use the hydrogenic wave functions as input, and the output should agree with the analytical result. Table 3.2 shows theoretical and calculated values for various hydrogenic wave functions.

Test Cases				
Orbital	Z	Theoretical Values	Algorithm Values	Error
1s	1	0.5	0.50000011	2.20000E-07
2p	1	0.125	0.12500001	7.00000E-08
3d	1	0.0555555556	0.055547351	-1.47690E-04

Table 3.2: Table of theoretical Hydrogen orbital total energies, calculated energies and relative error

3.3.4 Green's Theorem

Equation 2.49 and Equation 2.51 suggest tests of the density, differentiation, and integration algorithms. Essentially

$$4\pi \int_0^\infty [|\nabla\psi(r)|^2 - \psi(r)\nabla^2\psi(r)]|r|^2 dr = 0, \quad (3.16)$$

and

$$4\pi \int_0^\infty \nabla^2 n(r)|r|^2 dr = 0, \quad (3.17)$$

must hold for any atomic wave function. One could construct Equation 3.16 and Equation 3.17 using the aforementioned density, differentiation, and integration algorithms. If the FHI98pp atomic wave functions for various atoms were used as input, and the output were always zero, it would be reasonable to assume that the algorithms for density, integration, and differentiation were correct. Tables 3.3 and 3.4 give the results of these tests.

Atom	Z	$\int_0^\infty \nabla^2 n(r)$	T	$\nabla^2 n(r)/T$
H	1	2.08863172583e-06	0.424863381041	4.91601e-06
He	2	8.59649899629e-06	2.76738933829	3.10636e-06
Li	3	2.36748225166e-05	7.23701632994	3.27135e-06
Be	4	4.81018069075e-05	14.3087882661	3.3617e-06
B	5	8.16917900728e-05	24.160126274	3.38127e-06
C	6	0.000122828096555	37.1891597112	3.30279e-06
N	7	0.000175508883932	53.7302255544	3.26648e-06
O	8	0.000235950788612	74.1151724159	3.18357e-06
F	9	0.00030653211246	98.6742791906	3.1065e-06
Ne	10	0.00038504087108	127.736731382	3.01433e-06
Ar	18	0.00143211405013	524.967166602	2.72801e-06
Kr	36	0.00638260662935	2747.80997139	2.3228e-06
Xe	54	0.0151325900524	7225.09269533	2.09445e-06
Rn	86	0.0401198071979	21854.6610007	1.83576e-06

Table 3.3: Table of $\int_0^\infty \nabla^2 n(r)$, FHI98PP total energies, and their respective ratio.

Atom	Z	Green Diff	T	Green Diff/T
H	1	5.22248959044e-07	0.424863381041	1.22922e-06
He	2	2.14859511076e-06	2.76738933829	7.76398e-07
Li	3	5.91772496239e-06	7.23701632994	8.17702e-07
Be	4	1.20242393611e-05	14.3087882661	8.40339e-07
B	5	2.04216973916e-05	24.160126274	8.45265e-07
C	6	3.070500985e-05	37.1891597112	8.25644e-07
N	7	4.3875110013e-05	53.7302255544	8.16582e-07
O	8	5.89857505728e-05	74.1151724159	7.95866e-07
F	9	7.66309835314e-05	98.6742791906	7.76605e-07
Ne	10	9.62602005402e-05	127.736731382	7.53583e-07
Ar	18	0.000358042700449	524.967166602	6.82029e-07
Kr	36	0.00159570489129	2747.80997139	5.80719e-07
Xe	54	0.00378328496211	7225.09269533	5.23631e-07
Rn	86	0.0100305690939	21854.6610007	4.58967e-07

Table 3.4: Table of the difference between green's function terms Equation 3.16, the total kinetic energy, and their respective ratios for several atoms.

3.3.5 Comparing Total Energies to FHI98PP

The most important test of every algorithm was to compare the total KS energies calculated by FHI98PP to those calculated using KS algorithm given by Equation 3.9. Energies generated by the KS algorithm and FHI98PP’s KS energies show good agreement. This can be seen in table 3.5. The data sets used, the algorithms used to manipulate said data, and verifications of those algorithms have been discussed. The analysis and results of the comparison of the mGGArev model to other models can now be discussed.

Atom	Z	FHI98PP Values	Code Values	Relative Error
H	1	0.42486	0.424863381	–
He	2	2.76739	2.76738933829	–
N	7	53.73023	53.73022555	–
Ne	10	127.73673	127.736731382	–
Al	13	240.66176	240.6617641	–
Ar	18	524.96716	524.967166602	1.25760E-08
Fe	25	1259.55048	1259.550491	8.73327E-09
Kr	36	2747.80993	2747.80997139	1.50629E-08
Xe	54	7225.09245	7225.09269533	3.39553E-08
Rn	86	21854.65964	21854.6610007	6.22613E-08

Table 3.5: Table of Fhi98pp Total energies and our calculated total energies using the Kohn-Sham model with relative error. The dashes indicate that the first uncertain digit was less than the last significant digit in the FHI98PP output.

Chapter 4

Analysis and Results

Science at large is about simplification. Research in the field of OFDFT attempts to simplify the KS method by eliminating orbitals. In the case of this thesis, the simplification to which the author is referring is the identification and exploitation of the most simple quantities to properly describe the KS kinetic energy of atoms. This simplification may allow the development of an OFDFT model that can be compared to the KS model as well as other OFDFT models. Three steps will be taken to conduct this analysis.

The first will be to study trends in KS enhancement factors across the periodic table. Recall that enhancement factors are defined as the ratio of the kinetic energy density of a specific model to the TF kinetic energy as seen in Equation 2.63. More pertinent to the following discussion is the Pauli enhancement factor, $F_{model}^p(p, q)$, given by Equation 2.64. This enhancement factor is the difference between the enhancement factor of a given model, and the VW enhancement factor. A Pauli enhancement factor allows one to compare bosonic and fermionic, inhomogeneous and homogeneous, natures in a system. This is because the lower bound kinetic energy of any system should be the VW kinetic energy, which now equates to $F_{model}^p = 0$.

In the interest of simplification, enhancement factors in this context will be functions of the density, the gradient of the density, and the Laplacian of the density for a given

system. These quantities can be expressed in scale invariant unitless parameters, $p(\mathbf{r})$ and $q(\mathbf{r})$, as given by Equation 2.58 and Equation 2.59 respectively. It is interesting to plot $p(\mathbf{r})$ against $q(\mathbf{r})$ for various atoms, which is done in sections 4.1.1-4.1.3. All enhancement factors discussed below can be expressed as functions of $p(\mathbf{r})$ and $q(\mathbf{r})$. It is interesting then to make three dimensional plots of Pauli enhancement factors against $p(\mathbf{r})$ and $q(\mathbf{r})$ for various atoms, as is done in section 4.2. These three dimensional plots can be simplified if $p(\mathbf{r})$ and $q(\mathbf{r})$ are parameterized to a single variable $z(p, q)$, as given by Equation 2.65. These simplified two dimensional plots will be seen in sections 4.3.2 and 4.3.3.

Second, kinetic energy densities will be generated by various OFDFT models and compared to the KS energy for portions of the periodic table that exhibit a specific trend. Kinetic energy density for various models will be plotted as a function of radius in section 4.5.1. Complimentary plots will be made that show the difference between the kinetic energy density of a given model and the KS kinetic energy density. This is done because the KS kinetic energy is the model which all OFDFT models are attempting to approximate.

The final discussion will be centered around the total kinetic energy of atoms. Most physical properties of matter depend on the total energy, so for the success of a functional this is very important. The importance of the scaling of atomic total kinetic energy as nuclear charge is increased will be discussed in 4.5.2. Plots of total kinetic energy as a function of nuclear charge will then be shown and analyzed.

4.1 Visualizing Parametrizations

Throughout this chapter, the idea of plotting parametrized functions will be discussed. Specifically, the functions that will be parametrized will be $p(\mathbf{r})$, $q(\mathbf{r})$, and Pauli enhancement factors for various models. To give a specific example, if $p(\mathbf{r})$ were plotted against $q(\mathbf{r})$ the parametric plot would have a parameter \mathbf{r} . In this context \mathbf{r} is the radial distance from a nuclear point charge at the origin. This would result in a two dimensional plot where the

plot functionally depends on \mathbf{r} , but \mathbf{r} is not plotted explicitly.

There are many OFDFT models that are meant to map to the KS model [7]. If one wanted to analyze all models based on the second order correction of the GEA graphically, what would be the criterion for the analytical tools? The main analytical tool that already exists to describe DFT functionals is the enhancement factor. Virtually every OFDFT models enhancement factor can be expressed as some function of $p(\mathbf{r})$ and $q(\mathbf{r})$. Recall that $p(\mathbf{r})$ and $q(\mathbf{r})$ are both functionally dependent on $n(\mathbf{r})$ and its first and second order radial derivatives in such a way that each is scale invariant. This means that a Pauli enhancement factor is also scale invariant, so there are no normalization issues when comparing models. Note that $p(\mathbf{r})$ and $q(\mathbf{r})$ depend on the Fermi energy of the system, which is physical. Recall the relationship between the Pauli enhancement factor and the VW enhancement factor, as well as the discussion of VW enhancement factor as it relates to fermionic systems in section 2.3.2. Also recall the constraints on the KS functional described in section 2.4.2. The Pauli enhancement factor is defined in such a way that as $F_{model}^p(p, q) \rightarrow 0$ the behavior of the system is purely bosonic, which is the lower bound of energy, and should be the lower bound of the Pauli enhancement factor of any model that is equivalent to the KS model. One can reduce the parametrization to two dimensions for many analyses of models based on the second order correction of the GEA if one further parametrizes $p(\mathbf{r})$ and $q(\mathbf{r})$ to $z(p, q)$ given by Equation 2.65, which will be seen often in this chapter. This parametrization was chosen because the second order gradient expansions Pauli enhancement factor describes a line in the 2D parametrization.

To give the reader a clear picture of these parameterizations, observe Figure 4.1(a). This plot shows the density of argon with respect to radius in Atomic Units (AU) with a canonical normalization [34]. The density is generated by FHI98PP. This plot of Ar's radial density illuminates that argon has three filled shells, corresponding to the three peaks in the density. Figure 4.1(b) shows $p(\mathbf{r})$ and $q(\mathbf{r})$ vs \mathbf{r} . Each is plotted with a canonical Z normalization [34]. Each is derived from FHI98PP's number density for argon, $n(\mathbf{r})$. This plot shows two peaks

for both $p(\mathbf{r})$ and $q(\mathbf{r})$, one less peak than the number of filled shells. It should be noted that $q(\mathbf{r})$ leads $p(\mathbf{r})$. Similarly, $\sin(x)$ leads $\cos(x)$, and when they are plotted parametrically with respect to x , the resulting plot is a circle. Therefore, if one were to parametrize $p(\mathbf{r})$ and $q(\mathbf{r})$ with respect to \mathbf{r} , one might expect to see a corresponding oval shape where the radius of the oval shape would depend on the local amplitude of $p(\mathbf{r})$ and $q(\mathbf{r})$.

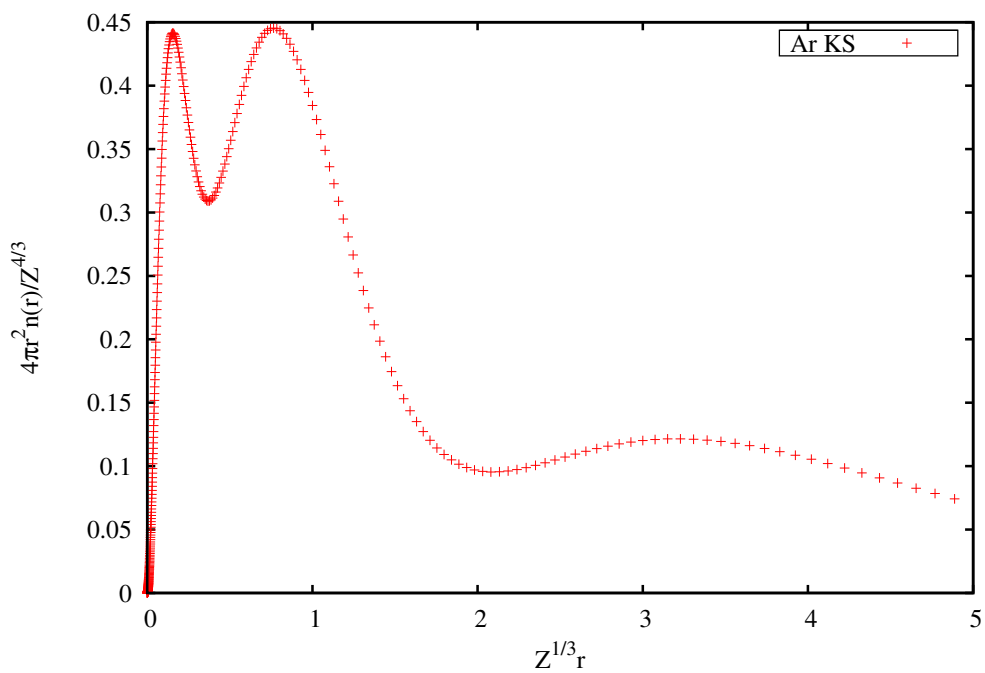
It is interesting to note that the peaks of $p(\mathbf{r})$ and $q(\mathbf{r})$ correspond to transitions between orbitals. This is physical because the density should change drastically between orbitals. It is also noteworthy that the minima of $p(\mathbf{r})$ and $q(\mathbf{r})$ correspond to the expected radii of electron shells. This is again physical because the density shouldn't vary much as the radius changes slightly from the expected radius of an electron. A paper by Bader [31] gives a good explanation of this¹.

4.1.1 The Second Row of the Periodic Table

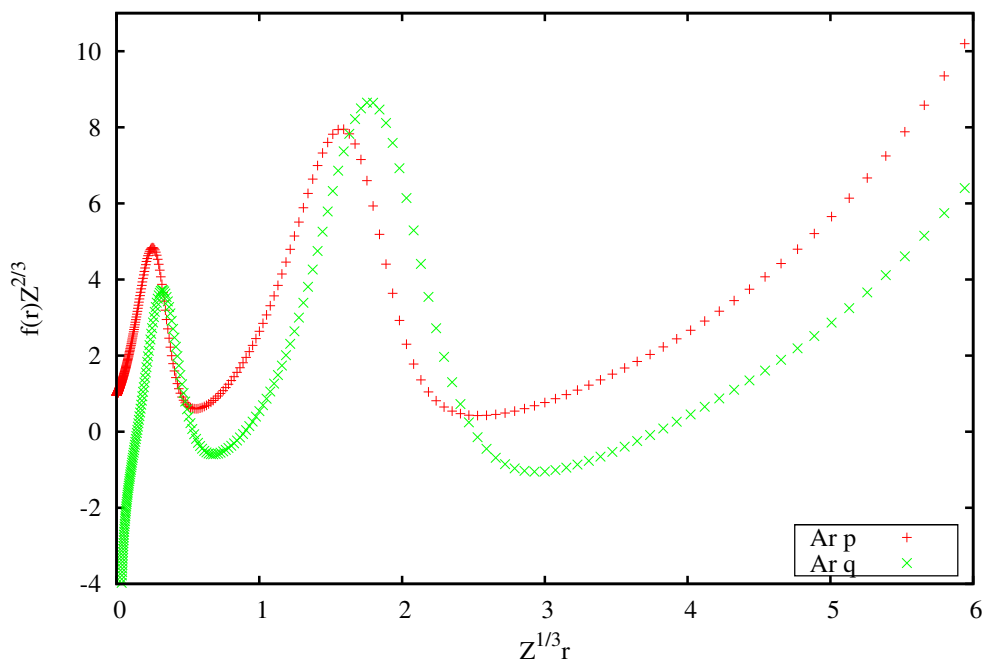
One of the motivations for specifically analyzing atoms is their periodic nature. Figure 4.2 shows a parametric plot of $p(\mathbf{r})$ vs $q(\mathbf{r})$ parametrized with respect to \mathbf{r} [35]. Each curve is derived using FHI98PP densities for the second row of the periodic table. Each atom in the second row of the periodic table has two shells at least partially filled, and the plot of each atom loops around once. Furthermore as the nuclear charge increases, the loops become more compact. These results seem to match physical intuition.

First, the oval shaped parameterization was predicted. The single loop corresponds to the single peak one would expect for $p(\mathbf{r})$ and $q(\mathbf{r})$ for these atoms. Second, the origin equates to complete homogeneity using this parameterization, because a completely homogeneous system would have no gradient or Laplacian in its density. Elements toward the right of the periodic table are more homogeneous in the core region. Figure 4.2 agrees with the trend of noble gases being more homogeneous in the core region than alkaline metals.

¹Bader's paper gives a good explanation of physical chemistry at large, and helps develop good intuition as to how number density relates to quantum mechanical behavior in an atom/molecule.



(a)



(b)

Figure 4.1: **(a)** Number density $n(r)$ given by Equation 2.43 for argon. **(b)** $p(r)$ given by Equation 2.58 and $q(r)$ given by Equation 2.59

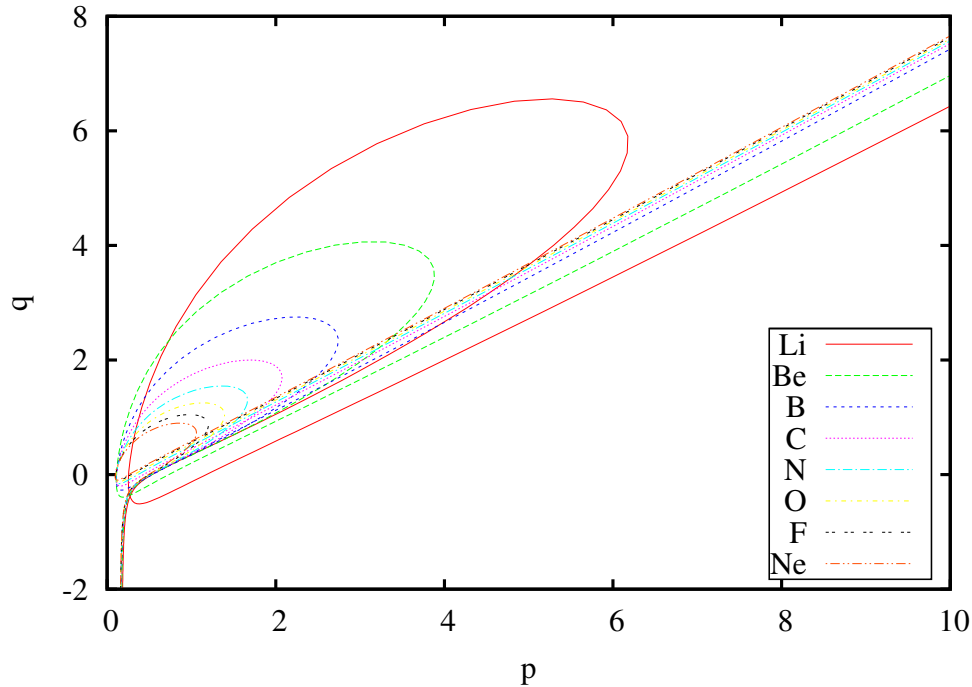


Figure 4.2: Parametric plot of $p(\mathbf{r})$ vs $q(\mathbf{r})$ for row two of the periodic table.

4.1.2 Noble Gases

The periodic table is periodic by column as well as row. Therefore, it is interesting to analyze columns as well as a rows. One of the more interesting columns for our purposes is column eight, the noble gases. They are interesting due to their completely filled shells, which means that there is no angular dependence in the core of these atoms. This allows a radial model to treat these atoms exactly. Figure 4.3(a) is a parametric plot similar to 4.2 but for helium, neon, argon, and radon. Figure 4.3(b) is a parametric plot of $p(\mathbf{r})$ vs $q(\mathbf{r})$ for krypton and xenon. The purpose of splitting the noble gases into two plots was to avoid unreadable plots. It is interesting to note that the curve for helium, which has only one filled shell, has no loops. Of course, how could it have loops when the number of loops is one less than the number of filled shells? The single peak in heliums density corresponds to the one and only turning point of $p(\mathbf{r})$ and $q(\mathbf{r})$ for helium. This is what gives it its hockey stick shape.

It is also interesting to note that as one goes down column eight, the number of loops increases by one as the row number increases. This means neon has one loop, argon has two

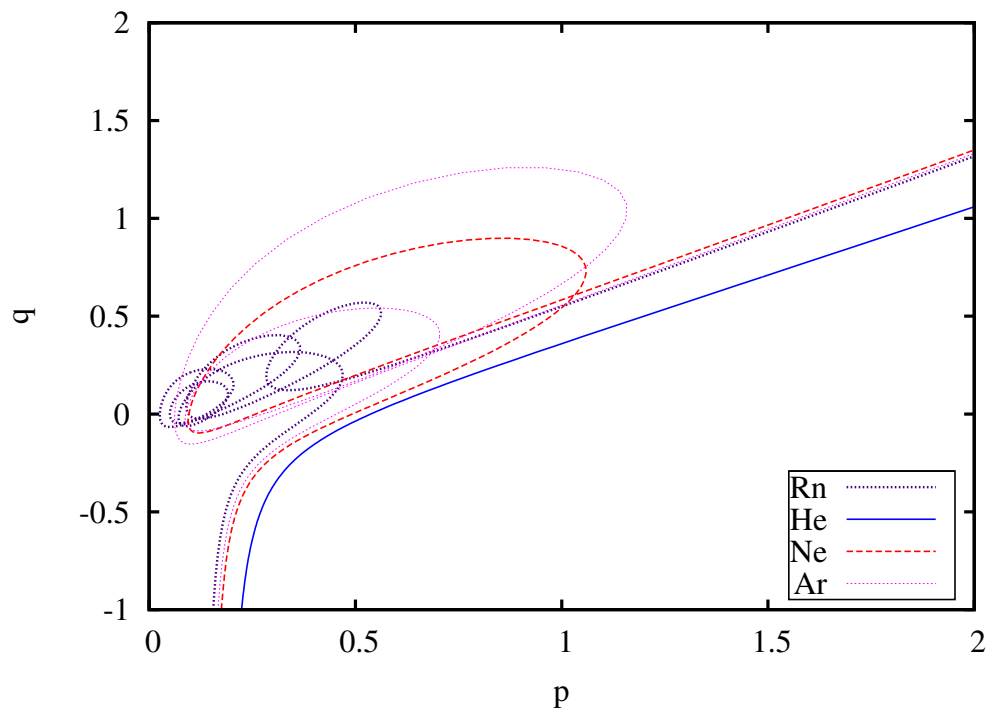
loops and so on, corresponding to one less than the number of filled shells. It also seems that the loops for the core electrons are more compact, and the loops for frontier electrons are more spread out. This is again a physical result, as one would expect the slope and inflection of frontier electrons to be large, due to their exponential decay, and the core shells to be more homogeneous.

4.1.3 Three Regimes

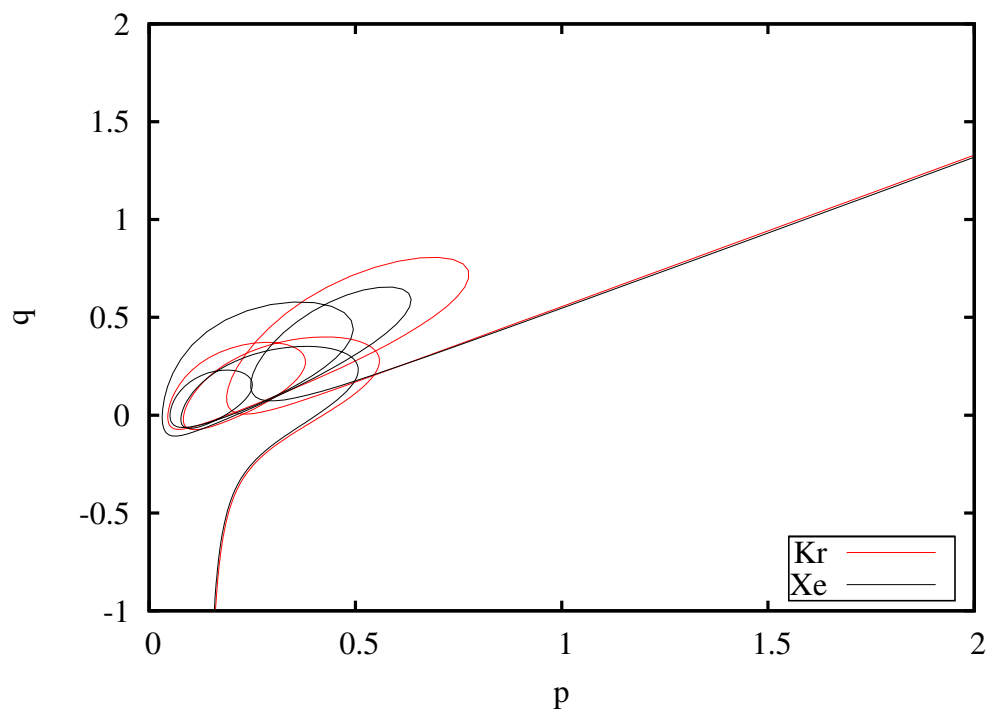
Several conclusions can be drawn from the above analysis. Figure 4.4 parametrically plots $p(\mathbf{r})$ vs $q(\mathbf{r})$ and is split into three regions of disparate behavior. Region A is the frontier region of each atom. Region B is the core region of each atom. Region C is the near-nuclear region of each atom. It can be concluded that section A is the frontier region of each atom because of the large values of $p(\mathbf{r})$ and $q(\mathbf{r})$. This is indicative of frontier electrons, which are the outermost electrons, due to their exponential decay. Exponential decay would result in exponential gradients and Laplacians. It can be concluded that region B is the core region, the region of highest electron density, due to the number of loops and their increasing compactness. This is indicative of going from the more drastically changing density of frontier shells into the core where density is more homogeneous. Finally one can conclude region C is the near-nuclear region because $p(\mathbf{r})$ is small, however $q(\mathbf{r})$ goes to $-\infty$. This suggests some sort of discontinuity at the origin, a nuclear point charge.

4.1.4 Views in 3D space

Up to now only parameterizations of $p(\mathbf{r})$ and $q(\mathbf{r})$ have been discussed. It is now prudent to include a third dimension, the KS Pauli enhancement factor as given by Equation 2.64. Figure 4.5(a) plots the KS Pauli enhancement factor vs $p(\mathbf{r})$ vs $q(\mathbf{r})$ for each of the noble gases. The KS Pauli enhancement factor uses $p(\mathbf{r})$ and $q(\mathbf{r})$ as its inputs. This results in a 3D parametric plot similar to the 2D plot 4.4. The plot view is rotated 30 degrees about the enhancement factor axis. The curves are again derived using atomic densities. Figure



(a)



(b)

Figure 4.3: (a) Parametric plot of $p(\mathbf{r})$ vs $q(\mathbf{r})$ for helium, neon, argon, and radon. (b) Parametric plot of $p(\mathbf{r})$ vs $q(\mathbf{r})$ for krypton and xenon.

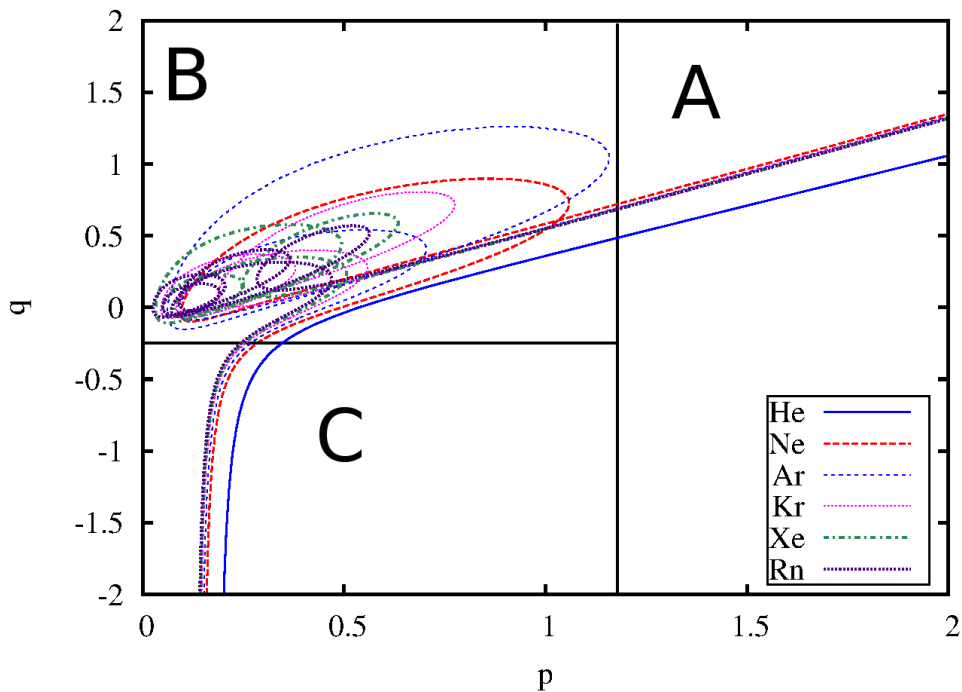


Figure 4.4: Parametric plot of $p(\mathbf{r})$ vs $q(\mathbf{r})$ for all atoms in column eight of the periodic table.

4.5(b) is virtually the same as 4.5(a), but the plot view is rotated 60 degrees about the enhancement factor axis. Figures 4.6(a), and 4.6(b) are plots similar to Figure 4.5(a) with plot views further rotated about the enhancement factor axis to 90 degrees and 120 degrees respectively. Figure 4.6(b) is especially interesting. It can be seen that the frontier and core regions are coplanar, so if one were to look at that plane edge on, the whole curve would look like a hockey stick. Note that this is a different hockey stick from the helium hockey stick mentioned earlier. A successful mapping of an OFDFT to the KS kinetic energy should predict this hockey stick behavior. A hockey stick has only one turning point, which was conjectured by Equation 2.72!

4.2 Gradient Expansion Fits

One of the reasons the Pauli enhancement factor vs $p(\mathbf{r})$ vs $q(\mathbf{r})$ parameterization was chosen is that the second order gradient expansion Pauli enhancement factor, $F_{GEA2}^p(p, q)$, describes a plane when plotted against $p(\mathbf{r})$ vs $q(\mathbf{r})$. Recall that $\tau_{GEA2}(p, q)$ is given by Equation 2.60.

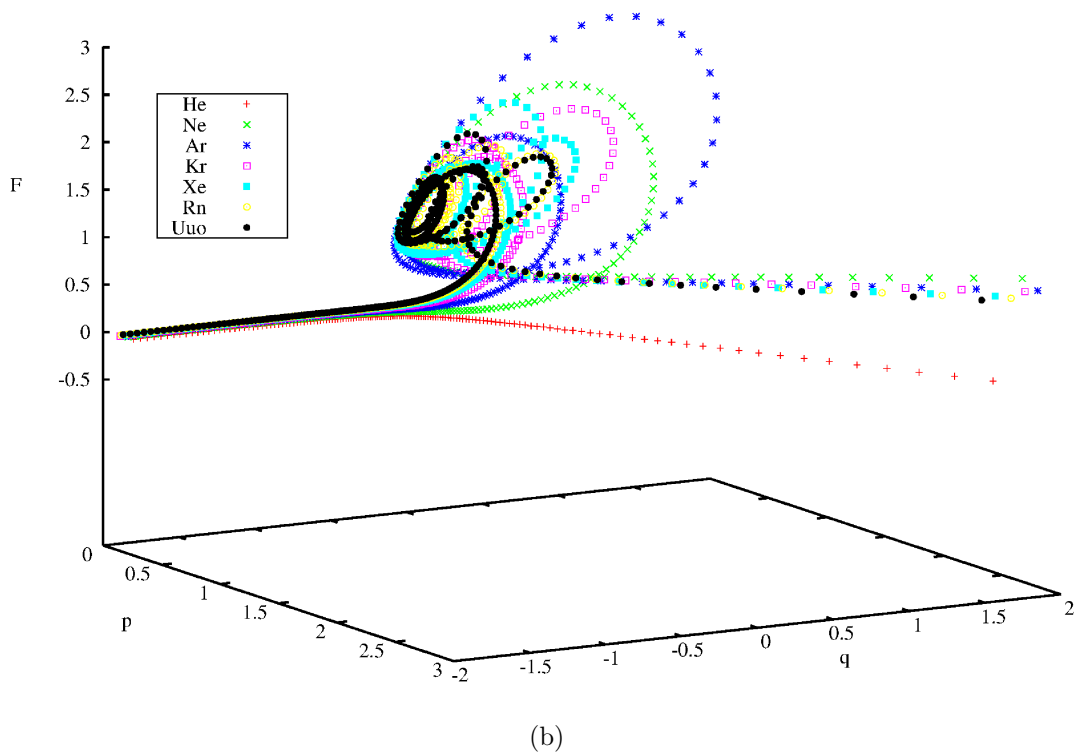
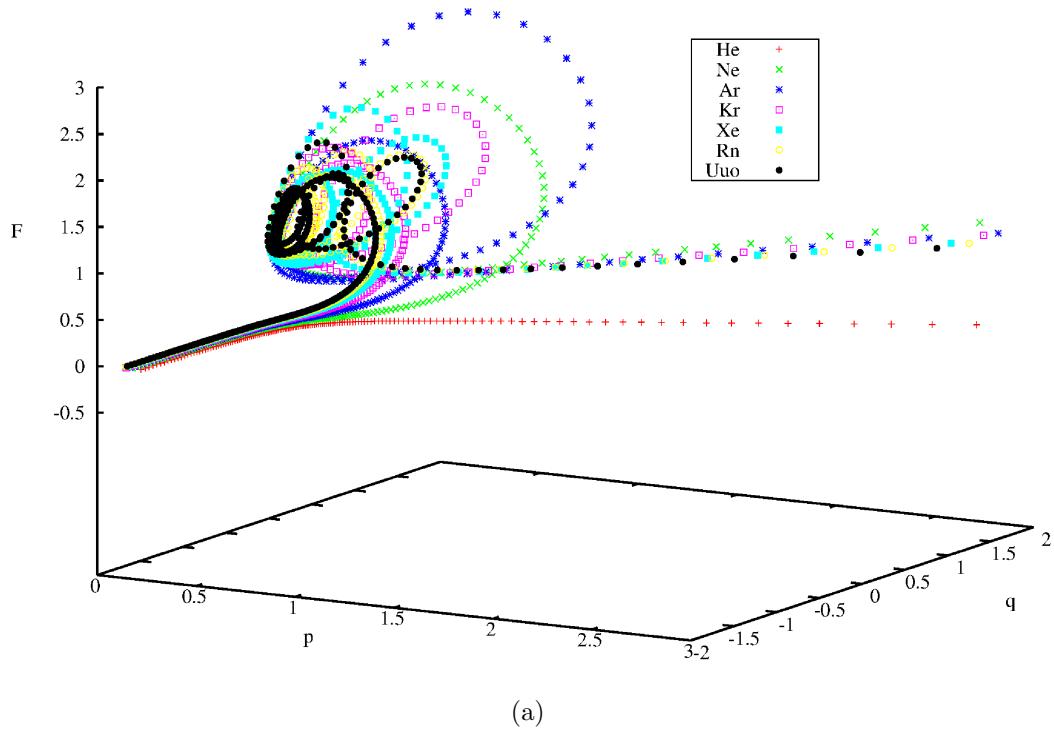
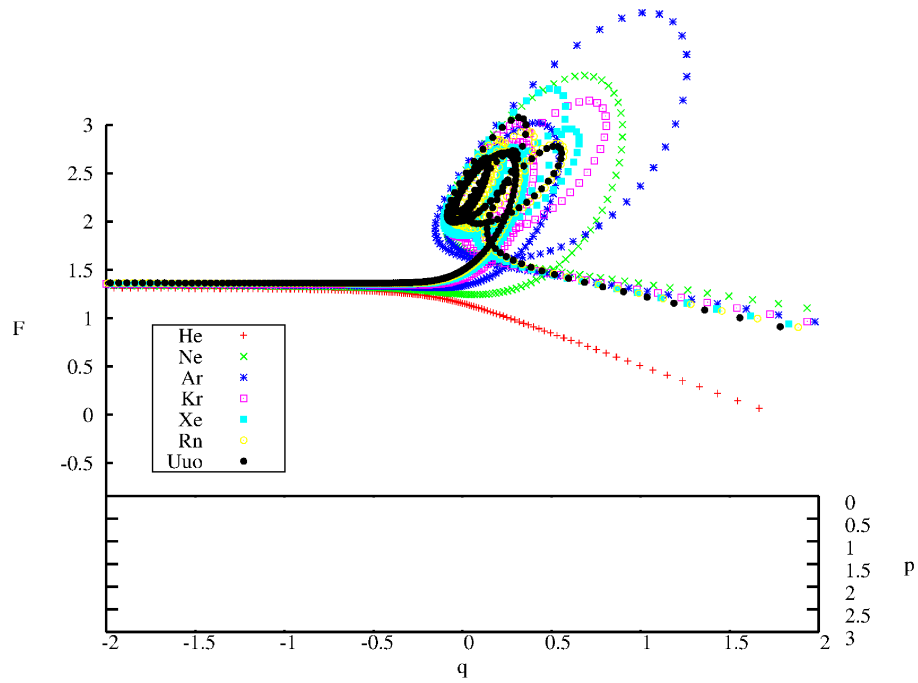
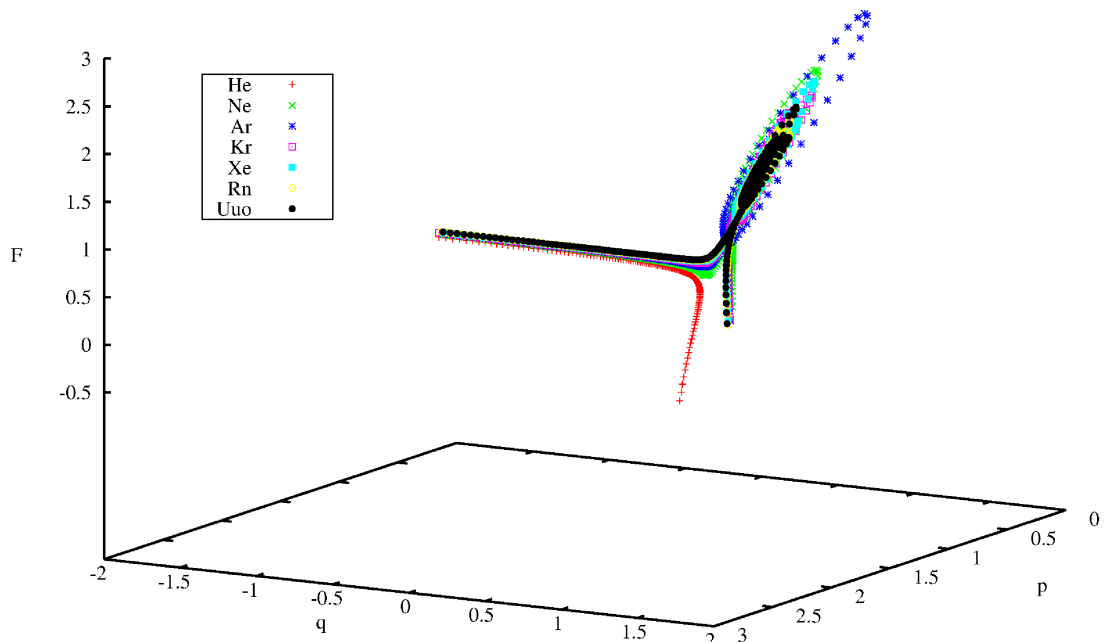


Figure 4.5: **(a)** $F_{ks}^p(p, q)$ vs $p(\mathbf{r})$ vs $q(\mathbf{r})$ for noble gases rotated 30 degrees about the F axis. **(b)** $F_{ks}^p(p, q)$ vs $p(\mathbf{r})$ vs $q(\mathbf{r})$ for noble gases rotated 60 degrees about the F axis.



(a)



(b)

Figure 4.6: **(a)** $F_{ks}^p(p, q)$ vs $p(\mathbf{r})$ vs $q(\mathbf{r})$ for noble gases rotated 90 degrees about the F axis. **(b)** $F_{ks}^p(p, q)$ vs $p(\mathbf{r})$ vs $q(\mathbf{r})$ for noble gases rotated 120 degrees about the F axis.

This may correlate to the coplanar core and frontier regions of the KS Pauli enhancement factor. It would be ideal then, if the plane described by $F_{GEA2}^p(p, q)$ were the same plane that the core and frontier regions of the KS Pauli enhancement factor fall on.

Figure 4.7(a) plots $F_{ks}^p(p, q)$ and $F_{GEA2}^p(p, q)$ vs $p(\mathbf{r})$ vs $q(\mathbf{r})$. The plot view is rotated about the $p(\mathbf{r})$ axis such that the plane described by $F_{GEA2}^p(p, q)$ viewed from the $q = 0$ direction is seen edge on. Figure 4.7(b) also plots $F_{ks}^p(p, q)$ and $F_{GEA2}^p(p, q)$ vs $p(\mathbf{r})$ vs $q(\mathbf{r})$, however the plot view is rotated about the $q(\mathbf{r})$ axis such that the plane described by $F_{GEA2}^p(p, q)$ viewed from the $p = 0$ direction is seen edge on. From these plots it can be seen that the plane described by the core and frontier regions of the KS enhancement factor and the plane described by gradient expansions enhancement factor don't quite overlap.

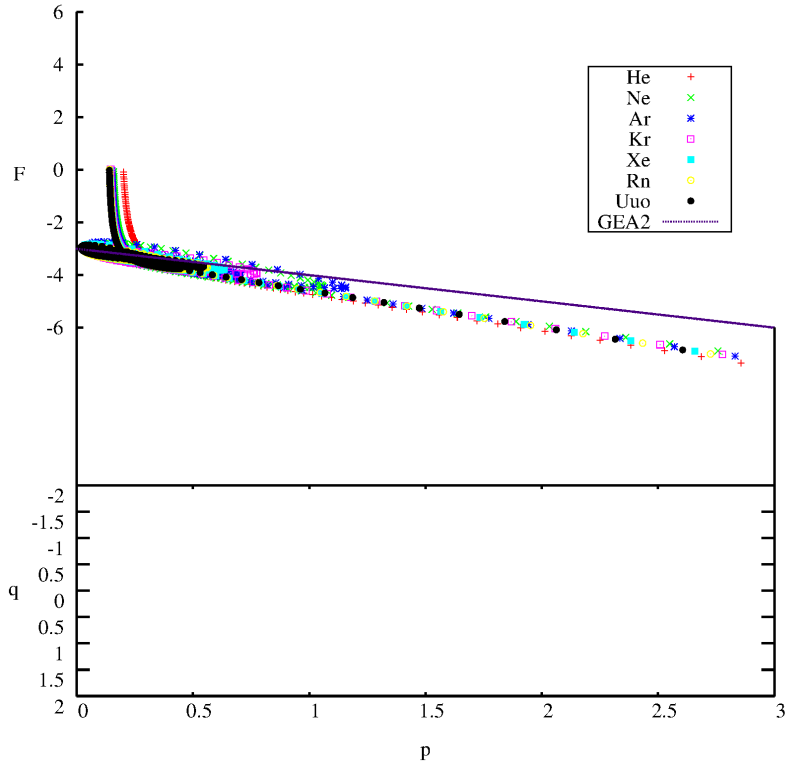
One can empirically construct an expansion similar to $F_{GEA2}^p(p, q)$ that describes the exact plane the core region and frontier regions of the KS enhancement factor fall on. Utilizing Gnuplots [36] least squares fit in the regions $0 < p < 0.75$ and $-0.125 < q < 0.75$, such an expansion was constructed. The fit regions were chosen to correspond to the core of the average atom, which is the most homogeneous portion. The following equation,

$$z_{emp} = a \cdot \sin(\theta)p + a \cdot \cos(\theta)q, \quad (4.1)$$

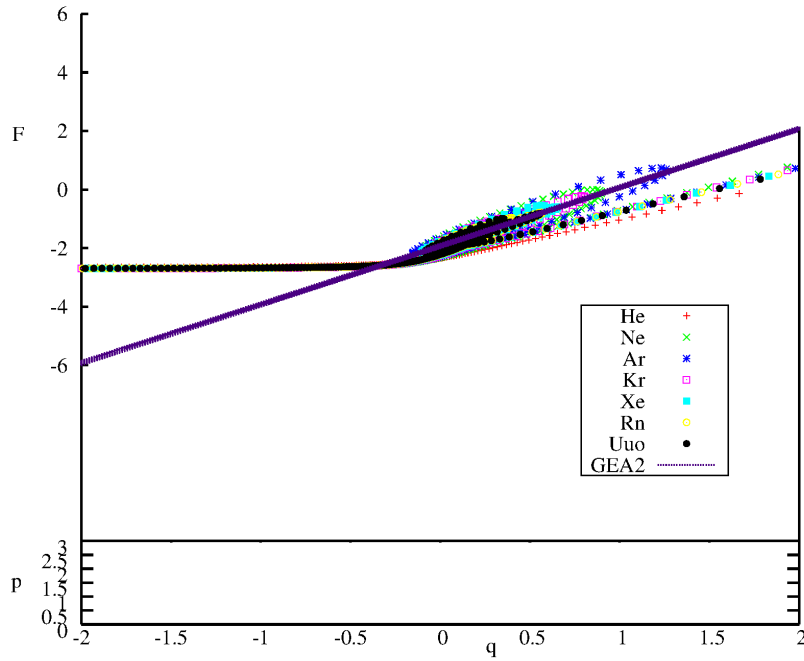
was the fitting variable for all empirically fit gradient expansions. The adjustable parameters in the equation were a and θ . The function,

$$F_{GEA2}(z_{emp}) = 1 + z_{emp}, \quad (4.2)$$

was then fit to KS enhancement factors in order to generate an empirical $F_{GEA2}^p(p, q)$ comparable to Equation 2.60. This function was most notably fit to the KS enhancement factors of the noble gases and the alkali earth metals. The resulting fit parameter values were $a = 3.50931 \pm 0.01694$ and $\theta = -0.59517 \pm 0.001723$ for the $F_{GEA2}^p(p, q)$ empirically fit to the noble gases, and $a = 3.38617 \pm 0.0232$ and $\theta = -0.57671 \pm 0.002596$ for the $F_{GEA2}^p(p, q)$



(a)



(b)

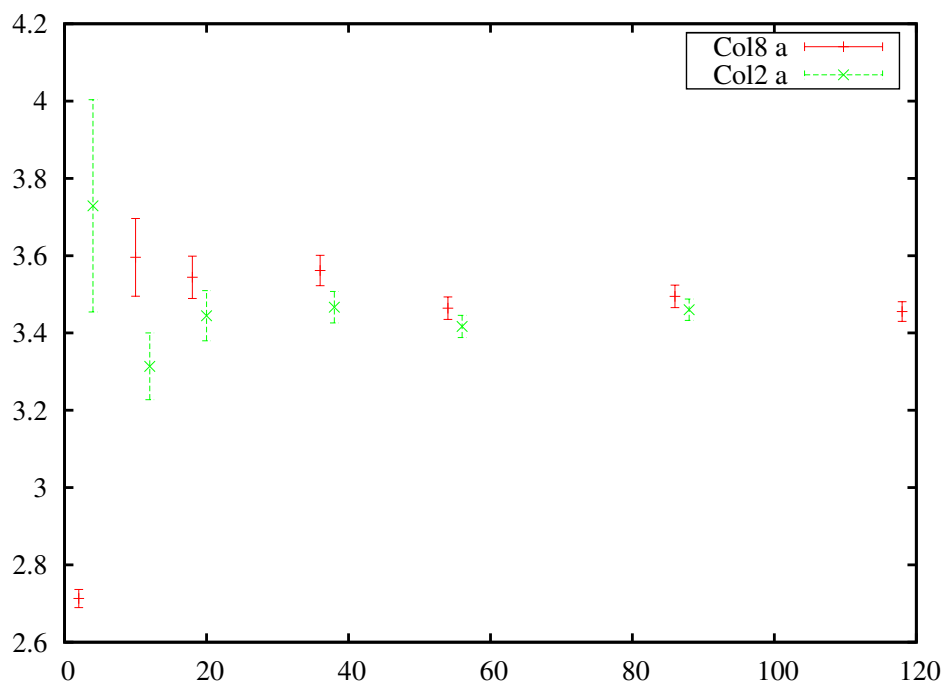
Figure 4.7: **(a)** $F_{ks}^p(p, q)$ and $F_{GEA2}^p(p, q)$ vs $p(\mathbf{r})$ vs $q(\mathbf{r})$ rotated such that the plane described by $F_{GEA2}^p(p, q)$ viewed in the $q = 0$ direction is seen edge on. **(b)** $F_{ks}^p(p, q)$ and $F_{GEA2}^p(p, q)$ vs $p(\mathbf{r})$ vs $q(\mathbf{r})$ rotated such that the plane described by $F_{GEA2}^p(p, q)$ viewed in the $p = 0$ direction is seen edge on.

empirically fit to the alkaline earth metals. The fit to the noble gases excluded hydrogen as an outlier.

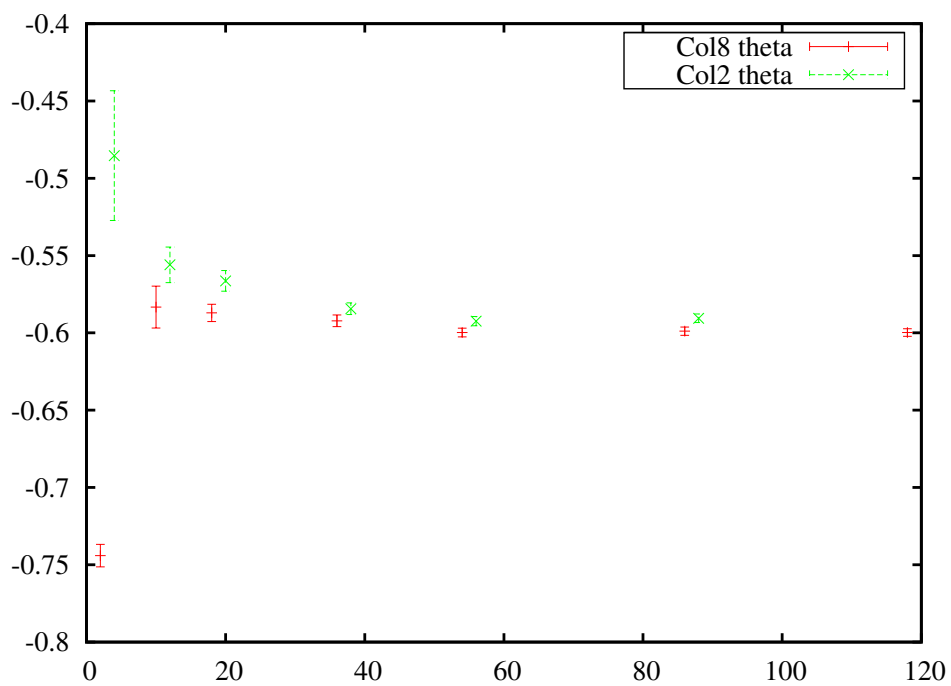
To ensure the fits were reasonable, and to determine if there was any systematic trend down the respective columns of the periodic table for the fit parameters, individual atoms in both the alkaline earth metals and the noble gases were also fit in the same manner. Figure 4.8(a) shows the values for the parameter a as a function of Z . The red data points correspond to parameter values for atoms from the noble gases, and the green data points correspond to parameter values for atoms from the alkaline earth metals. The error presented was the error given by Gnuplot's [36] linear regression algorithm. Figure 4.8(b) shows the values for the parameter θ as a function of Z . Again the red data points correspond to noble gases, the green data points correspond to atoms from the alkaline earth metals and the error presented was the error given by Gnuplot's linear regression algorithm.

It seems from these Figures there is in fact a trend. These plots show that the error for each parameter is less for larger Z atoms, and also that each of the fit parameters for the alkaline earth metals and the noble gases converge on a single shared value. It is interesting to note that if one averages the values of a for the noble gases in Figure 4.8(a) (excluding helium), the average value, $a = 3.519$, is very close to the value found when fitting all noble gases excluding helium, $a = 3.50931$. The average of the values of a for the alkaline earth metals in Figure 4.8(a), $a = 3.472$, does not agree with the value found from fitting all alkaline earth atoms, $a = 3.38617$. A stress test was employed to determine why this is. The upper limit of the fit range for $p(\mathbf{r})$ and $q(\mathbf{r})$ was varied when fitting these individual atoms. When the upper limit of the fit range was reduced, the resulting values of a for large Z atoms changed little. The varying upper limit had a large impact in the values of a for small Z atoms. This suggests that the fitting criteria used is more stable for large Z atoms.

With this knowledge, an empirically fit $F_{GEA2}^p(p, q)$ was fit to KS enhancement factor data for xenon, barium, radon, radium, and ununocium. It should be noted that ununocium is element 118, a noble gas. The fit range was slightly modified for these atoms to $0 < p < 0.6$



(a)



(b)

Figure 4.8: **(a)** Fit parameter $a(Z)$ vs Z as determined by fitting Equation 4.2 to $F_{ks}^p(p, q)$ of individual atoms. **(b)** Fit parameter $\theta(Z)$ vs Z as determined by fitting Equation 4.2 to $F_{ks}^p(p, q)$ of individual atoms.

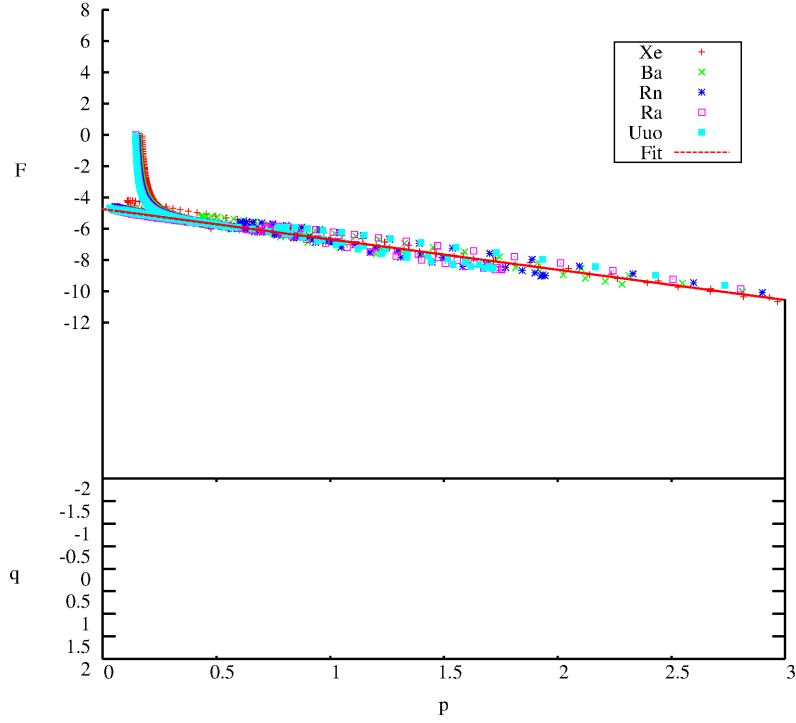
and $-0.125 < q < 0.6$, because the core region of higher Z atoms are more homogeneous. The fit parameters were $a = 3.45905 \pm 0.0127$ and $\theta = -0.594433 \pm 0.001286$. These values are quite close to the parameters for the $F_{GEA2}^p(p, q)$ empirically fit to the noble gases.

Figure 4.9(a) plots $F_{ks}^p(p, q)$ vs $p(\mathbf{r})$ vs $q(\mathbf{r})$ and an $F_{GEA2}^p(p, q)$ vs $p(\mathbf{r})$ vs $q(\mathbf{r})$ empirically fit to large Z atoms. The plot view is rotated about the $p(\mathbf{r})$ axis such that the empirically fit $F_{GEA2}^p(p, q = 0)$ plane is seen edge on. Figure 4.9(b) also plots $F_{ks}^p(p, q)$ vs $p(\mathbf{r})$ vs $q(\mathbf{r})$ and $F_{GEA2}^p(p, q)$ vs $p(\mathbf{r})$ vs $q(\mathbf{r})$ empirically fit to large Z atoms. This plot view, however, is rotated about the $q(\mathbf{r})$ axis such that the empirically fit $F_{GEA2}^p(p = 0, q)$ plane is seen edge on. Visually the empirically fit $F_{GEA2}^p(p, q)$ plane seems to fit the plane described by the core and frontier regions of $F_{ks}^p(p, q)$ quite well.

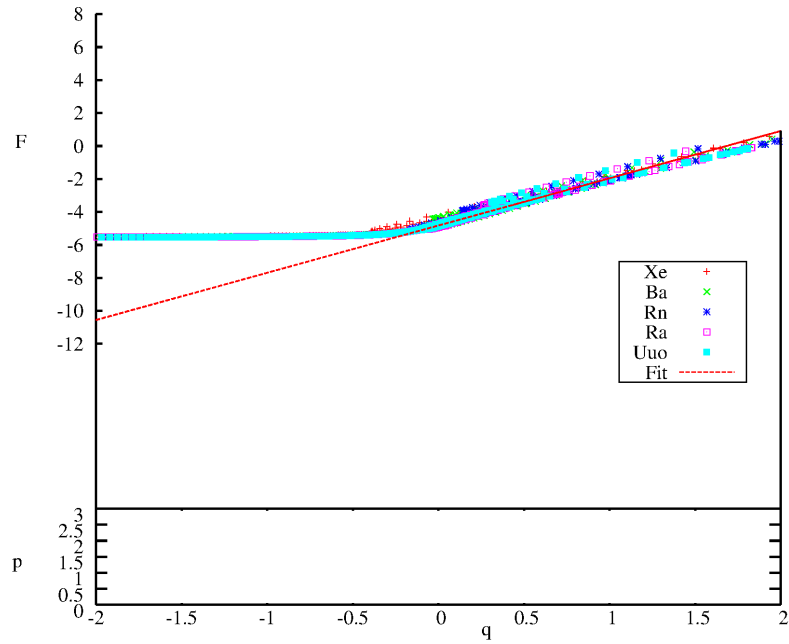
At this point it has been visually determined that the empirically fit $F_{GEA2}^p(p, q)$ fit to large Z atoms fits KS enhancement factors better than the canonical $F_{GEA2}^p(p, q)$ in the core region. Because the data being fit is $F_{ks}^p(p, q)$, the KS enhancement factor is actually the mean of the fit curve. Consequently, $|F_{ks}^p(p, q) - F_{GEA2_{model}}^p(z_{model})|^2$ is in fact the square of the standard deviation away from the mean of the fit.

Figure 4.10 shows this relationship for both the canonical $F_{GEA2}^p(p, q)$ and the $F_{GEA2}^p(p, q)$ empirically fit to large Z atoms. Both the error of the canonical $F_{GEA2}^p(p, q)$ and the $F_{GEA2}^p(p, q)$ empirically fit to large Z atoms are plotted as a function of $q(\mathbf{r})$ in the fit range -0.125 to 0.6 . It should also be noted that points of the canonical $F_{GEA2}^p(p, q)$ and the $F_{GEA2}^p(p, q)$ empirically fit to large Z atoms with $p(\mathbf{r})$ values outside the range 0 to 0.6 were excluded.

This plot shows that the $F_{GEA2}^p(p, q)$ empirically fit to large Z atoms has reduced error over the canonical $F_{GEA2}^p(p, q)$ in the core region. The idea of an empirically fit $F_{GEA2}^p(p, q)$ will be discussed later in the chapter. It should be mentioned that for the remainder of the thesis the $F_{GEA2}^p(p, q)$ empirically fit to large Z atoms will be referred to because of its agreement to KS enhancement factors, and the $F_{GEA2}^p(p, q)$ empirically fit to the alkaline earth metals will be referred to because it has the sharpest contrast with the $F_{GEA2}^p(p, q)$



(a)



(b)

Figure 4.9: **(a)** $F_{ks}^p(p, q)$ and an $F_{GEA2}^p(p, q)$ empirically fit to large Z atoms vs $p(\mathbf{r})$ vs $q(\mathbf{r})$, rotated such that the plane described by the empirically fit $F_{GEA2}^p(p, q)$ viewed from the $q = 0$ direction is seen edge on. **(b)** $F_{ks}^p(p, q)$ and an $F_{GEA2}^p(p, q)$ empirically fit to large Z atoms vs $p(\mathbf{r})$ vs $q(\mathbf{r})$, rotated such that the plane described by the empirically fit $F_{GEA2}^p(p, q)$ viewed in the $p = 0$ direction is seen edge on.

empirically fit to large Z atoms.

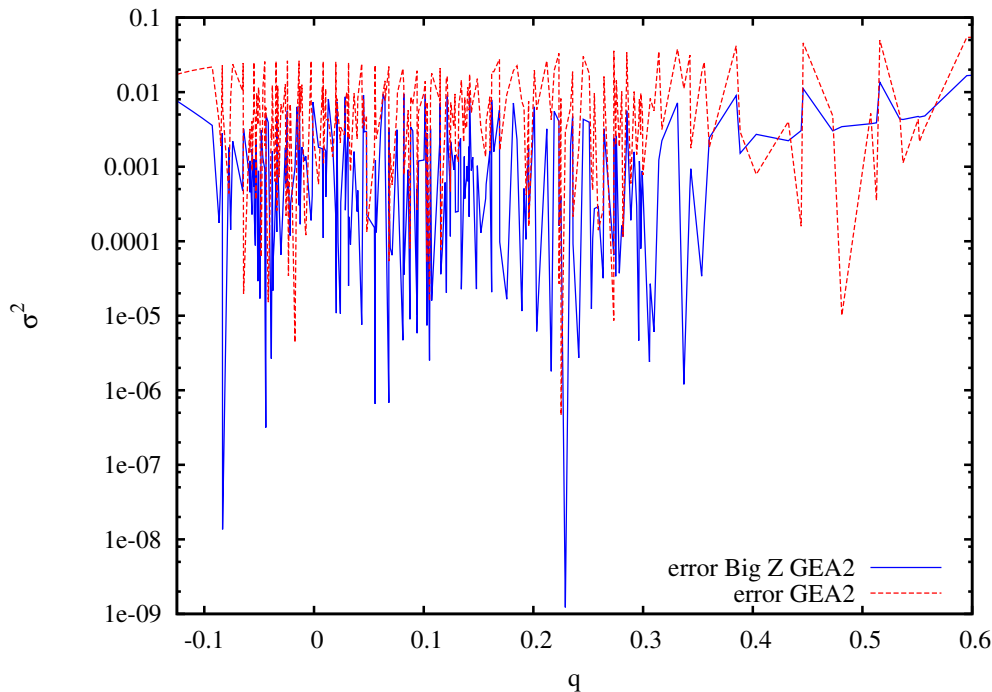


Figure 4.10: Square of the standard deviation away from $F_{ks}^p(p, q)$ of the canonical $F_{GEA2}^p(p, q)$ and the $F_{GEA2}^p(p, q)$ empirically fit to large Z atoms in the core region of $F_{ks}^p(p, q)$.

4.3 Stitching Between the GEA2 and VW

A functional which closely fits the core region and frontier region of KS enhancement factors for many atoms has been constructed. The near-nuclear region has yet to be addressed. In the near-nuclear region all electrons are on the same energy level. This is because only two electrons are being sampled in this region regardless of Z due to small radius. This would likely lead one to come to the conclusion that the density would approach the behavior of the VW functional. This would suggest limits such that as $z \rightarrow -\infty$, $F_{model}^p(z) \rightarrow 0$ in the $F_{model}^p(z)$ vs z parameterization. Because gradient expansions do not go to the VW limit, a model is required that stitches these two limiting behaviors together.

4.3.1 Perdew and Constantin

The first attempt at stitching a gradient expansion to F_{vw} was done by Perdew and Constantin [12]. Their model is given by Equations 2.69 and 2.70. This was a good first step at stitching together these two limits, and offers reasonable total kinetic energy values. There are some characteristics which are lacking [1], which was the motivation to generate a more suitable stitching function. The shortcomings and triumphs of the mGGA model will be discussed in detail throughout the rest of the chapter, to contrast the mGGArev model.

4.3.2 The mGGArev Model: Canonical GEA2

The model given by Equation 2.72 was slightly altered with a transitional tuning parameter, α . This was done because it was necessary to control how fast the functional approached the VW limit as $z \rightarrow -\infty$. This altered stitching function is given by

$$F_{mGGArev} = 1 + F_{vw} + z[1 - \Theta(-z)e^{-1/|z|^\alpha}]^{1/\alpha}. \quad (4.3)$$

It is prudent to now analyze the limit of this new functional as $z \rightarrow -\infty$. Let $u = \frac{1}{|z|^\alpha}$. As $z \rightarrow -\infty$ Equation 4.3 becomes

$$\begin{aligned} F_{mGGArev} &= 1 + F_{vw} + z[1 - e^{-u}]^{1/\alpha} \approx \\ &1 + F_{vw} + z[1 - (1 - u)]^{1/\alpha} = 1 + F_{vw} + \frac{z}{|z|} = F_{vw}. \end{aligned} \quad (4.4)$$

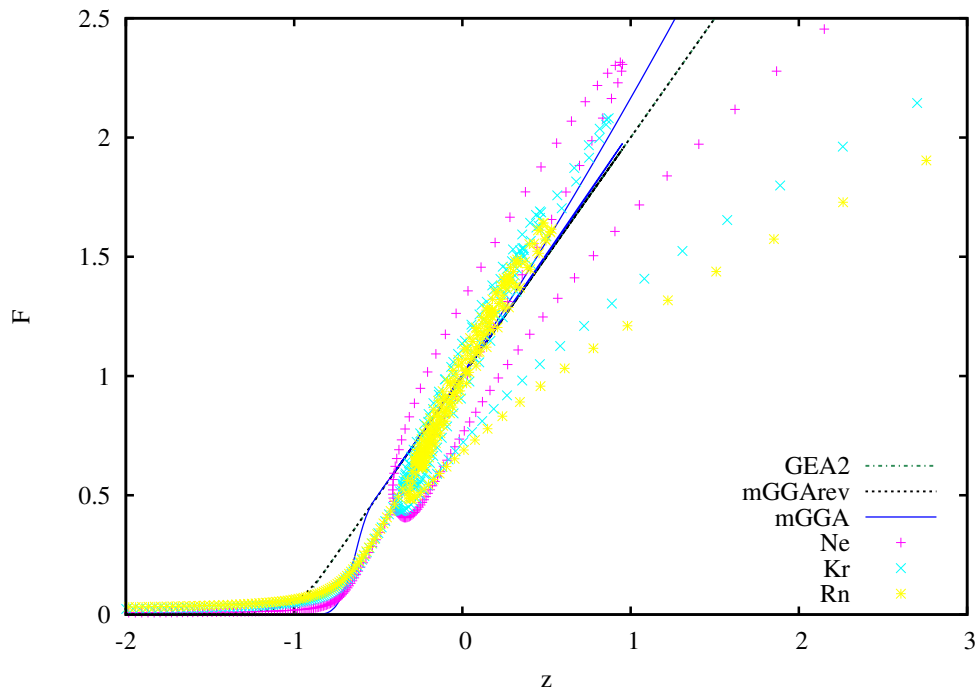
This confirms that the $z \rightarrow -\infty$ limit is unchanged from Equation 2.75. In the case where $z \rightarrow 0$ Equation 4.3 goes to $1 + F_{vw} + z$ which is unchanged from Equation 2.74.

It should be noted that a number of values of α were experimented with. The general trend was as follows. For small α , the stitching function approached the VW limit too slowly as $z \rightarrow -\infty$, which caused overestimation in kinetic energy. As α became larger, $\alpha \approx 10$, the kinetic energy was closer to the KS kinetic energy, but the stitching feature was sharp, which

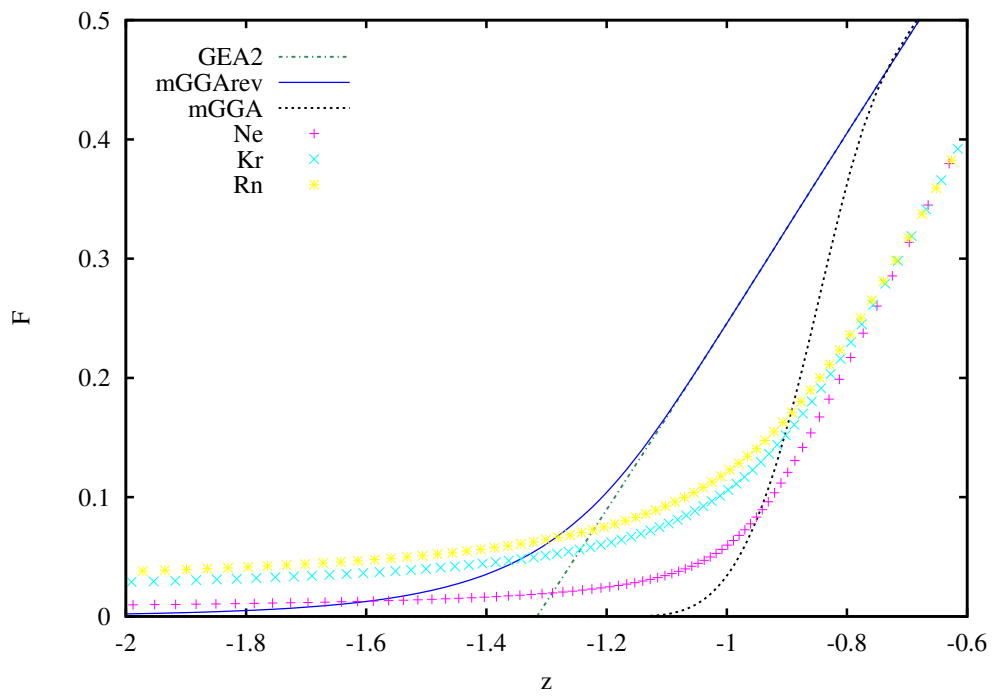
would cause computational problems when the kinetic energy was minimized. A potential value of α that split the difference between these two features was $\alpha = 4$, which is the value of α used throughout the remainder of the thesis unless otherwise specified.

It is prudent now to compare several pertinent models to $F_{mGGA_{rev}}$ graphically, and this will be done in Figure 4.11(a) and Figure 4.11(b). First, the KS Pauli enhancement factor is plotted for a number of atomic electron densities because it is the functional that each OFDFT model is attempting to approximate. These will be called Ne, Kr, and Rn respectively. Second, because each of the models with stitching functions should stitch between the VW limit and the Pauli enhancement factor for the second order gradient expansion, the second order gradient expansion, $F_{GEA2}^p(z)$, is plotted. This will be referred to as GEA2 in the following Figures. Recall the VW limit is the horizontal axis by definition. Third, the current state of the art model, $F_{mGGA}^p(p, q)$, is plotted. This will be referred to as mGGA in the following Figures. The final curve is the model being developed in this thesis, $F_{mGGA_{rev}}^p(z)$. This will be referred to as mGGArev. This convention should allow one to compare the mGGA and mGGArev models, their stitching characteristics, and their agreement with the KS model in terms of enhancement factors.

Figure 4.11(a) illustrates that the mGGArev curve and the KS curves Ne, Kr, and Rn have a single turning point as conjectured by Equation 2.72! The mGGA curve does not. Figure 4.11(b) is a re-plot of Figure 4.11(a) rescaled to focus on the near-nuclear region, $-2 < z < -0.6$. Note the poor fit to of the KS curves Ne, Kr, and Rn by the mGGArev curve when compared to the mGGA curve in both Figure 4.11(a) and Figure 4.11(a). The mGGA curve does seem to fit the KS curves better than the mGGArev curve, especially in the hockey stick transition to the near-nuclear regime. However the insights of empirically fit gradient expansions have yet to be considered!



(a)



(b)

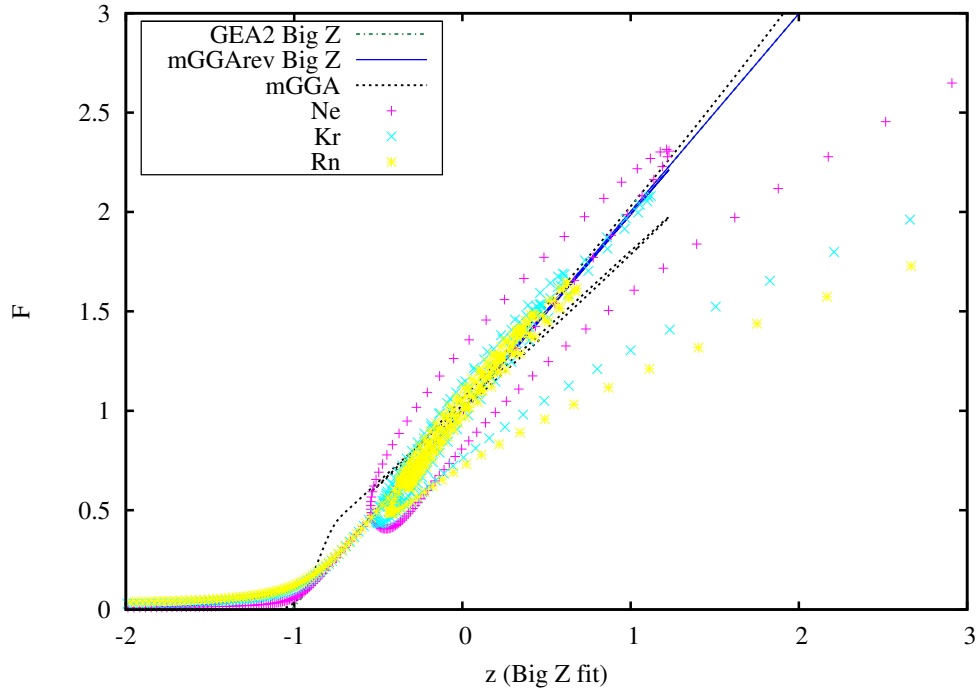
Figure 4.11: **(a)** $F_{mGGA_{rev}}^p(z)$, $F_{mGGA}^p(p, q)$, $F_{ks}^p(\mathbf{r})$, and $F_{GEA2}^p(z)$ vs z . **(b)** Re-plot of Figure 4.11(a) zoomed in on the near-nuclear region.

4.3.3 The mGGAreV Model: Empirically Fit GEA2

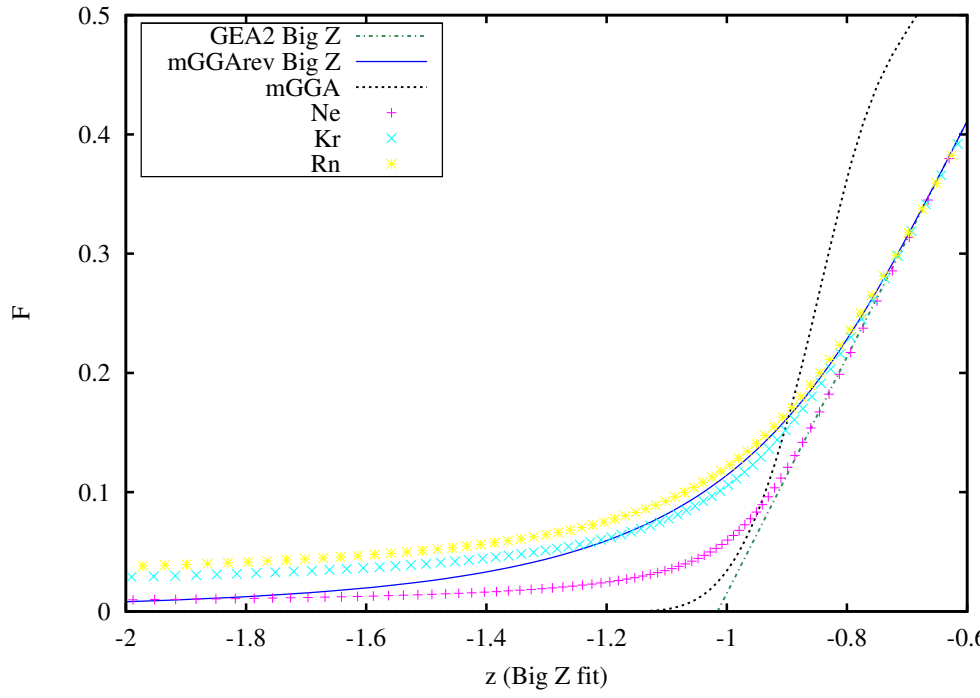
Using the insights gained from considering empirically fit gradient expansions, the mGGAreV model can be adapted from depending on the canonical z to an empirically fit z . The following Figures will be similar to Figure 4.11(a) and Figure 4.11(b). The key difference is that the mGGAreV models will be stitching the VW limit to an empirically fit gradient expansion. The empirically fit gradient expansion, $F_{GEA2}^p(z_{emp})$, fit to large Z atoms will be referred to as GEA2 Big Z . Recall that the gradient expansion fit to large Z atoms was the most similar to KS enhancement factors in the core region. The mGGAreV model that stitches the GEA2 Big Z to the VW limit, $F_{mGGAreV}^p(z_{emp})$, will be referred to as mGGAreV Big Z . The remaining curves follow the same naming convention already outlined.

Observing Figure 4.12(a), it can be seen that the GEA2 Big Z curve and the mGGAreV Big Z curve, each visually correspond to the KS curves, Ne, Kr, and Rn, better than the canonical gradient expansion did in Figure 4.11(a) in the core region, $0 < z < 1$. Figure 4.12(a) illustrates that the mGGAreV Big Z curve offers a better fit to the KS curves than the mGGA curve in the core region, $0 < z < 1$. Figure 4.12(b), which is a re-plot of Figure 4.12(a) rescaled to better view the near-nuclear region, confirms that the mGGAreV Big Z curve fits the KS curves better than the mGGA curve around the turning point and the near-nuclear region, $z \approx -1$. It is interesting to note the serpentine shaped stitching curve in the mGGA in the near-nuclear region. This serpentine shaped stitching curve will be elaborated upon throughout the remainder of the chapter. These Figures also show something surprising. It seems that the near-nuclear region of the KS curves, $z \rightarrow -\infty$, don't go to the VW limit at all! They seem to converge on a finite number that increases as Z increases!

Before the next topic in this analysis is discussed, the fact that $F_{mGGA}^p(p, q)$ does not represent a single valued function when using the z parametrization needs to be addressed. When both $F_{mGGA}^p(p, q)$ and $F_{mGGAreV}^p(z)$ do describe a single valued function is when using the parameterization $F_{model}(p = 0, q)$ vs q . It is then necessary to at least briefly analyze



(a)



(b)

Figure 4.12: **(a)** $F_{mGGArev}^p(z_{emp})$, $F_{mGGA}^p(p, q)$, $F_{ks}^p(p, q)$, and $F_{GEA2}^p(z_{emp})$ vs z_{emp} . **(b)** Re-plot of Figure 4.12(a) zoomed in on the near-nuclear region.

and contrast the mGGA with the mGGArev using this parametrization.

Figure 4.13 has the same naming conventions as those previously discussed with one addition. An $F_{mGGArev}^p(z)(p=0, q)$ stitched to a canonical gradient expansion is plotted. However $\alpha = 1$ instead of four as is the case for all other curves in this chapter. This curve is referred to as mGGArev $\alpha = 1$. The mGGArev $\alpha = 1$ model is essentially the model created by the Cancio group in section 2.5.3. Also, in Figure 4.13 the horizontal axis is not $z(p, q)$. It is $q(\mathbf{r})$ and in each enhancement factor $p(\mathbf{r})$ is set to zero.

Note that Figure 4.13 is very similar to Figure 2.3. Note also that the mGGArev Big Z curve essentially splits the serpentine stitching curve of the mGGA down the middle. This suggests that the mGGArev model may solve the mGGAs binding problem when stitching the VW limit to GEA2 Big Z, recalling that said binding problem likely stems from the mGGA approaching the VW limit too quickly. Also note the second turning point of the mGGA curve falls on the GEA2 Big Z curve, which suggests physical behavior from the GEA2 Big Z curve. Finally note the mGGArev $\alpha = 1$ curve. It seems this functional approaches the VW limit too slowly.

4.4 Analysis of the near-nuclear Regime

It was initially believed that the limit $F_{mGGArev}^p(z_{emp})$ needed to approach as $(p \rightarrow 0, q \rightarrow -\infty)$ was the VW limit. Figure 4.12(b) and Figure 4.13 seem to indicate this belief is incorrect. It seems that there is a different limiting value caused by electron density near the nucleus! What follows is a hypothesis as to why this phenomenon occurs.

4.4.1 The Link Between p shells and the Constant

While the following analysis does not specifically prove that atomic shells with an angular momentum of one, or p shells, are the mechanism by which higher Z atoms deviate from the

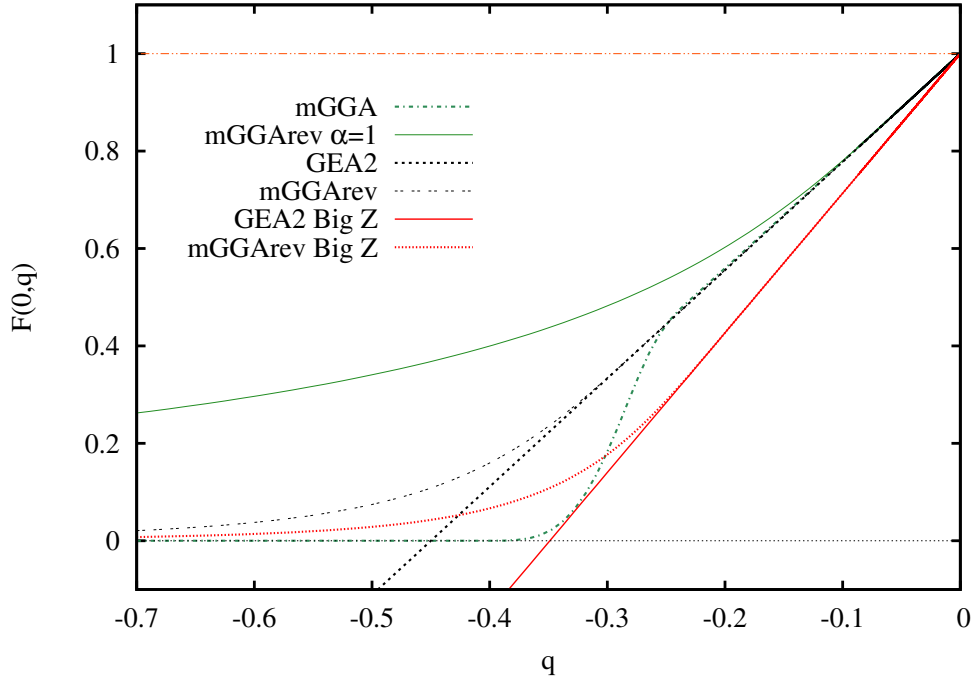


Figure 4.13: $F_{mGGA}(0, q)$, $F_{mGGA_{rev}}(0, q)$ stitched to the canonical GEA2 where $\alpha = 4$, $F_{mGGA_{rev}}(0, q)$ stitched to the canonical GEA2 where $\alpha = 1$, and $F_{mGGA_{rev}}(0, q)$ stitched to $F_{GEA2}^p(z_{emp})$ empirically fit to large Z where $\alpha = 4$ atoms vs $q(\mathbf{r})$.

VW limit in the near-nuclear regime, it is interesting. It can be shown that

$$n(\mathbf{r})[\tau_{ks}(\mathbf{r}) - \tau_{vw}(\mathbf{r})] = \frac{1}{2}[\psi_1(\mathbf{r})\nabla\psi_2(\mathbf{r}) - \psi_2(\mathbf{r})\nabla\psi_1(\mathbf{r})]^2, \quad (4.5)$$

for the case where there are two occupied orbitals. This is essentially the deviation of the KS kinetic energy from the VW kinetic energy. Note that

$$n(\mathbf{r}) = |\psi_1(\mathbf{r})|^2 + |\psi_2(\mathbf{r})|^2, \quad (4.6)$$

and

$$\tau_{ks}(\mathbf{r}) = \frac{1}{2} [|\nabla\psi_1(\mathbf{r})|^2 + |\nabla\psi_2(\mathbf{r})|^2]. \quad (4.7)$$

Also recall the definition of the VW functional is given by the square of the gradient of density, divided by one eighth the density as given by Equation 2.55. If one considers hydrogenic

wave functions of the form $|\mathbf{r}|^l e^{-Z|\mathbf{r}|}$ in the context of Equation 4.5, it can be determined that if $\psi_1(\mathbf{r})$ has $l = 0$, occupying an s shell, and $\psi_2(\mathbf{r})$ has $l > 1$ then $n(\mathbf{r})[\tau_{ks}(\mathbf{r}) - \tau_{vw}(\mathbf{r})] \rightarrow 0$ as $\mathbf{r} \rightarrow 0$. Furthermore, if both shells are s shells then $\psi_1(\mathbf{r}) \rightarrow (1 - Z|\mathbf{r}|)$ and $\psi_2(\mathbf{r}) \rightarrow (1 - Z|\mathbf{r}|)$ as $\mathbf{r} \rightarrow 0$. This means that $n(\mathbf{r})[\tau_{ks}(\mathbf{r}) - \tau_{vw}(\mathbf{r})] = (-Z + Z) = 0$. In fact, the only combination of wave functions that results in $n(\mathbf{r})[\tau_{ks}(\mathbf{r}) - \tau_{vw}(\mathbf{r})] \neq 0$ is the combination of an s and p shell. It seems that only p shells can contribute to the charge density near the nucleus. This suggests that p shells are responsible for the deviation from the F_{vw} limit in the near-nuclear regime.

4.4.2 A Toy Model

In the near-nuclear region, $z \rightarrow -\infty$, $F_{ks}^p(z)$ was fit with a $1/z$ expansion. This fit was of the form

$$f(z) = A + \frac{B}{z} + \frac{C}{z^2} + \dots \quad (4.8)$$

Equation 4.8 was fit to the KS enhancement factor of unumoctium using a density generated by FHI98PP. The fit parameters were $A = 0.021266 \pm 4.732 \times 10^{-07}$, $B = -0.0210527 \pm 1.484 \times 10^{-05}$, and $C = 0.0221753 \pm 0.0001288$. No higher orders were included in the fit. The attempt was made to modify the mGGArev model to match the constants of deviation from the VW limit of atoms as a function of Z based on this fit. However the only contribution that was non-trivial to include in the non-analytic smooth function was the constant A . The resultant toy model is given by

$$F_{mGGArevNN} = 1 + F_{vw} + z[(1 - \Theta(-z)e^{-\beta/|z|^\alpha})^{1/\alpha}], \quad (4.9)$$

where

$$\beta = 1 - \frac{\alpha A (Z - 2)^{1/3}}{(118 - 2)^{1/3}}. \quad (4.10)$$

It should be noted that β scales such that when $Z = 118$, which is the charge of ununoctium, the functional has a value of the constant deviation from the VW limit, A , rather than zero. Also when $Z = 2$ this functional is equivalent to the original mGGArev model. Although this toy model doesn't exactly count p shells, it does offer some improvement over other functionals in certain regimes, as will be seen. The argument could be made that this model lacks the proper behavior as $Z \rightarrow \infty$. This is a valid observation, however it is unlikely that an atom with a $Z > 118$ will be used in an application beyond theoretical analysis. One may also note that this toy functional breaks down for hydrogen. This is again valid. One could scale to hydrogen instead of helium in the model. This is, however, only a toy model meant to prove a concept.

At this point it is necessary to prove that this toy model simply adds a constant to the VW limit. This is the only limit that could change from mGGArev. Using a u substitution where $u = \frac{\beta}{|z|^\alpha}$ as $z \rightarrow -\infty$

$$\begin{aligned} F_{mGGArevNN} &= 1 + F_{vw} + z [1 - e^{-u}]^{1/\alpha} \approx \\ &1 + F_{vw} + z[1 - (1 - u)]^{1/\alpha} = 1 + F_{vw} + \frac{z}{|z|} \beta^{1/\alpha} = 1 + F_{vw} - \beta^{1/\alpha}. \end{aligned} \quad (4.11)$$

However, because the second term in beta is small

$$\beta^{1/\alpha} = \left[1 - \frac{\alpha A (Z - 2)^{1/3}}{(118 - 2)^{1/3}} \right]^{1/\alpha} \approx \left[1 - \frac{\alpha A (Z - 2)^{1/3}}{\alpha (118 - 2)^{1/3}} \right]. \quad (4.12)$$

Therefore

$$\lim_{z \rightarrow -\infty} F_{mGGArevNN}(z) = F_{vw} + \frac{A(Z - 2)^{1/3}}{(118 - 2)^{1/3}} \quad (4.13)$$

as long as A is small.

4.5 Kinetic Energies and Kinetic Energy Densities

What has been discussed up to now shows a potential for the mGGArev model to be an improvement over the mGGA model. However no permutation of the mGGArev model has been compared to the mGGA model in terms of total kinetic energy directly. Bond geometries, bulk properties, electron mobility, and the ability to bond at all depend on accurate total kinetic energy. If the mGGArev doesn't offer an improvement over previous models in those respects it is unlikely to have much utility.

4.5.1 Local Energy Densities

Does any permutation of the mGGArev model offer an improvement over the mGGA model for the kinetic energy density of atoms? Are there regimes where either model is superior, or is one model superior for predicting the electronic structure of every atom in the periodic table at every distance from the nucleus? What follows is the analysis of the kinetic energy density for the mGGA, mGGArev, and other pertinent models in the effort to answer said questions. These analyses were done for virtually every atom on the periodic table, however for the sake of brevity, only helium, neon, potassium, and ununoctium will be analyzed here. It should be noted that the case where $\tau_{mGGArev}$ stitches the canonical $F_{GEA2}^p(z)$ to the VW limit will not be analyzed at all in the scope of local energy densities. This is because it does not seem to offer any improvement in any regime over the mGGA model.

It is prudent at this juncture to discuss the models and naming conventions that will be seen in Figures 4.14(a)-4.17(b). It should be noted that the units of the vertical axis in each of these Figures are kinetic energy density in Hartrees with a normalizing factor for spherical symmetry. The horizontal axis is radius in atomic units.

In each of these Figures, the first sub-Figure is a plot of kinetic energy density for various models versus radius from the nucleus for a given atom. The KS kinetic energy, the VW kinetic energy and the energy of the canonical second order gradient expansion are plotted

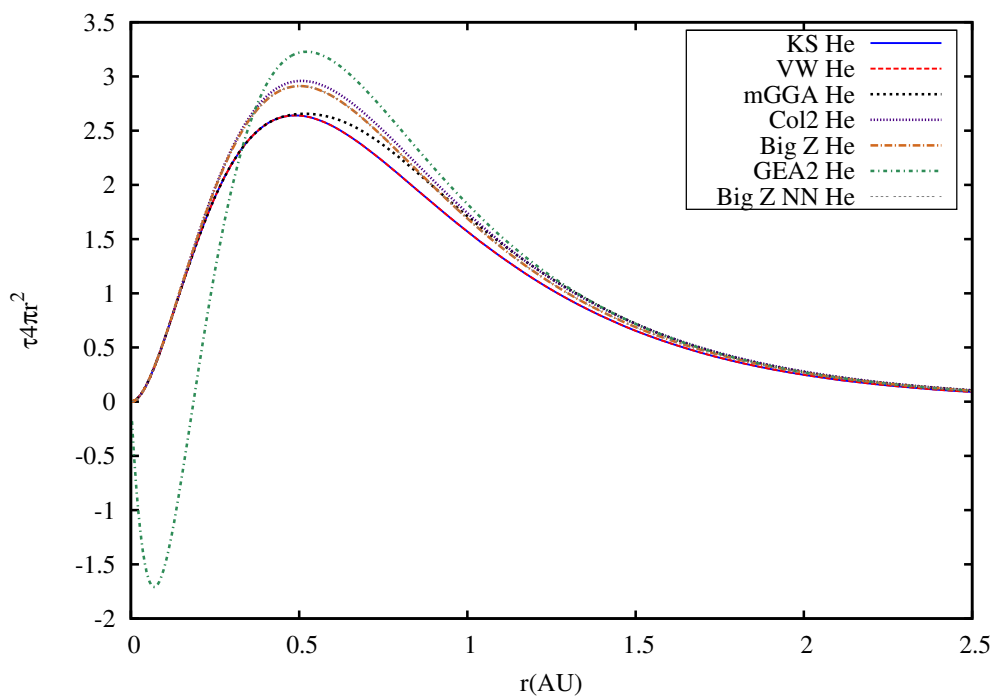
because of their limiting behaviors and other reasons already discussed. These curves will follow the naming conventions previously discussed as well. The remaining models plotted are the mGGA and various mGGArev models. In the interest of reasonably sized plot legends, the naming convention for the mGGArev models has been changed from previous plots. The mGGArev model stitching between the VW model and an empirically fit gradient expansion fit to large Z atoms will now be called Big Z instead of mGGArev Big Z. An mGGArev model stitched between the VW model and an empirically fit gradient expansion fit to the alkaline earth metals is now also plotted. This is called Col2. Finally a permutation of Big Z with the previously discussed near-nuclear correction is plotted. This is called Big Z NN.

The second sub-Figure of Figures 4.14(a)-4.17(b) plots the difference between the kinetic energy of specific models and the KS kinetic energy for a given atom. Because the KS kinetic energy is the energy that any OFDFT model is attempting to approximate, this essentially results in an error plot. The naming convention is the same as for the first sub Figures, however only mGGA and mGGArev energies were plotted.

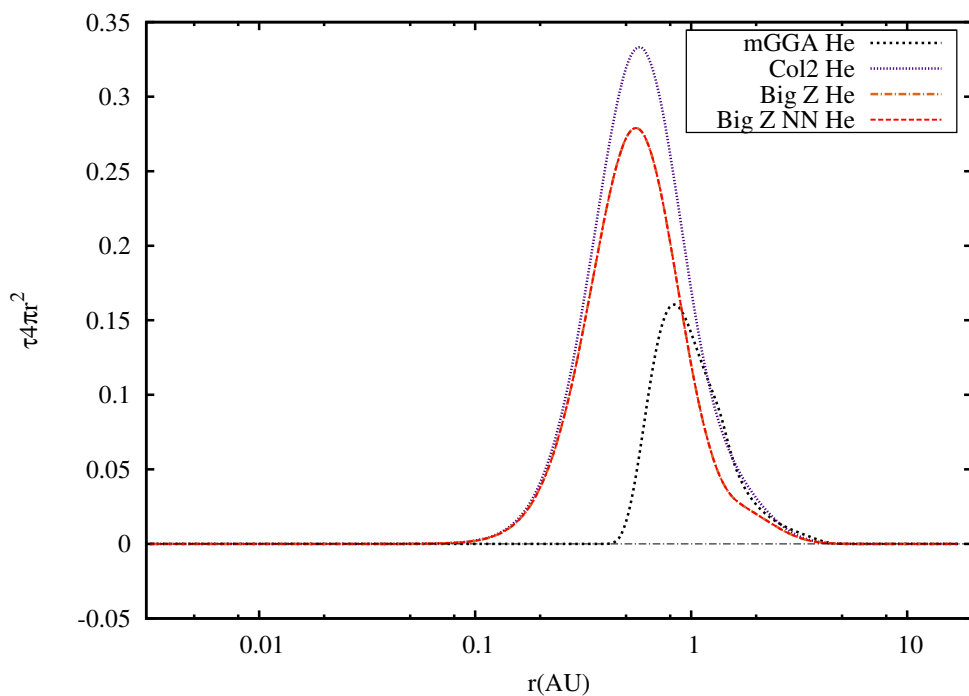
Figure 4.14(a) plots the kinetic energy density of helium for the various models. Note that the GEA2 fails the first KS constraint from section 2.4.3 because it crosses the VW kinetic energy. Recall that helium has all electrons in the lowest energy state. This means that each model should agree exactly with the VW kinetic energy. The GEA2 also fails constraints three and four from section 2.4.3 because it is not equal to the VW kinetic energy. Note that, in fact, every model fails constraints three and four except the KS model. Note that the mGGA is the closest to agreeing with the VW and KS curves.

Figure 4.14(b) plots the difference between the KS kinetic energy and the kinetic energy of the various models mentioned for helium. Note the mGGA has the best fit to the KS kinetic energy for this atom. Also note that the error in the mGGA leads the error in Col2, Big Z, and Big Z NN.

Figure 4.15(a) plots the kinetic energy density of Neon for various models. Although it seems that the mGGA has the best fit to the KS energy, it has an unnecessary sharpness as



(a)



(b)

Figure 4.14: **(a)** $4\pi r^2 \tau_{model}(r)$ of helium for several models. **(b)** $4\pi r^2 [\tau_{model}(r) - \tau_{ks}(r)]$ of helium for several models.

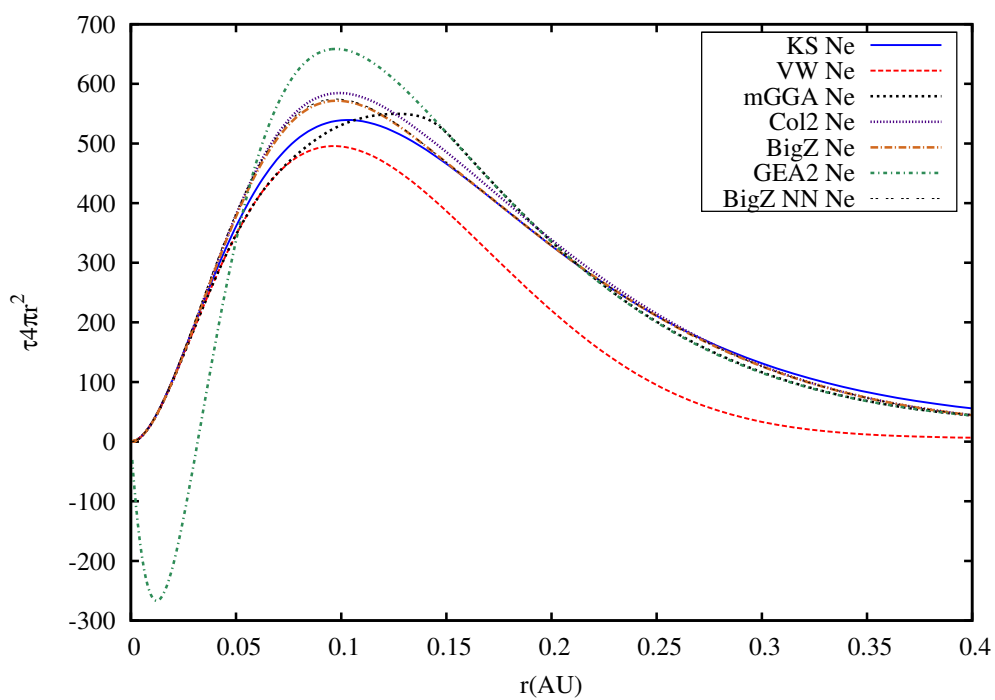
it stitches to the VW kinetic energy that seems unphysical. This is likely due to the extra turning point in the $F_{mGGA}^p(p, q)$ serpentine shaped stitching curve, as seen in Figure 4.12(b). Also note that Col2, Big Z, and Big Z NN appear to have less relative error vs their error for the helium atom.

Figure 4.15(b) plots the difference between the KS kinetic energy and the kinetic energy of the various models mentioned for neon. Note that the mGGA has an extra peak of negative error vs Col2, Big Z, and Big Z NN. This is likely due to the extra turning point in the $F_{mGGA}^p(p, q)$ serpentine shaped stitching curve. Also note that most of the error in Col2, Big Z, and Big Z NN is in the first positive peak in error, which should correspond to the 1s shell of the atom. Finally, note the first negative peak in error, or “pre-ring”, in each model and the benefit of the near-nuclear correction utilized in Big Z NN.

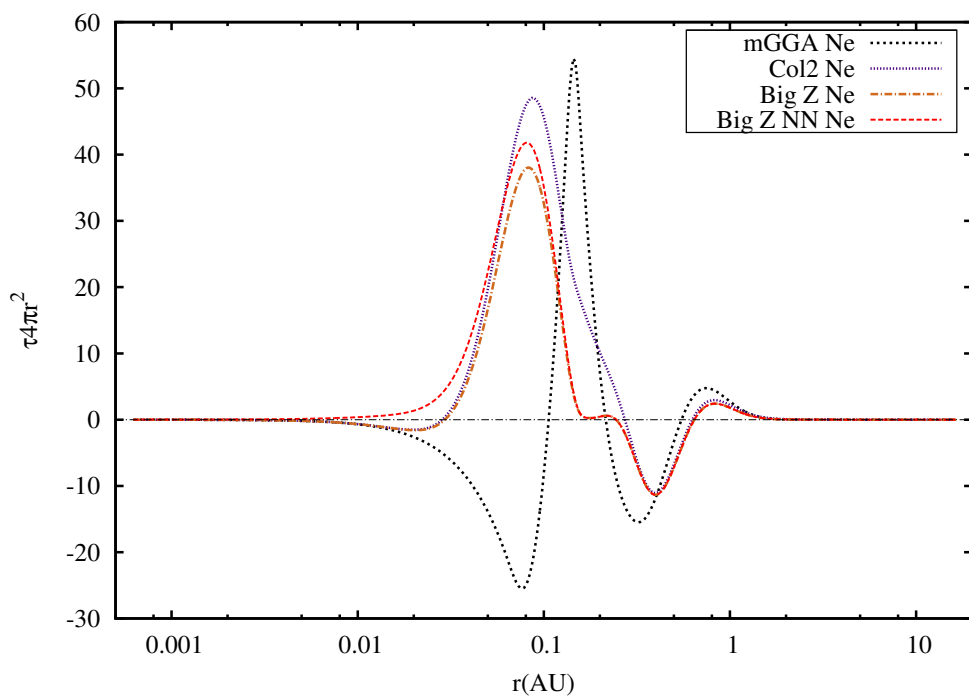
Figure 4.16(a) plots the kinetic energy density of potassium for various models. The overly sharp peak where the mGGA stitches into VW kinetic energy is more pronounced here than in neon. Also note that each Col2, Big Z, and Big Z NN now appear to fit the KS kinetic energy better locally than the mGGA.

Figure 4.16(b) plots the difference between the KS kinetic energy and the kinetic energy of the various models mentioned for potassium. Col2, Big Z, and Big Z NN definitely fit the KS kinetic energy better locally than the mGGA. Big Z and Big Z NN have very small local error. Again the “pre-ring” seems to be corrected by the near-nuclear correction. However when each model is integrated over the radius to determine total kinetic energy, it appears that the mGGA will benefit from the “prering” such that the negative error will cancel the positive error. Again the largest error in Col2, Big Z, and Big Z NN is in the first positive peak.

Figure 4.17(a) plots the kinetic energy density of ununocium. The overly sharp peak where the mGGA stitches into the VW kinetic energy is now more pronounced than in potassium. Even without the error plot it can be seen that Col2, Big Z, and Big Z NN now to fit the KS kinetic energy better locally than the mGGA.

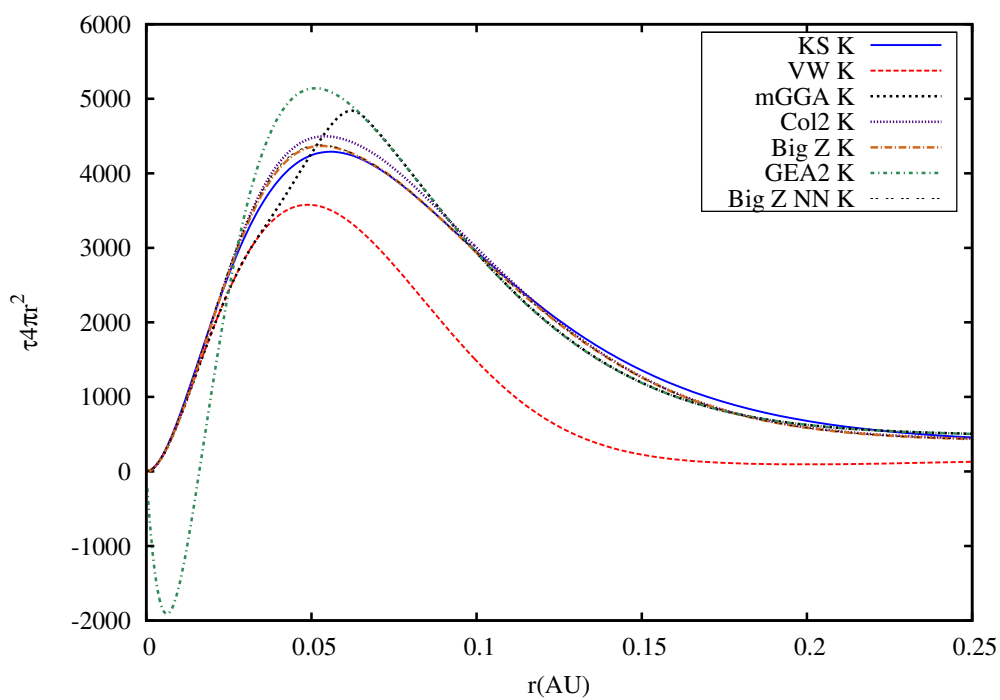


(a)

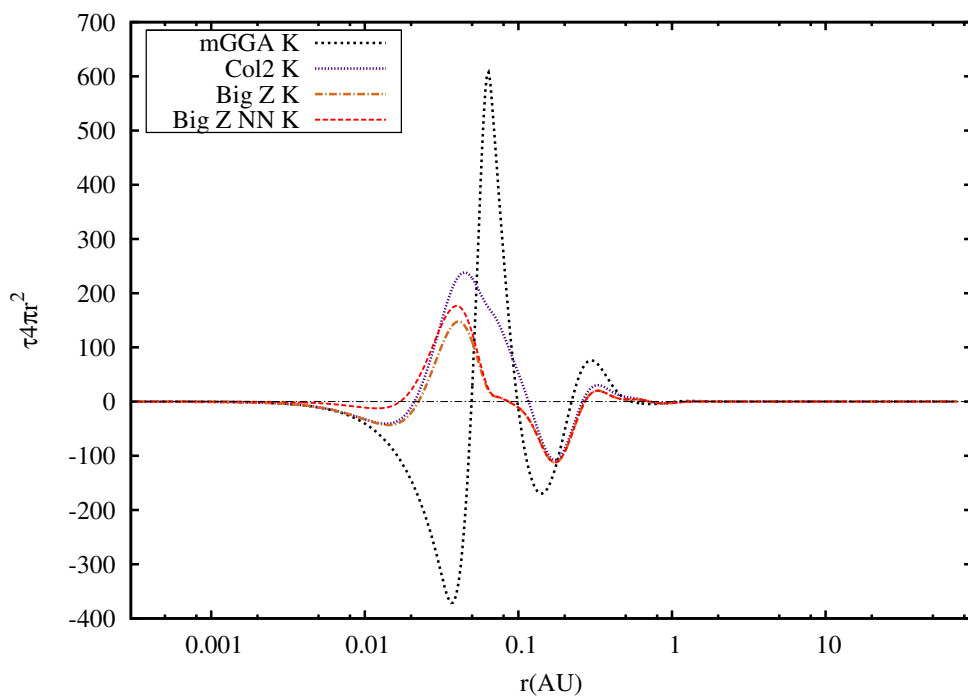


(b)

Figure 4.15: **(a)** $4\pi r^2 \tau_{model}(\mathbf{r})$ of neon for several models. **(b)** $4\pi r^2 [\tau_{model}(\mathbf{r}) - \tau_{ks}(\mathbf{r})]$ of neon for several models.



(a)



(b)

Figure 4.16: **(a)** $4\pi r^2 \tau_{model}(\mathbf{r})$ of potassium for several models. **(b)** $4\pi r^2 [\tau_{model}(\mathbf{r}) - \tau_{ks}(\mathbf{r})]$ of potassium for several models.

Figure 4.17(b) plots the difference between the KS kinetic energy and the kinetic energy of the various models mentioned for ununoctium. The first positive peak is no longer the source of largest error for Col2, Big Z, and Big Z NN. This is interesting because it suggests that Col2, Big Z, and Big Z NN are more accurate for atoms where the 1s shell doesn't contribute as much to the kinetic energy. The diminishment of this peak may, however, simply be due to the high agreement between the enhancement factors of the empirically fit gradient expansions employed and the KS enhancement factors for atoms like ununoctium. Col2, Big Z, and Big Z NN have small local error, but their error is typically locally negative which may cause an underestimation of total energy. This is the most stark correction of the pre-ring" by the near-nuclear correction

It seems that the mGGArev model offers an improvement of local energy density for atoms with $Z > 10$. It also seems that this feature of the model may be correlated to the 1s orbital. Specifically the mGGArev model seems to overestimate the kinetic energy of the 1s orbital, and that overestimation contributes less to higher Z atoms. The next step is to determine how these local behaviors equate to total energy and global behaviors.

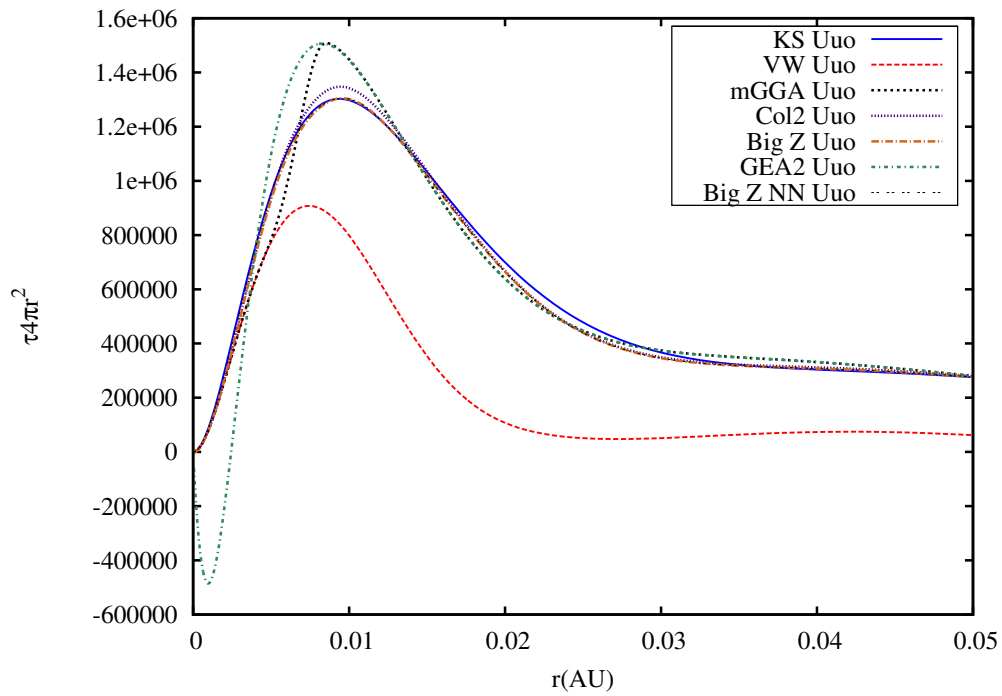
4.5.2 Total Energies

It is more important to have an accurate total kinetic energy than it is to have an accurate kinetic energy density. That having been said, with what tools does one analyze total energy in the context of atoms? It turns out that,

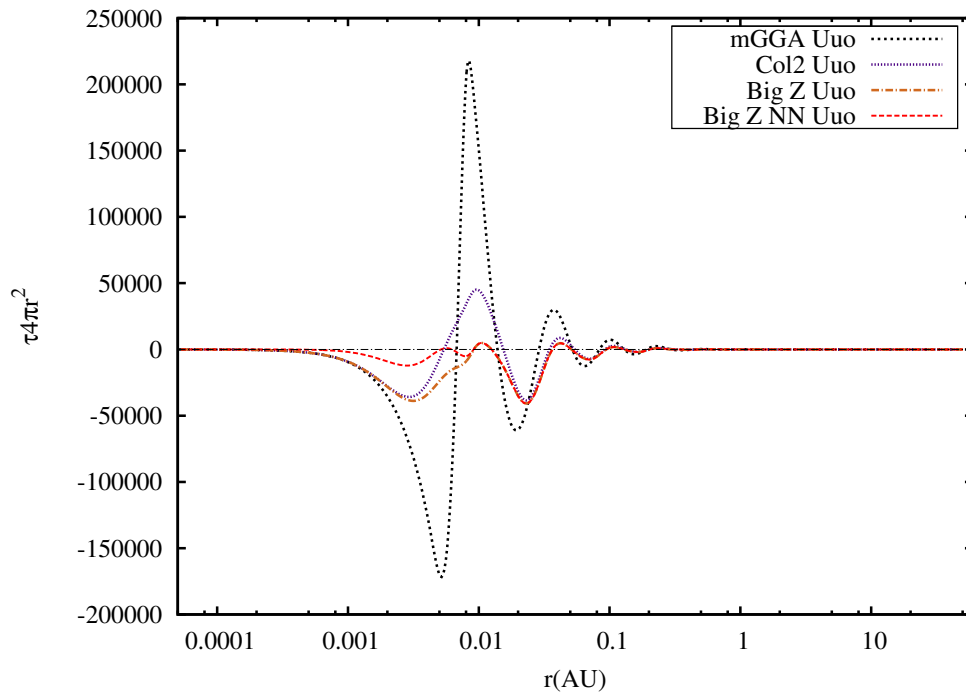
$$\lim_{Z \rightarrow \infty} T(Z) = T_H Z^{7/3} = 0.7688 Z^{7/3}, \quad (4.14)$$

where the total kinetic energy is

$$T = \int_{r=0}^{\infty} \tau_{model}(\mathbf{r}) d^3r. \quad (4.15)$$



(a)



(b)

Figure 4.17: **(a)** This plot shows $4\pi r^2 \tau_{model}(r)$ of unumoctium for several models similar to Figure 4.14(a). **(b)** This plot shows $4\pi r^2 [\tau_{model}(r) - \tau_{ks}(r)]$ of unumoctium for several models.

This is due to scaling arguments that Baers online book [8] has a wonderful treatment of. This scaling is also derived briefly in appendix D. For the task at hand it can be considered to be derived empirically. It can then be shown that the kinetic energy scales as

$$N \frac{k_f^2}{2} \propto Z(Z^{2/3})^2 = Z^{7/3}. \quad (4.16)$$

This means that $T_{tf}/Z^{7/3}$ as $Z \rightarrow \infty$ is a constant.

There is a well known representation of the gradient expansion that is as follows [37]

$$\lim_{Z \rightarrow \infty} T(Z) = c_0 Z^{7/3} + c_1 Z^{6/3} + c_2 Z^{5/3} + \dots \quad (4.17)$$

where c_0 , c_1 , and c_2 are known constants for the KS energy. This Equation comes from an asymptotic expansion which is an extension to the Baer scaling argument. Because this is an extension of the Baer scaling argument, $C_0 = 0.7688$, and the first term is the TF scaling by definition. These results should not be surprising considering the constraints on τ_{ks} in chapter two, and given that an infinite Z atom is completely homogeneous.

Each model was fit with an expansion of the form

$$y(x) = D + Ex + Fx^2 + \dots, \quad (4.18)$$

where $x = Z^{-1/3}$, $y = T/Z^{7/3}$ and D , E , and F are constants. For a model that matches the scaling behavior of the KS model well, the coefficients D , E , and F should equate to the expansion coefficients c_0 , c_1 , c_2 . This, then, presents a test of any model.

It is now necessary to discuss the conventions used in Figures 4.18(a), 4.18(b), and 4.19. Each of these Figures plot the total kinetic energy of various models as a function of nuclear charge. The data points correspond to the energy values of individual noble gases, with neon being the rightmost point and ununocium being the leftmost point. The corresponding lines are a least squares fit to the individual kinetic energies, fit with Equation 4.18 to second

order. The fit parameters are given in table 4.1. The naming conventions are the same as in previous plots.

The first model plotted in Figure 4.18(a) is the KS model for the purpose of comparison. Because the TF energy should be a constraint as $Z \rightarrow \infty$, it is plotted as well. Also to contrast the behaviors of canonical and empirically fit gradient expansions, both the GEA2 and GEA2 Big Z are plotted in Figure 4.18(a). Because the VW model is the lower bound energy for any model, it is also plotted in Figure 4.18(a). Note that all models go to the TF limit with the exception of the VW kinetic energy, which is physical due to bosonic systems necessarily having a lower kinetic energy than fermionic systems. Finally the mGGArev model stitching the VW limit to a canonical gradient expansion is plotted to illustrate the need for empirically fit gradient expansions. Note that the mGGArev overestimates virtually all atoms. Also note the relative underestimation of energy of the GEA2 Big Z curve compared to GEA2 curve. This may illustrate the behavior and benefit of the empirically fit gradient expansions in the mGGArev models.

Figure 4.18(b) is a replot of Figure 4.18(a) with only the GEA2, the mGGA, and the KS functionals plotted. It is also rescaled so that these three functionals can be compared specifically. Note the high level of agreement that the GEA2 and the mGGA scaling behavior have to the KS scaling behavior. It is interesting to note that the GEA2 consistently underestimates the KS energy. It is also interesting that the mGGA crosses the KS energy near ununocium, and goes from overestimating the KS energy to underestimating the KS energy.

Figure 4.19 is meant to compare the KS energy and various permutations of the mGGArev model to determine if any permutation of the mGGArev model is superior to the mGGA. Note all models go roughly to the TF limit, although the permutations of the mGGArev model seem to approach this limit more closely than the mGGA. It should be noted, however, that each permutation of the mGGArev model has a more quadratic nature than the mGGA and KS curves. Each mGGArev model overestimates the total energy of small Z atoms, and

underestimates the total energy of large Z atoms, although the points where each crosses the KS energy are different. Although this trend can also be seen in the mGGA it is much more pronounced in the mGGArev models, and the crossing points for the mGGArev models are at much lower values of Z . This is likely due to a lack of cancellation of error as was alluded to by Figure 4.17(b) and Figure 4.16(b), as well as the overestimation of the 1s orbital as illustrated in Figure 4.15(b) and Figure 4.14(b). Also note that Big Z NN doesn't drastically change the total energy scaling when compared to Big Z.

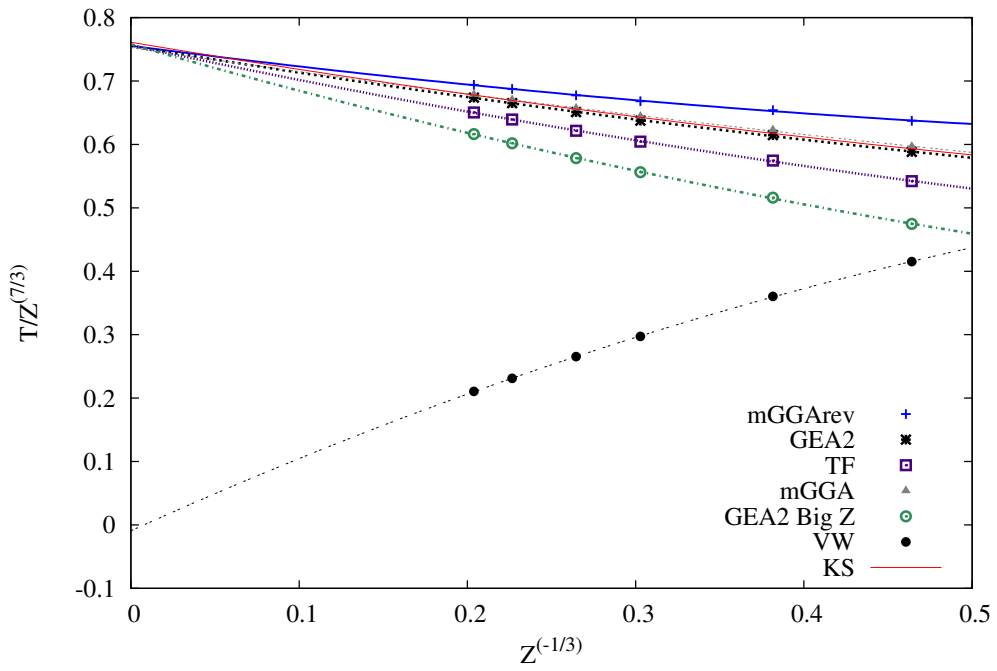
Table 4.1 further illustrates trends in the mGGA and mGGArev models. First, it is interesting that the value of the constant coefficient of the TF curve is 0.7612 not the theoretical value of 0.7688. The deviation between these values is within 2σ which is acceptable, however the fitting curve could likely be improved. Second, it is interesting to note that the constant coefficients of the mGGArev models that used empirically fit gradient expansions were closer to the TF limit than the mGGA. However the second order coefficients of the mGGArev models that used empirically fit gradient expansions were much larger than the second order coefficient of the KS curve and the mGGA.

It is interesting and important to note that the mGGA has a significantly better global behavior over the entire periodic table than Col2, Big Z, and Big Z NN. It becomes clear why when analyzing Figures 4.16(b) and 4.17(b) that the culprit is cancellation of error. Although the mGGA doesn't have as accurate a local behavior as Col2, Big Z, and Big Z NN, its over estimations in some areas cancel out its under estimations in others. It is also interesting to note that although Big Z, and Big Z NN had the best local behavior, Col2 had better global behavior. Col2, Big Z, and Big Z NN underestimate the kinetic energy density for atoms with $Z > 10$.

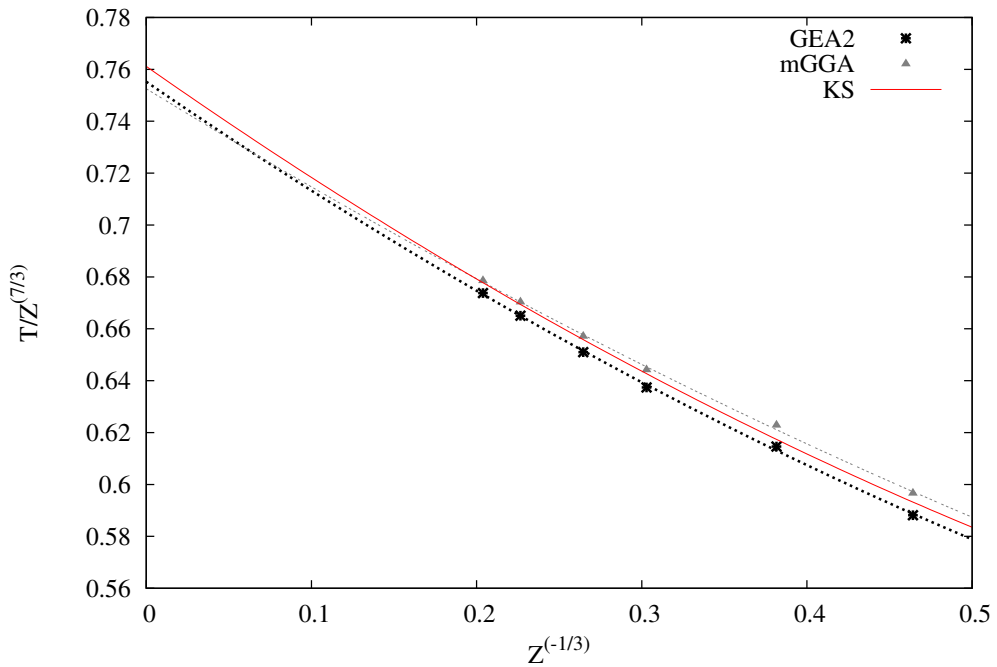
Due to the fact that Col2, Big Z, and Big Z NN overestimate the energy of atoms near $Z \leq 10$, it is likely that each overestimates the radial regimes of kinetic energy density that correspond 1s, 2s, or 2p shells specifically. Looking back at Figure 4.12(b), and at Figure 2.3 the main difference between the mGGA model and mGGArev models in the near-nuclear

region is the serpentine shaped stitching curve, and that curve falls on the portion of the hockey stick curve which should only correlate to the s shells (although this region likely doesn't capture the entire s shell region). This suggests that each permutation of mGGArev specifically overestimates the 1s shell region.

Why each permutation of the mGGArev overestimates the 1s shell region is unclear. For some clarification consider the following. Considering the mGGArev in Figure 4.18(a), the total energy was consistently overestimated for all atoms. However in the case of Big Z and Big Z NN, the total energy was overestimated for atoms with $Z \leq 10$, and underestimated for atoms with $Z > 10$ as seen in Figure 4.19. Therefore there must be a negative effect in the total energy from stitching to an empirically fit gradient expansion. This effect is clear from Figure 4.18(a). However stitching to an empirically fit gradient expansion doesn't cause one to underestimate low Z atoms. This is likely because gradient expansions are meant to describe near homogeneous systems, so one would not expect any empirically fit gradient expansion to accurately describe atoms like hydrogen or helium, due to their high inhomogeneity. So in conclusion of this chapter it seems that the mGGA model more accurately predicts kinetic energy over the mGGArev model. It is possible that if 1s shells were more accurately described by the mGGArev model, it may offer more utility. Although there may be physical arguments against the choice of stitching curve in the mGGA model, its serpentine shape gives it a desirable cancellation of error that results in an accurate estimation of the KS kinetic energy.



(a)



(b)

Figure 4.18: **(a)** This plots $T/Z^{7/3}$ vs $Z^{-1/3}$ for various kinetic energy models. **(b)** $T/Z^{7/3}$ vs $Z^{-1/3}$ for fewer, more important, kinetic energy models for visual clarity.

Model	D	E	F
T_{ks}	0.761154 ± 0.004429	-0.446117 ± 0.02833	0.181599 ± 0.04225
T_{GEA2}	0.755238 ± 0.007791	-0.43612 ± 0.04983	0.166598 ± 0.07431
T_{tf}	0.756272 ± 0.007189	-0.569638 ± 0.04598	0.235145 ± 0.06856
T_{mGGA}	0.752564 ± 0.008766	-0.390323 ± 0.05607	0.119961 ± 0.08361
$T_{mGGA_{rev}}$	0.755969 ± 0.007648	-0.335585 ± 0.04892	0.119961 ± 0.07295
$T_{mGGA_{rev}}$ Col2	0.759385 ± 0.006104	-0.506205 ± 0.03904	0.488548 ± 0.05821
$T_{mGGA_{rev}}$ Big Z	0.761324 ± 0.005477	-0.570689 ± 0.03503	0.477067 ± 0.05224
$T_{mGGA_{rev}}$ Big Z NN	0.759875 ± 0.006689	-0.544676 ± 0.04278	0.42816 ± 0.0638

Table 4.1: Table of fit parameters for various models in $T/Z^{7/3}$ vs $Z^{-1/3}$ space.

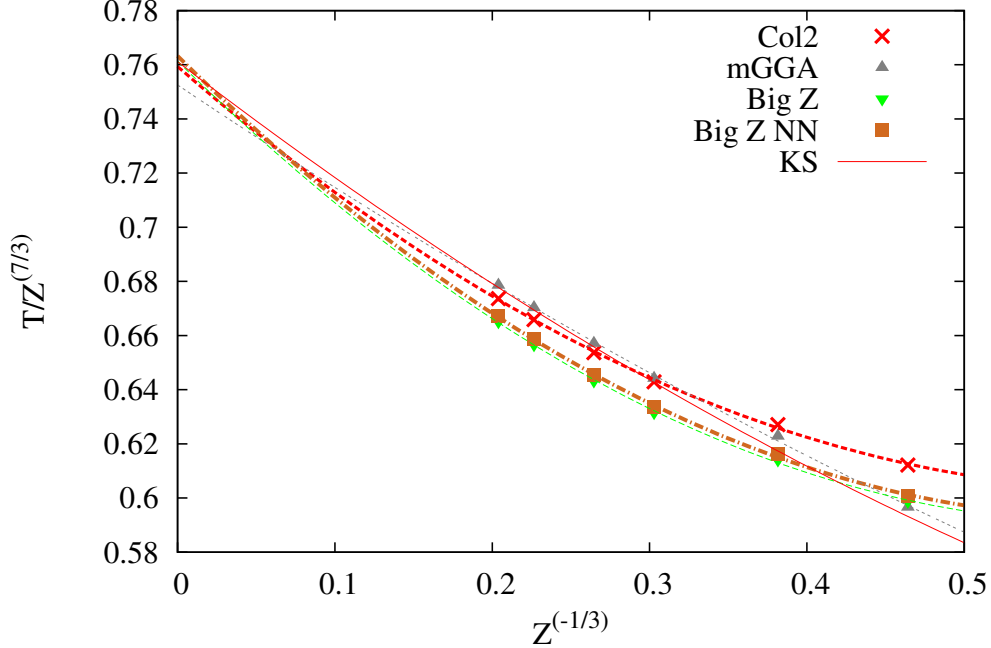


Figure 4.19: This plots $T/Z^{7/3}$ vs $Z^{-1/3}$ for various kinetic energy models.

Chapter 5

Conclusions and Future Work

5.1 Triumphs

5.1.1 Two Turning Points Vs. One

The stitching function that stitches between the GEA2 functional, which aptly approximates systems with weak inhomogeneity, and the VW limit, a limit of strong inhomogeneity, should have 1 turning point. It is clear that the KS atomic data that has been used to generate an empirical form of the kinetic energy functional, has a hockey stick shape with only one turning point, as was seen Figure 4.6(b). The mGGA model, which has a similar stitching function but with two turning points does not fit KS enhancement factor data or KS kinetic energy density data. This is undesirable because the KS model is the baseline for any OFDFT kinetic energy model, which was illustrated by 4.12(b). This feature of the mGGA creates a fair amount of error when predicting the kinetic energy density of atoms. However, this feature results in a pleasing cancellation of error in the total energies of atoms. This was seen in Figures 4.16(b) and 4.18(b).

5.1.2 Empirically Fit Gradient Expansions

The mGGArev model used several gradient expansions empirically fit to KS Pauli enhancement factors in the highly homogeneous core region for several atoms. These fits produced a smaller error than the canonical GEA2 which Figures 4.9(a) and 4.9(b) have illustrated. It is important to note that empirically fitting gradient expansions to atomic KS enhancement factors for multiple large Z atoms produces the least error in enhancement factors and in kinetic energy densities. It would be interesting and exciting to explore a theoretical mechanism that would map the canonical GEA2 to empirically fit gradient expansions in the limit of realistic large Z atoms. What that mechanism could be at this time is only speculative.

It may also be interesting to try to fit atoms as $Z \rightarrow \infty$. When gradient expansions were fit empirically to single atoms, there was a clear convergence of fit parameter values as Z increased, as is seen Figures 4.8(a) and 4.8(b). It would be desirable to determine the exact convergence value for each of these fit parameters. This sort of analysis may also give some insight into a theoretical mechanism that would explain the deviation from the canonical GEA2.

Finally the mGGArev models, when stitched to empirically fit gradient expansions, offer an improvement in local energy density over other functionals for many atoms, as was pictured in Figures 4.17(a) and 4.17(b). This model does not seem to do very well for atoms where 1s shells are the dominant shell as was pictured in Figures 4.14(a) and 4.14(b), and there is almost certainly interesting research required to explain this behavior.

5.1.3 Goldilocks Stitching Behavior

Because the mGGA stitching function has 2 turning points, its stitching function takes on a serpentine shape. This causes the mGGA model to approach the VW limit too rapidly. This is seen in Figure 4.13. Subsequently the mGGA model underestimates covalent binding energies. As discussed in section 4.3.3, the mGGArev model when stitched to an empirically fit gradient expansion splits the mGGAs serpentine shaped stitching function down the

middle. This was illustrated in Figure 4.13. The mGGArev model approaches the VW limit more slowly. This is very promising regarding the mGGArev functional’s ability to accurately predict bond energies. Because the mGGArev model doesn’t approach the VW limit as fast as the mGGA model, it is reasonable to speculate that the mGGArev model will bind better!

5.1.4 Atoms with $Z > 2$ Don’t Approach the von Weizsacker Limit

Both the mGGA model and the mGGArev model have stitching functions that asymptotically approach the VW limit as one approaches the nucleus. Recall this is due to the near-nuclear electron densities resemblance to an electron singlet. Actual KS enhancement factors do not approach the VW limit near the nucleus, but instead approach a constant that seems to be a function of the number of occupied p orbitals of the atom. A crude correction was added to the mGGArev model to describe this behavior. This correction relied on a $1/z(p, q)$ expansion, given by Equation 4.8, to find the constant by which the VW limit was corrected. Although this correction does not seem to make a drastic difference in the total energy scaling of the mGGArev model, it was clear from Figure 4.17(b) that the first negative error peak, or ”pre-ring”, is reduced by the near-nuclear correction for most atoms. Although a more accurate near-nuclear correction could be employed by using the higher orders of the expansion fit in the near-nuclear region, as a proof of concept it was a success. It should be noted that this model doesn’t work for hydrogen.

5.2 Failings

5.2.1 Underestimation of the Total Energy for Large Z Atoms

The mGGA model calculates the total energy of virtually every atom on the periodic table better than the mGGArev. For atoms with $Z > 10$, the mGGArev model has a better local behavior than the mGGA model. Unfortunately its error is typically negative whereas the

mGGA model has a very favorable cancellation of error for most atoms, as was illustrated by Figure 4.18(a). This cancellation of error certainly stems from the serpentine shaped stitching curve that the mGGA employs. It is likely that a portion of the mGGArev models failing in this regard stems from a misfit in the near-nuclear region of atoms. Improving the behavior of the mGGArev model in this regime would likely be beneficial.

5.2.2 Overestimation of the Total Energy for Small Z Atoms

For low Z atoms, the mGGArev model drastically overestimates total energy, and the mGGA model predicts local behavior better. This is because the mGGArev model overestimates the 1s orbital energy, which was clear from Figures 4.14(a) and 4.14(b). The most likely culprit is the misfit of the constant shift from the VW limit in the near-nuclear region. This is illustrated in Figure 4.12(b). The near-nuclear correction was meant to combat this problem to a certain extent, but the model was a toy and nothing more. The use of $1/z$ expansions may give some insight into how to potentially fit this region better in the future.

5.3 Future Work

The most pressing work is to better fit the KS kinetic energy in the near-nuclear region. It is clear that a better fit in this region could potentially resolve a number of issues with the mGGArev model. It is unclear if increased density near the core due to p orbitals is the cause of the near-nuclear densities departure from a 1s shell behavior, but it seems likely. Also, different atoms don't leave the GEA2 curve at the same rate, which was illustrated by Figure 4.12(b). It is also important to model a near-nuclear correction that isn't a function of Z, which is not ideal.

Second, it is important that the binding hypothesis is tested. It seems reasonable to speculate that the permutation of the mGGArev model that uses an empirically fit gradient expansion fit to large Z atoms approaches the VW limit more physically than mGGA model.

This behavior should improve binding. However, it cannot be known for sure if the mGGArev model will improve poor binding without using it to model chemical binding.

Third, there is a limit of the KS model that was intentionally neglected during the discussion surrounding 2.4.3. Because an electron gas where all particles are found in the ground state is the lower bound of kinetic energy for a unique potential, one can construct a correction to $T_{vw}[n]$ such that $T_{ks}[n] = T_{vw}[n] + T_{pauli}[n]$ [3]. Another way of saying this is that $T_{ks}[n] - T_{vw}[n]$ gives the energy due to the fermionic behavior of electrons. This being the case, there is a constraint that follows. Because the energy of any fermionic system must be greater than the energy of any Bose system, $T_{pauli}[n] \geq 0$. Subsequently, $\frac{\delta(T_{ks}-T_{vw})}{\delta n(\mathbf{r})} \geq 0$. Because a functional derivative of T is necessary to self consistently solve for density, any model that hopes to approximate T_{ks} must meet this constraint. The mGGArev model must then be tested under this constraint.

Finally, for the analysis of the mGGArev model, externally produced densities were used. Those densities were produced by a program, FHI98PP. Using a trusted density to test a model is an effective way to analyze its behavior, but the utility of the model is to produce densities, not to use them. In the future the mGGArev kinetic energy functional needs to be employed in a self consistent code, to produce densities. This is meant ensure that the mGGArev model will converge in self consistent calculations, and to ensure that it can produce reliable densities.

Appendix A

List of Acronyms

DFT Density Functional Theory

GEA Gradient Expansion Approximation

KS Kohn-Sham

HF Hartree-Fock

mGGA metta-Generalized Gradient Approximation

OFDFT Orbital Free Density Functional Theory

VW von Weizsacker

Appendix B

Lagrangian Interpolation Polynomials and Derivatives

Given a data set of $n + 1$ points, one can construct an interpolating n order polynomial

$$P(x) = \sum_{i=0}^n \omega_i(x) y_i, \quad (\text{B.1})$$

where y_i is $f(x_i)$ and $\pi_i(x)$ is constructed from the fundamental interpolating polynomials which are as follows [33],

$$\pi(x) = \prod_{l=0}^n (x - x_l), \quad (\text{B.2})$$

$$\pi_i(x) = \prod_{l=0, l \neq i}^n (x - x_l), \quad (\text{B.3})$$

$$\pi_{ij} = \prod_{l=1, l \neq i, j}^n (x - x_l), \quad (\text{B.4})$$

such that

$$\omega_i(x) = \frac{\pi_i(x)}{\pi_i(x_i)}. \quad (\text{B.5})$$

One can also find derivatives of these polynomials as follows

$$\frac{d}{dx}P(x) = \sum_{i=1}^n y_i \frac{d}{dx}\omega_i(x) = \sum_{i=1}^n y_i \frac{\frac{d}{dx}\pi_i(x)}{\pi_i(x_i)} = \sum_{i=1}^n y_i \frac{\pi_i'(x)}{\pi_i(x_i)}, \quad (\text{B.6})$$

where by applying a product rule the resultant Equation is

$$\pi_i'(x) = \sum_{j=0, j \neq i}^n \pi_{ij}(x). \quad (\text{B.7})$$

This can be generalized to N derivatives, although it looks a bit messy because of product rules inside product rules, and it is using this method that all derivatives are calculated in the code used in this thesis.

It should be noted that extensive testing was done by Neal Coleman in an effort to relate numerical error to the order of the interpolating polynomial, vs a geometric factor $1 + \gamma$ (refer to chapter 3) [38]. For small gamma he showed that there is little to no gain in increasing the order of the polynomial beyond 13 (meaning 6 grid points are sampled to each side of the point interpolated about), for geometric factors below 1.04. Recalling then that $\gamma = 0.0247$ in FHI98PP a polynomial of order 13 was chosen.

Appendix C

Hartree Fock

The Hartree-Fock method is a single body method, similar to the Kohn-Sham model. The single body wave function total energy is given by

$$\begin{aligned} E_{HF} = & -\frac{1}{2} \sum_{j=1}^N \int \phi_j^*(\mathbf{r}) \nabla^2 \phi_j(\mathbf{r}) d\mathbf{r} + \frac{1}{2} \sum_{j=1, i=1} \int \frac{\phi_j^*(\mathbf{r}_1) \phi_i^*(\mathbf{r}_2) \phi_j(\mathbf{r}_1) \phi_i(\mathbf{r}_2)}{|\mathbf{r}_1 - \mathbf{r}_2|} d\mathbf{r}_1 d\mathbf{r}_2 \\ & -\frac{1}{2} \sum_{j=1, i=1} \int \frac{\phi_j^*(\mathbf{r}_1) \phi_i^*(\mathbf{r}_2) \phi_i(\mathbf{r}_1) \phi_j(\mathbf{r}_2)}{|\mathbf{r}_1 - \mathbf{r}_2|} d\mathbf{r}_1 d\mathbf{r}_2 + \sum_{j=1} \int \phi_j^*(\mathbf{r}) \phi_j(\mathbf{r}) \nu(\mathbf{r}) d\mathbf{r}, \end{aligned} \quad (\text{C.1})$$

where

$$\begin{aligned} E_{int} = & \frac{1}{2} \sum_{j=1, i=1} \int \frac{\phi_j^*(\mathbf{r}_1) \phi_i^*(\mathbf{r}_2) \phi_j(\mathbf{r}_1) \phi_i(\mathbf{r}_2)}{|\mathbf{r}_1 - \mathbf{r}_2|} d\mathbf{r}_1 d\mathbf{r}_2 \\ & -\frac{1}{2} \sum_{j=1, i=1} \int \frac{\phi_j^*(\mathbf{r}_1) \phi_i^*(\mathbf{r}_2) \phi_i(\mathbf{r}_1) \phi_j(\mathbf{r}_2)}{|\mathbf{r}_1 - \mathbf{r}_2|} d\mathbf{r}_1 d\mathbf{r}_2 \end{aligned} \quad (\text{C.2})$$

is the Hartree-Fock internal energy. This functional is quite interesting. It is related to an electron with a screening hole, but because of the non local nature of this functional, electron exchange is built in. In fact this functional perfectly describes exchange. This is not too shocking if one knows how exchange is defined using the density matrix, and the pair density matrix. The Kohn-Sham method, however, gives more accuracy for less computational cost in most systems, so the Hartree-Fock method is less used.

Appendix D

Thomas Fermi Scaling

Let

$$\phi_{\alpha,\lambda}(\mathbf{r}) = \alpha\phi(\lambda\mathbf{r}) = \int \frac{n_{+\alpha,\lambda}(\mathbf{r}') - n_{-\alpha,\lambda}(\mathbf{r}')}{|\mathbf{r} - \mathbf{r}'|} d^3r' + \mu \quad (\text{D.1})$$

be a TF potential. From Equation E.7 it can be show that

$$\nabla^2\phi_{\alpha,\lambda}(\mathbf{r}) = [A\phi_{\alpha,\lambda}(\mathbf{r})]^{3/2} - n_{+\alpha,\lambda}(\mathbf{r}) = [A\alpha\phi(\lambda\mathbf{r})]^{3/2} - n_{+\alpha,\lambda}(\mathbf{r}), \quad (\text{D.2})$$

but the laplacian can also be taken in the context of

$$\nabla^2\phi_{\alpha,\lambda}(\mathbf{r}) = \nabla^2[\alpha\phi(\lambda\mathbf{r})] = \alpha\lambda^2[A\phi(\lambda\mathbf{r})]^{3/2} - \alpha\lambda^2n_+(\lambda\mathbf{r}). \quad (\text{D.3})$$

Combining Equations D.2 and D.3 results in

$$n_{+\alpha,\lambda}(\mathbf{r}) = [A\phi(\lambda\mathbf{r})]^{3/2}\alpha(\alpha^{1/2} - \lambda^2) + \alpha\lambda^2n_+(\lambda\mathbf{r}). \quad (\text{D.4})$$

If one sets $\alpha = \lambda^4$, this results in

$$n_\lambda(\mathbf{r}) = \lambda^6n_+(\lambda\mathbf{r}) \quad (\text{D.5})$$

and given Equation 2.28

$$T[n_\lambda] = \lambda^7 T[n]. \quad (\text{D.6})$$

If one lets $T[n]$ be the kinetic energy for hydrogen, and $T[n_\lambda]$ be the kinetic energy for some atom with charge Z , and finally let $\lambda = Z^{-1/3}$ for radial scale invariance then

$$T_Z = T_H Z^{7/3} = 0.7688 Z^{7/3}. \quad (\text{D.7})$$

Appendix E

The Thomas-Fermi Potential

It is expedient when discussing the Thomas-Fermi potential to consider only how the kinetic energy and Hartree functionals interact with V_{ext} to determine their physicality, so that exchange and correlation corrections don't affect the result. One can then re-write Equation 2.41 as

$$\epsilon_f + \int \frac{n(\mathbf{r}') - n_+(\mathbf{r}')}{|\mathbf{r} - \mathbf{r}'|} d^3r' = \mu. \quad (\text{E.1})$$

Because the first term in Equation E.1 is ϵ_f , one can define a potential [8]

$$\phi(\mathbf{r}) = \int \frac{n_+(\mathbf{r}') - n(\mathbf{r}')}{|\mathbf{r} - \mathbf{r}'|} d^3r' + \mu. \quad (\text{E.2})$$

This is called the Thomas-Fermi potential.

It may seem that the Thomas-Fermi potential is simply some expression that has the proper units of a potential with no clear physical meaning. This is not the case. Consider the following. Imagine what the change in energy of an electron gas would be if a positively charged particle were added to the system [8],

$$\delta E_{tot}[n, n_+] = \int \left\{ \frac{\delta E_{tf}[n, n_+]}{\delta n(\mathbf{r})} \delta n(\mathbf{r}) + \frac{\delta E_{tf}[n, n_+]}{\delta n_+(\mathbf{r})} \delta n_+(\mathbf{r}) \right\} d^3r + \int \frac{n_+(\mathbf{r}) \delta n_+(\mathbf{r}')}{|\mathbf{r} - \mathbf{r}'|} d^3r d^3r'. \quad (\text{E.3})$$

Knowing that $\delta n(\mathbf{r}) = \delta n_+(\mathbf{r})$ it can be shown with some effort that Equation E.3 can be written as

$$\delta E_{tot} = \int \left[\mu + \int \frac{n_+(\mathbf{r}') - n(\mathbf{r}')}{|\mathbf{r} - \mathbf{r}'|} d^3 r' \right] \delta n_+(\mathbf{r}) d^3 r \rightarrow \int [\phi(\mathbf{r})] \delta n_+(\mathbf{r}) d^3 r. \quad (\text{E.4})$$

This means that the Thomas-Fermi potential is the potential of adding a positively charged particle to an electron gas. This potential then is tantamount to the conditions that determine molecular binding.

E.0.1 The Binding Problem

Because the TF potential is physical it must satisfy Poisson's Equation. Taking the laplacian of Equation E.2 results in

$$\nabla^2 \phi(\mathbf{r}) = n(\mathbf{r}) - n_+(\mathbf{r}), \quad (\text{E.5})$$

bearing in mind that $\nabla^2 \frac{1}{|\mathbf{r}|} = \delta(\mathbf{r})$. Recall that $\frac{5}{3} C_1 n(\mathbf{r})^{2/3} = \epsilon_f$. With this in mind, if one then plugs Equation E.2 into Equation E.1 it can be shown that

$$n(\mathbf{r}) = A \phi(\mathbf{r})^{3/2}, \quad (\text{E.6})$$

where A is some positive constant. This means that

$$\nabla^2 \phi(\mathbf{r}) = A \phi(\mathbf{r})^{3/2} - n_+(\mathbf{r}). \quad (\text{E.7})$$

Consider Equation E.7 briefly. In order for binding to occur, a global minimum is required. However, because $\phi(\mathbf{r})^{3/2}$ is a number density it must be positive, therefore $\phi(\mathbf{r}) > 0$ [10]. This means the potential is always greater than zero. If the potential must be positive, there can be no molecular binding. This is because there is no globally minimum potential well, due to the fact that for any finite volume of charge $\lim_{r \rightarrow \infty} \phi(\mathbf{r}) = 0$.

Bibliography

- [1] Antonio C Cancio, Dane Stewart, and Aeryk Kuna. *Visualizing orbital-free descriptions of the kinetic energy density for molecules and the covalent bond.* pending (pending).
- [2] P. Hohenberg and W. Kohn. *Inhomogeneous electron gas.* *Physical Review B* **139**, 864 (1964).
- [3] Valentin V Karasiev, Debajit Chakraborty, and SB Trickey. *Progress on new approaches to old ideas: Orbital-free density functionals.* In “Many-Electron Approaches in Physics, Chemistry and Mathematics,” pages 113–134. Springer (2014).
- [4] Chen Huang and Emily A Carter. *Nonlocal orbital-free kinetic energy density functional for semiconductors.* *Physical Review B* **81(4)**, 045206 (2010).
- [5] Junchao Xia, Chen Huang, Ilgyou Shin, and Emily A Carter. *Can orbital-free density functional theory simulate molecules?* *The Journal of chemical physics* **136(8)**, 084102 (2012).
- [6] Richard Martin. *Electronic Structure: Basic Theory and Practical Methods.* Cambridge University Press (2004).
- [7] Fabien Tran and Tomasz A Wesolowski. *Link between the kinetic-and exchange-energy functionals in the generalized gradient approximation.* *International journal of quantum chemistry* **89(5)**, 441 (2002).
- [8] Roi Baer. *Electron density functional theory* (2009).
- [9] Aurora Pribram-Jones, David A Gross, and Kieron Burke. *Dft: A theory full of holes?* *arXiv preprint arXiv:1408.4826* (2014).
- [10] Edward Teller. *On the stability of molecules in the thomas-fermi theory.* *Reviews of Modern Physics* **34(4)**, 627 (1962).
- [11] W. Kohn and L. J. Sham. *Self-consistent equations including exchange and correlation effects.* *Physical Review* **140**, A1133 (1965).
- [12] John P Perdew and Lucian A Constantin. *Laplacian-level density functionals for the kinetic energy density and exchange-correlation energy.* *Physical Review B* **75(15)**, 155109 (2007).

- [13] Roi Baer, Daniel Neuhauser, and Eran Rabani. *Self-averaging stochastic kohn-sham density-functional theory*. *Physical review letters* **111(10)**, 106402 (2013).
- [14] Luca Salasnich. *Kirzhnits gradient expansion for a d-dimensional fermi gas*. *Journal of Physics A: Mathematical and Theoretical* **40(33)**, 9987 (2007).
- [15] A Putaja, E Räsänen, R van Leeuwen, JG Vilhena, and MAL Marques. *Kirzhnits gradient expansion in two dimensions*. *Physical Review B* **85(16)**, 165101 (2012).
- [16] Frank Neese. *A critical evaluation of dft, including time-dependent dft, applied to bioinorganic chemistry*. *JBIC Journal of Biological Inorganic Chemistry* **11(6)**, 702 (2006).
- [17] Daniele Sanna, Vincent L Pecoraro, Giovanni Micera, and Eugenio Garribba. *Application of dft methods to the study of the coordination environment of the vo²⁺ ion in v proteins*. *JBIC Journal of Biological Inorganic Chemistry* **17(5)**, 773 (2012).
- [18] Damian G Allis, Darya A Prokhorova, and Timothy M Korter. *Solid-state modeling of the terahertz spectrum of the high explosive hmx*. *The Journal of Physical Chemistry A* **110(5)**, 1951 (2006).
- [19] YD Park, AT Hanbicki, SC Erwin, CS Hellberg, JM Sullivan, JE Mattson, TF Ambrose, A Wilson, G Spanos, and BT Jonker. *A group-iv ferromagnetic semiconductor: Mn_xGe_{1-x}*. *Science* **295(5555)**, 651 (2002).
- [20] Robert O Jones and Olle Gunnarsson. *The density functional formalism, its applications and prospects*. *Reviews of Modern Physics* **61(3)**, 689 (1989).
- [21] Leeor Kronik, Tamar Stein, Sivan Refaely-Abramson, and Roi Baer. *Excitation gaps of finite-sized systems from optimally tuned range-separated hybrid functionals*. *Journal of Chemical Theory and Computation* **8(5)**, 1515 (2012).
- [22] Ilgyou Shin and Emily A Carter. *Possible origin of the discrepancy in peierls stresses of fcc metals: First-principles simulations of dislocation mobility in aluminum*. *Physical Review B* **88(6)**, 064106 (2013).
- [23] Linda Hung and Emily A Carter. *Orbital-free dft simulations of elastic response and tensile yielding of ultrathin [111] al nanowires*. *The Journal of Physical Chemistry C* **115(14)**, 6269 (2011).
- [24] Qing Peng, Xu Zhang, Linda Hung, Emily A Carter, and Gang Lu. *Quantum simulation of materials at micron scales and beyond*. *Physical Review B* **78(5)**, 054118 (2008).
- [25] Valentin V Karasiev, Travis Sjostrom, and SB Trickey. *Generalized-gradient-approximation noninteracting free-energy functionals for orbital-free density functional calculations*. *Physical Review B* **86(11)**, 115101 (2012).
- [26] Baojing Zhou, Vincent L Ligneres, and Emily A Carter. *Improving the orbital-free density functional theory description of covalent materials*. *The Journal of chemical physics* **122(4)**, 044103 (2005).

- [27] M. Born and R. Oppenheimer. *Ann. Phys.* **389**, 457 (1927).
- [28] Charles Kittel. *Introduction to Solid State Physics*. John Wiley & Sons (2005).
- [29] M Ya Amusia, AZ Msezane, and VR Shaginyan. *Density functional theory versus the hartree-fock method: Comparative assessment*. *Physica Scripta* **68(6)**, C133 (2003).
- [30] David Jeffery Griffiths. *Introduction to quantum mechanics*. Pearson Education India (2005).
- [31] Richard F. W. Bader. *A quantum theory of molecular structure and its applications*. *Chemical Reviews* **91(5)**, 893 (1991). URL <http://dx.doi.org/10.1021/cr00005a013>.
- [32] Martin Fuchs and Matthias Scheffler. *Ab initio pseudopotentials for electronic structure calculations of poly-atomic systems using density-functional theory*. *Computer Physics Communications* **119(1)**, 67 (1999).
- [33] Neal Coleman. *Report iii: Report on polynomial interpolation* (2009). Internal Report.
- [34] Donghyung Lee, Lucian A Constantin, John P Perdew, and Kieron Burke. *Condition on the kohn-sham kinetic energy and modern parametrization of the thomas-fermi density*. *The Journal of chemical physics* **130(3)**, 034107 (2009).
- [35] Antonio C Cancio and Chris E Wagner. *Laplacian-based generalized gradient approximations for the exchange energy*. *arXiv preprint arXiv:1308.3744* (2013).
- [36] Thomas Williams, Colin Kelley, and many others. *Gnuplot 4.4: an interactive plotting program*. <http://gnuplot.sourceforge.net/> (March 2010).
- [37] Donghyung Lee, Lucian A Constantin, John P Perdew, and Kieron Burke. *Condition on the kohn-sham kinetic energy and modern parametrization of the thomas-fermi density*. *The Journal of chemical physics* **130(3)**, 034107 (2009).
- [38] Neal Coleman. *Numerical method for calculating xc potentials* (2009). Internal Report.